

Online and Offline Dielectric Condition Diagnosis of High Voltage Ceramic Insulators in wet-type Electrostatic Tar Precipitator Units

vorgelegt von
Dipl.-Ing. (FH)
Philipp Schröder

an der Fakultät IV - Elektrotechnik und Informatik
der Technischen Universität Berlin
zur Erlangung des akademischen Grades

Doktor der Ingenieurwissenschaften
- Dr.-Ing. -

genehmigte Dissertation

Promotionsausschuss:

Vorsitzender: Prof. Dr.-Ing. Kai Strunz

Gutachter: Prof. Dr.-Ing. Ronald Plath

Gutachter: Prof. Dr.-Ing. Ulrich Riebel

Gutachter: Dr.-Ing. Thomas Schoenemann

Tag der wissenschaftlichen Aussprache: 23. Juli 2021

Berlin 2021

Acknowledgment

The present thesis was carried out as research associate at the Institute for Electrical Power Engineering, chair of High Voltage and High Current Technologies, at the University of Rostock and at the Institute of Energy Engineering at the Berlin University of Technology. I would like to thank all persons who have through their cooperation and support contributed to the achievement of this thesis.

First of all, I would particularly like to thank my supervisor Professor Dr.-Ing. Thomas Schoenemann for his great support and encouragement of my research work, his scientific guidance and continued support.

I am most grateful to Professor Dr.-Ing. Ronald Plath for giving me the opportunity of defending my PhD Thesis at the Berlin University of Technology. I also would like to thank Prof. Plath for the valuable discussions, his scientific guidance and his support to finalize my thesis.

My thanks go to Professor Dr.-Ing. Ulrich Riebel from the Brandenburg University of Technology for their willingness and commitment reviewing my thesis.

I also would like to express my special thanks to my colleagues Dr.-Ing. York Neubauer and Dr.-Ing. Saravanakumar Arumugam for their continued help and support of my research work, valuable discussions and their technical advice. I am also thankful to Dr.-Ing. Marcus Schuchardt for the valuable discussions and his support with measurement equipment.

In addition to this, I would like to acknowledge the LDS 6 UHF software support of the HHD GmbH.

Furthermore, I would like to express my thanks to my colleagues Yvonne Haba and Holger Strate from the Institute of Electrical Power Engineering of the University of Rostock and to my colleagues Dr. rer. nat. Eva-Maria Brüning, Sandra Walther, Omid-Henrik Elhami, Dr. Thomas Mouton and Joseph Baarmann from the junior research group TCKON at Berlin University of Technology for their help, collegue-ship and teamwork.

My final acknowledgment is to my parents and my brother for their continuous support.

List of Publications

The present thesis is based on the following publications:

- Y. Neubauer, P. Schröder, I. Litvinov, A. Kölling, H. Liu, W. Zhang, N. Sachno, U. Hellwig, H. Oldenburg, A. Seilkopf. Gas Treatment of Fuel Gases from Biomass Gasification with Structured Tube Gas Cooling, Quench, Electrostatic Precipitator and Mop Fan Filter - Experimental Results of an ERANET Bioenergy Project. In 19th European Biomass Conference and Exhibition, 2011, Berlin, pages 1420-1425, DOI: 10.5071/19thEUBCE2011-VP2.3.18. [15]
- Y. Neubauer, A. Kölling, P. Schröder, F. Behrendt, U. Hellwig, N. Sachno, H. Liu, W. Zhang, I. Ul Hai, S. B. Riffat, H. Oldenburg. Gas Treatment of Fuel Gases from Biomass Gasification with structured tube Gas Cooling, Quench, Electrostatic Precipitator and Mop-Fan Filter (EMF) - Effectiveness and Viability of Components developed in ERA-NET Bioenergy Project. In 20th EU Biomass Conference and Exhibition 2012, Milan, pages 844-849, DOI: 0.5071/20thEUBCE2012-2CO.4.5. [16]
- P. Schröder, S. Arumugam, Y. Neubauer, M. Schuchardt, F. Behrendt, and T. Schoenemann. Investigations on ageing phenomena on a tar contaminated porcelain insulator. In 19th International Conference on Gas Discharge and Their Applications, 2-7 September 2012, Beijing, China, pages 778781, 2012. [66]
- P. Schröder, S. Arumugam, Y. Neubauer, and T. Schoenemann. Diagnosis of operating conditions of high voltage insulators in electrostatic precipitators. In ETG-Fachbericht 134 - Diagnostik elektrischer Betriebsmittel 2012, 15-16 November 2012, Fulda, ISBN 978-3-8007-3465-8. [63]
- W. Zhang, H. Liu, I. Ul Hai, Y. Neubauer, P. Schröder, H. Oldenburg, A. Seilkopf, A. Kölling. Gas cleaning strategies for biomass gasification product gas. International Journal of Low-Carbon Technologies, 2012, 7 (2), DOI: 10.1093/ijlct/ctr046. [8]
- P. Schröder, S. Arumugam, Y. Neubauer, and T. Schoenemann. Performance characteristics and dielectric conditions of a wet electrostatic precipitator application for tar removal. In 21th EU Biomass Conference and Exhibition, 3-6 June 2013, Copenhagen, Denmark, pages 789794, 2013, DOI: 10.5071/21stEUBCE2013-2CV.3.14. ISBN: 978-88-89407-53-0. [4]

- S. Arumugam, P. Schröder, Y. Neubauer, and T. Schoenemann. An experimental study on electrostatic precipitator with tar contaminated hv insulator through UHF based PD tests. In 18th International Symposium on High Voltage Engineering, 25-30 August 2013, Seoul, Korea, pages 12341239, 2013. [107]
- S. Arumugam, P. Schröder, Y. Neubauer, S. Gorchakov, K.-D. Weltmann, and T. Schoenemann. Electrical discharge on the condensable hydrocarbons under the influence of dc voltage: An experimental approach. In 20th International Conference on Gas Discharges and Applications, 6-11 Juli 2014, Orleans, France, pages 630-636, 2014. [108]
- S. Arumugam, P. Schröder, Y. Neubauer, and T. Schoenemann. Dielectric and partial discharge investigations on ceramic insulator contaminated with condensable hydrocarbons. IEEE Transactions on Dielectrics and Electrical Insulation Special Issue, 21(6):25122524, 2014, DOI: 10.1109/T-DEI.2014.004553. [3]
- P. Schröder, Y. Neubauer, T. Schoenemann, and S. Arumugam. Quasi-phase resolved partial discharge pattern analysis of surface discharges arising on the tar polluted porcelain bushing of an electrostatic precipitator unit under high voltage DC. Engineering Reports, 2021, DOI: 10.1002/eng2.12379.

Chapter 1 introduces into the fundamental technical problem of sustainable energy solution based on gasification technology addressing the research problem of the formation of tar and its reliable removal from producer gas before its utilization [3, 4, 8, 15, 16].

Chapter 2 provides the fundamentals of biomass gasification and the removal of tar from producer gas and contains information already published in the paper [4, 8, 15, 16].

Chapter 4 provides the procedures and results of the investigation on test samples and contains information already published in the paper [3, 63, 66, 107, 108].

Chapter 5 provides the procedures and results of the experimental validation conducted on a laboratory scaled wet type ESP unit and contains information already published in the paper [3, 63, 66, 107, 108].

List of Figures

2.1	Schematic of an biomass power plant based on the gasification technique.	7
2.2	GC/MS reconstructed ion chromatogram from an online producer gas measurement.	8
2.3	Biomass gasifier in sequence with 2 ESP units for removal of heavy tar (1st stage) and light oil (2nd stage).	11
2.4	Reconstructed GC/MS ion chromatogram from an online tar analysis of biomass gasifier producer gas. (a): Raw gas sampled at the ESP inlet. (b): Clean gas sampled at the ESP outlet.	17
2.5	Overview of operational and design based influencing factors from producer gas cleaning causing insulator surface pollution.	18
3.1	Photo of the test sample B that was part of an actual HV insulator with severe surface deposition of tar.	23
3.2	Three-dimensional sketch of the test electrode arrangement for measuring the dielectric response on the surface of the test samples.	24
3.3	Photo of the test insulator porcelain no. CB3M.	25
3.4	Photo of the Megger MIT 1020/2 DC insulation resistance tester.	30
3.5	Photo of the Dirana (dielectric response analyzer).	31
3.6	RC parallel circuit of the dielectric loss factor ($\tan(\delta)$). (a): Equivalent circuit diagram. (b): Voltage and current curve. (c): Vector diagram in the complex plain.	32
3.7	Frequency dependent resonance and relaxation behavior of a dielectric material. Top: Real part $\epsilon'_r(\omega)$ (dispersion spectrum). Bottom: Imaginary part $\epsilon''_r(\omega)$ (loss spectrum).	36
3.8	Block diagram of an advanced digital PD measuring system.	38
3.9	Frequency band-width of conventional, VHF and UHF PD analysis.	38
3.10	Photo of the partial discharge measurement and analysis device (MPD 600) and the optic fiber bus controller interface (MCU 502).	39
3.11	Photo of the LDS-6-UHF PD measurement system.	40
4.1	Schematic of the dielectric response test setup. (a): Time domain. (b): Frequency domain.	43

4.2	Photo of the dielectric response test setup. (a): Time domain. (b): Frequency domain.	44
4.3	DC insulation resistance of test sample A and B measured at 5 kV.	45
4.4	AC Impedance of test sample A and B measured at 200 V.	46
4.5	Loss factor of the clean and tar-coated test samples.	47
4.6	Complex capacitance of the clean and tar-coated test samples.	48
4.7	Test setup for measuring the electrical discharges (PD) on the surface of test sample A and B under AC test voltage.	50
4.8	Schematic of the PD test setup under AC test voltage (shown in Figure 4.7).	51
4.9	Calibration setup of the PD AC test circuit.	52
4.10	Schematic of the setup used for calibration of PD AC test circuit (shown in Figure 4.9).	52
4.11	PRPD pattern of test sample B measured at 4.96 kV (PD level of 594.4 pC).	53
4.12	PD signal waveform in time and frequency domain. (a): Baseline in time domain (test sample A). (b): Calibration pulse in time domain (test sample A). (c): PD signal in time domain (test sample B). (d): Baseline in frequency domain. (e): Calibration pulse in frequency domain. (f): PD signal in frequency domain.	54
4.13	Photo of the PD DC test setup.	56
4.14	Schematic of the PD DC test setup (shown in Figure 4.13).	57
4.15	Wave shape of the DC test voltage.	57
4.16	Schematic of the calibration setup of the PD DC measuring circuit.	58
4.17	Calibration pulse of PD DC test circuit on the test sample A. (a): QPRPD pattern. (b): 3PARD diagram.	59
4.18	QPRPD pattern of test sample B under positive DC test voltage measured at + 8.1 kV DC (PD level of 358 pC).	60
4.19	QPRPD pattern of the electrical discharges on the test sample B at + 10.4 kV DC (PD level of 623 pC).	60
4.20	Charge-time (q-t) characteristics of intermittent electrical discharges on the test sample B measured at + 10.4 kV DC.	61
4.21	QPRPD pattern of electrical discharges on the test sample B measured at - 6.9 kV DC (PD level of 46.8 pC).	62
4.22	QPRPD pattern of electrical discharges on the test sample B measured at - 8.1 kV DC (PD level of 144.2 pC).	63
4.23	Charge-time (q-t) characteristics of continuous electrical discharges on the sample B measured at - 10.4 kV DC.	63
4.24	3PARD diagram of electrical discharges on the test sample B. (a): Measured at + 8.1 kV DC. (b): Measured at - 6.9 kV DC.	64

4.25	Frequency response of the broadband UHF coupler LDWS-T (top line).	65
4.26	Schematic of the test setup used for measuring UHF PD signals on the test sample B.	66
4.27	Time and frequency representation of UHF pulse used for performance check of UHF PD measuring circuit. (a): Time domain. (b): Frequency domain.	67
4.28	UHF PD signal pertaining to the electrical discharges arising on the surface of the tar contaminated broken insulator sample. (a) Real time representation at test voltage of 3 kV. (b) Real time representation at test voltage of 5 kV. (c) Frequency content at test voltage of 3 kV. (d) Frequency content at test voltage of 5 kV.	68
4.29	Test rig used for housing the bottom half of the test insulators during the measurements.	69
4.30	Time dependent dielectric response of the test insulator.	70
4.31	Loss factor ($\tan(\delta)$) of the test insulator installed in the test rig.	71
4.32	Frequency dependent dielectric response of the test insulator installed in the test rig. (a) AC impedance. (b) Capacitance.	72
4.33	Imaginary part $\epsilon_r''(\omega)$ of complex dielectric permittivity.	73
4.34	Real part $\epsilon_r'(\omega)$ of the complex permittivity.	73
4.35	Complex relative permittivity of test insulator under baseline condition.	74
4.36	Complex relative permittivity of test insulator under tar-coated surface condition.	75
4.37	Complex relative permittivity of test insulator under water-sprayed surface condition.	76
4.38	Time and frequency domain of the PD signals that arise on the clean (test insulator A.1) and with tar contaminated surface (test insulator A.3) measured at 3 kV AC. (a) Time domain of the test insulator A.1. (b) PD signal in time domain of the test insulator A.3. (c) Frequency domain representation of A.1. (d) Frequency domain representation of A.3.	77
5.1	Flowchart of laboratory scaled fluidized bed biomass gasification plant.	79
5.2	Wet ESP unit involved for experimental validation.	81
5.3	ESP voltage-current curve.	82
5.4	ESP unit voltage-current-curve.	83
5.5	Operating voltage and current of ESP unit with tar contaminated ceramic insulator. (a) Voltage. (b) Current.	84

5.6	Photo of the dielectric response test setup. Left: Time domain analysis (MIT 1020). Right: Frequency domain analysis (DIRANA).	85
5.7	Schematic of test setup used to measure the dielectric response of test insulator installed in the test rig and the wet ESP unit over a wide range of time (a) and frequency (b).	85
5.8	Time dependent dielectric response (DC insulation resistance) of clean and tar polluted surface of an actual ceramic insulator installed in a wet ESP unit measured over a wide time span. (a) Clean and dry surface. (b) Severe tar polluted surface.	86
5.9	Frequency dependent AC impedance of a ceramic insulator installed in a wet ESP unit. (a) Clean/dry surface condition. (b) Severely contaminated surface condition.	87
5.10	Frequency dependent loss factor ($\tan(\delta)$) of a ceramic insulator installed in a wet ESP unit. (a) Clean and dry surface condition. (b) Tar polluted surface condition.	88
5.11	Frequency dependent capacitance of a ceramic insulator installed in a wet ESP unit. (a) Clean and dry surface condition. (b) Tar polluted surface condition.	89
5.12	Online PD test setup. Left: Photo. Right: Schematic.	91
5.13	QPRPD pattern of baseline noise during ESP unit open-circuited measured at - 35 kV DC (PD level of 1.65 pC).	91
5.14	QPRPD pattern of the ESP unit with a tar polluted HV insulator surface measured at 5 kV DC (PD level of 38.9 pC).	92
5.15	QPRPD pattern of the ESP unit after 4 hrs of insulator surface heating measured at 15 kV DC (PD level of 60.5 pC).	93
5.16	QPRPD pattern of the ESP unit after 6 hrs of insulator surface heating measured at 20 kV DC (PD level of 129.1 pC).	94
5.17	Frequency domain information of QPRPD signals. (a): Tar polluted HV insulator surface measured at 5 kV DC. (b): HV insulator heated for 4 hrs measured at 15 kV DC. (c): HV insulator heated for 6 hrs measured at 20 kV DC.	95
5.18	Photo of the test setup used for measuring the UHF based PD signals from an ESP unit. (a): ESP unit. (b): UHF PD Sensor location at the ESP vessel. (c): LDS-6-UHF PD detector unit.	96
5.19	Schematic of test setup (shown in Figure 5.18) used for online measurements of UHF based PD activity on the surface of an actual ceramic insulator installed in a wet ESP unit.	96
5.20	UHF pulse of 5 V used for the performance check of PD measuring circuit.	98
5.21	UHF pulse plot recorded during performance check of PD measuring circuit.	99

5.22	UHF pattern (related to Figure 5.21) manifested by the UHF pulse during the performance check of PD measuring circuit.	99
5.23	ESP U-I-curve during N_2 flushing.	100
5.24	ESP U-I-curve during producer gas cleaning.	101
5.25	UHF PD pulse plot line pattern of the ESP unit during open-circuit operation at - 35 kV.	102
5.26	UHF PD pattern of the ESP unit during open-circuit operation at - 35 kV.	103
5.27	UHF PD pattern measured from the ESP unit in operation (33 kV and 8 mA) during N_2 flushing.	104
5.28	UHF PD pattern measured from the ESP unit in operation (32 kV, 6 mA) during producer gas cleaning.	104
5.29	UHF PD pulse plot line pattern measured from the ESP unit in operation (33 kV and 8 mA) during N_2 flushing.	105
5.30	UHF PD pulse plot line pattern measured from the ESP unit in operation (33 kV and 8 mA) during N_2 flushing.	106
5.31	UHF pulse plot line pattern of ESP corona measured during producer gas cleaning.	106
5.32	UHF pulse plot line pattern of surface discharges and sparks measured during producer gas cleaning.	107

List of Tables

3.1	Overview of test objects applied in the present thesis.	27
3.2	Overview of measurements taken from the respective test objects. .	28

Abbreviations

AC	Alternating Current
DC	Direct Current
DIRANA	Dielectric Response Analyzer
DSO	Digital Storage Oscilloscope
ESP	Electrostatic Precipitator
FDS	Frequency Domain Spectroscopy
GC	Gas-phase Chromatograph
GIS	Gas Insulated Switchgear
HFCT	High Frequency Current Transformer
HF	High frequency
HV	High Voltage
I_A	Absorption Current
I_C	Charging Current
I_L	Leakage Current
I_R	Insulation Resistance
LFD	Low frequency dispersion
MS	Mass Spectrometer
PD	Partial Discharge
PDM	Partial Discharge Measurement
PRPD	Phase Resolved Partial Discharge
p.u.	Per Unit
QPRPD	Quasi-Phase Resolved Partial Discharge
RF	Radio Frequency
SPA	Solid Phase Adsorption
UHF	Ultra High Frequency
VHF	Very High Frequency
N₂	Nitrogen
O₂	Oxygen

Q_a	Apparent Charge
3PARD	3-Phase Amplitude Relation Diagram

Abstract

Sustainable Energy, free from fossil fuels, has recently emerged as environment-friendly and climate-friendly solution. Naturally, it has become the primary *motto* of European environmental policy and the energy industry. Pertaining developments are tremendous and have resulted in the advent of modern methods, technological advancements and better environmental protection schemes. Amongst all, biomass power generation schemes have received wide attention and popularity and are employed together with other sustainable energy options such as wind energy, solar energy, geothermal energy and hydro energy to secure a safe, stable and affordable energy supply. A biomass based power generation plant applying gasification mainly consists of gasifier for the generation of producer gas, several apparatus such as filter, scrubber, cooler, Electrostatic Precipitator (ESP), etc. for reliable gas cleaning, and the subsequent utilization unit (gas engine, generator set, etc.) that converts the gas energy into green electrical energy. Such multi-stage arrangements are necessary to ensure the cleanliness of producer gas for its unrestricted conversion into clean electric power and to maintain a clean environment.

Despite their importance and popularity, certain aspects of the downstream equipment used for the removal of mixtures of organic compounds (collectively known as tar), such as protection, cleaning, maintenance, etc., are not dealt with adequate care and attention. In particular, the maintenance strategies of the tar ESP units have been the same for several decades without any significant improvement. The conditions on the ceramic insulators, which can severely restrict the ESP performance, are totally ignored until their permanent failure. An attempt to monitor their condition will help in improving the operating condition of an ESP unit, thereby ensuring the cleanliness of producer gas before its energetic utilization, henceforth reaching the goal of clean power generation. To achieve this, it is necessary to understand, at-least in macroscopic scale, the possible constituents in producer gas, their electrical characteristics and their influence on the dielectric integrity of the ceramic insulator and on the operating condition of an ESP unit. This forms the subject matter of this thesis.

It is certain that the dielectric condition of ceramic insulators of an ESP unit has decisive influence on its performance and cleaning efficiency. Naturally, exercising one or more condition based monitoring methods on pertinent insulators might help to initiate preventive measures at an early stage. The currently practiced maintenance procedures on ESP units are not paying much attention in ensuring the dielectric integrity of the ceramic insulators. In most cases, the ESP unit is

operated until the failure of its insulator, after which the complete arrangement (ceramic feed-through insulator and the suspended discharge electrode) is replaced. The main reason for the dielectric failure is identified as the deposition of tar on the exposed surface of the insulator. These condensable compounds that are present in the producer gas have to be removed reliably since their presence impairs the dielectric condition of the insulator, thereby limiting the performance of the ESP unit and compromising the operation of power conversion equipment. Early detection of such tar depositions would clearly provide an opportunity to prevent premature failure of the insulator. The respective cleaning measures could be simplified and the severity of the threat level (to human being and to the environment) arising due to the handling and disposal of hazardous waste materials could be minimized. In this context, preliminary information regarding electric discharges on outdoor insulators and quantification of their pollution level are already available. At the same time, the electrical behavior of condensable hydrocarbon and hetero-cyclic compounds (a few of these species are di-polar in nature) and their influence on dielectric quality of ceramic insulator, a synonym for insulation condition, remains unclear. It forms the primary aim of this thesis to explore these factors. It is believed that such an investigation provides an opportunity to prevent premature failure and to help in gaining knowledge about the electrical characteristics of tar.

Summarizing all, the present thesis investigates the following objectives:

- *Determining the influence of tar on the dielectric integrity of the ceramic insulator and the pertinent impact of tar that is deposited on the insulator surface on the operating condition and performance of a wet ESP unit.*
- *Gaining a macroscopical insight in the collective dielectric behavior of a complex mixture of tar that is deposited on the surface of the ceramic insulator.*

More details regarding the test objects, analytical equipment, experimental setup, inferences and conclusions drawn are provided in the respective chapters of the thesis.

Zusammenfassung

Nachhaltige Energie, frei von fossilen Brennstoffen, hat sich in jüngster Zeit zu der idealen umwelt- und klimafreundlichen Technologie entwickelt. Dabei ist Nachhaltigkeit zu einer der wichtigsten Konzepte der europäischen Umweltpolitik und Energiewirtschaft geworden. Die nachhaltigen Entwicklungen bieten immenses Potential und haben zu moderneren und nachhaltigeren Methoden, technologischen Weiterentwicklungen und verbesserten Umweltschutzmaßnahmen geführt. Konzepte zur Stromerzeugung aus Biomasse haben große Aufmerksamkeit und Beliebtheit erhalten und werden zusammen mit anderen nachhaltigen Optionen der Energiegewinnung (nämlich Windenergie, Solarenergie, Erdwärme und Wasserkraft) eingesetzt, um eine sichere, stabile und bezahlbare Energieversorgung zu gewährleisten. Biomassekraftwerke, basierend auf der Vergasungstechnik, bestehen im Wesentlichen aus dem Vergasungsreaktor zur Produktgaserzeugung, mehreren Gasbehandlungsschritten wie Filter, Wäscher, Kühler, Elektrofilter usw., die das Produktgas reinigen, während die nachgeschalteten Aggregate (Gasmotor und Generator) das niederkalorische Produktgas in CO_2 neutrale elektrische Energie verstromen. Die mehrstufigen Abscheidetechniken zur Produktgasreinigung sind erforderlich, um die uneingeschränkte Wandlung des Produktgases in Energie zu gewährleisten und um eine saubere Umwelt aufrechtzuerhalten.

Trotz der Bedeutung und Beliebtheit der Biomassekraftwerke werden bestimmte Aspekte der Kraftwerkskomponenten, wie Schutz-, Reinigungs- und Wartungsstrategien, die zur Abscheidung der kondensierbaren Kohlenwasserstoffverbindungen (allgemein unter dem Begriff „Teer“ zusammengefasst) eingesetzt werden, nicht mit der erforderlichen Sorgfalt und nicht mit dem erforderlichen Interesse behandelt. Insbesondere die Instandhaltungsstrategien von Elektrofilteranlagen sind seit mehreren Jahrzehnten ohne nennenswerte Verbesserungen unverändert. Dem Zustand der keramischen Isolatoren der im erheblichen Maße die Elektrofilterleistung beeinträchtigt wird kaum Beachtung geschenkt, die Isolatoren werden hingegen zumeist bis zum dauerhaften Versagen betrieben. Das Bestreben, den Zustand der Isolatoren zu überwachen, wird helfen, den Betriebszustand von Elektrofiltern zu verbessern, um dadurch die Reinheit der Produktgase vor deren energetischen Nutzung sicherzustellen und somit das Ziel einer sauberen Energieerzeugung zu erreichen. Um dies zu erreichen, ist es zumindest auf makroskopischer Ebene erforderlich, die möglichen Bestandteile im Produktgas von Biomassevergasern, deren elektrische Eigenschaften und deren Einfluss auf die dielektrische Integrität von keramischen Hochspannungsisolatoren sowie auf den Betriebszustand von Elektrofilteranlagen zu verstehen. Dies ist das Ziel der vorliegenden Arbeit.

Zweifelsfrei hat der dielektrische Zustand keramischer Stütz- und Durchführungsisolatoren von Elektrofilteranlagen einen maßgebenden Einfluss auf deren Leistung und die Reinigungswirkung. Daher ist es selbstverständlich zu erwarten, dass eine zustandsorientierte Überwachungsmethode, oder mehrere zustandsorientierte Überwachungsmethoden, auf die entsprechenden Isolatoren angewendet werden, wodurch Präventivmaßnahmen bereits in einem frühen Stadium eingeleitet werden können. Derzeitig praktizierte Instandhaltungsverfahren an Elektrofilteranlagen schenken der Gewährleistung der dielektrischen Unversehrtheit von keramischen Isolatoren keine große Aufmerksamkeit. In den meisten Fällen wird ein Elektrofilter bis zum Ausfall eines Isolators betrieben, wonach der betreffende Isolator ausgetauscht werden muss. Die Hauptursache für das dielektrische Versagen sind Ablagerungen einer Vielzahl kondensierbarer Kohlenwasserstoffe auf der gasberührten Oberfläche der Isolatoren. Diese Kohlenwasserstoffe, die im Vergaser-Produktgas vorhanden sind, müssen vor der energetischen Verwertung aus dem Gas entfernt werden, da deren Anwesenheit den dielektrischen Zustand der Isolatoren, die Leistung der Elektrofilteranlage und den Betrieb der Energie-Wandlungseinrichtungen beeinträchtigt. Die frühzeitige Erkennung von solchen Verschmutzungen bietet eine Möglichkeit, vorzeitiges Versagen der Isolatoren zu verhindern. Die erforderlichen Reinigungsmaßnahmen könnten somit vereinfacht werden und das Ausmaß von Gefahrstoffwirkungen (auf Mensch und Umwelt), bedingt durch Umgang mit gefährlichen Abfällen und Entsorgung dieser Abfälle, könnte minimiert werden. Für Freiluftisolatoren, die gewöhnlichen Umwelteinflüssen ausgesetzt sind, existieren verschiedene Verfahren zur Erfassung von elektrischen Entladungen und verschiedene Modelle für die Bewertung ihres Verschmutzungsgrades. Zugleich ist das elektrische Verhalten von kondensierbaren Kohlenwasserstoffen und ihrem Einfluss auf die dielektrische Qualität der Keramikisolatoren weitestgehend unklar. Das primäre Ziel der vorliegenden Arbeit ist es, diese Faktoren zu untersuchen. Es wird davon ausgegangen, dass diese Untersuchung Möglichkeiten zum Verhindern von vorzeitigen Fehlern und Anlagenausfällen bereitstellen kann und hilft, Erkenntnisse über die elektrischen Eigenschaften von kondensierbaren Kohlenwasserstoffen zu erlangen.

Die vorliegende Arbeit untersucht zusammengefasst die folgenden Aspekte:

- Ermittlung des Einflusses von Teer auf den dielektrischen Zustand und die Qualität von keramischen Isolatoren und die damit verbundenen Auswirkungen auf den Betriebszustand und die Leistung von Elektrofilteranlagen.
- Erkenntnisse über das makroskopische, kollektive dielektrische Verhalten von kondensierten überwiegend aromatischen und heterozyklischen Kohlenwasserstoffverbindungen, die auf der Oberfläche von keramischen Isolatoren abgelagert sind.

Weitere Details hinsichtlich der Prüfanordnungen, Versuchsdurchführungen, Ergebnisse und Rückschlüsse sind in den entsprechenden Kapiteln dieser Arbeit enthalten.

Contents

Acknowledgment	ii
	Page
List of Publications	iii
List of Figures	ix
List of Tables	x
Abbreviations	xi
Abstract	xiii
Zusammenfassung	xv
1 Introduction	1
1.1 Sustainable Energy Solution	1
1.2 Objectives, Structure of the Thesis and Limitations	3
1.2.1 Objectives	3
1.2.2 Structure of the Thesis	3
1.2.3 Limitations	5
2 Background	6
2.1 Biomass Power Plants Based on Gasification	6
2.1.1 Producer Gas and its Contamination	7
2.1.2 Classification of Tar in Producer Gas	8
2.1.3 Significance of Cleaning Producer Gas	9
2.1.4 Producer Gas Cleaning Procedures	10
2.2 Definition and Properties of Tar	11
2.2.1 Definition of Tar	12
2.2.2 Electrical Properties of Tar Constituents	12
2.2.3 Factors that Affect the Electrical Characteristics of Tar	13
2.2.4 Measurement of Electrical Conductivity of Aromatic Com- pounds	14
2.3 ESP Tar Removal Efficiency	14
2.3.1 Present Maintenance Procedures of ESP Units	15

2.3.2	Performance of Electrostatic Tar Precipitator Units	15
2.3.3	Tar Sampling and Tar Analysis Methods	16
2.3.4	Online Tar Measurement	17
2.4	The Course of Tar Deposition on an ESP High Voltage Insulator . .	18
2.4.1	Measures to prevent surface contamination	20
2.4.1.1	Mechanical Measures	21
2.4.1.2	Process Measures	21
3	Materials and Measurement Techniques	22
3.1	Test Objects	22
3.1.1	Test Samples	22
3.1.2	Electrode Arrangement	24
3.1.3	Test Insulator	25
3.2	Techniques for Dielectric Condition Measurement and PD Monitoring	29
3.2.1	Dielectric Response Analysis	29
3.2.1.1	Time Dependent Dielectric Response	29
3.2.1.2	Frequency Dependent Dielectric Response	31
3.2.2	Partial Discharge Analysis	36
3.2.2.1	Conventional PD Analysis	39
3.2.2.2	Non-conventional PD Analysis in UHF Range	40
4	Experiments on Samples	41
4.1	Procedure	41
4.2	Experiments on Test Samples	42
4.2.1	Dielectric Response Analysis	43
4.2.1.1	Dielectric Response in Time Domain	44
4.2.1.2	Dielectric Response in Frequency Domain	46
4.2.2	Partial Discharge Analysis	49
4.2.2.1	PD at AC Test Voltage	49
4.2.2.2	PD at DC Test Voltage	55
4.2.3	Non-conventional PD Analysis in UHF Range	64
4.2.3.1	Performance Check	66
4.2.3.2	Signal Analysis in Time and Frequency Domain	67
4.3	Experiments on Test Insulator	68
4.3.1	Test Insulator Arrangement	69
4.3.2	Dielectric Response Analysis	69
4.3.2.1	Dielectric Response in Time Domain	69
4.3.2.2	Dielectric Response in Frequency Domain	70
4.3.3	PD Signal Analysis in Time and Frequency Domain	76
5	Validation	78
5.1	Procedure	78
5.2	Electrostatic Tar Precipitator Unit	80
5.2.1	Conventional Operation Performance Monitoring	81
5.2.2	Recovery of Operational-Based Performance Loss	83
5.3	Dielectric Response Analysis	84
5.3.1	Dielectric Response in Time Domain	85

5.3.2	Dielectric Response in Frequency Domain	87
5.4	Partial Discharge Analysis	90
5.4.1	PD DC Performance Check	91
5.4.2	QPRPD Analysis	92
5.4.2.1	QPRPD Pattern Analysis	92
5.4.2.2	PD Information in Frequency Domain	94
5.5	Non-conventional PD Analysis in UHF Range	95
5.5.1	Performance Check	97
5.5.2	UHF PD Signal Analysis	100
5.5.2.1	ESP U-I-curve during UHF PD Measurements . . .	100
5.5.2.2	UHF PD Pattern Analysis	101
5.6	Inferences	107
6	Conclusion	109
6.1	Summary	109
6.2	Limitations and Future Scope	113
	References	115
	Appendix A	129
	Appendix B	131

Introduction

1.1 Sustainable Energy Solution

Utilization of solid biomass has the longest global tradition for production of thermal heat and has within the past 25 years emerged as a solution of sustainable energy and power generation [1]. The thermo-chemical conversion of biomass by gasification provides, compared to the combustion process, several advantages like high effectiveness and the usage of various solid biomass feedstock. Furthermore, producer gas generated through gasification is versatile in its applications for direct heat and power generation or its conversion into other gaseous or liquid secondary energy carriers. Besides these economic aspects, the biggest challenge of the gasification process is the unavoidable presence of tar in raw producer gas and its reliable removal. The producer gas flows into power generation plants, where the gas energy is converted into electrical energy [2]. In such a process, the most important requirement is to ensure the cleanliness of the producer gas in order to prevent contamination problems in the downstream equipment of a biomass power plant caused by several hydrocarbon and heterocyclic compounds that are condensable from its gaseous state [3, 4]. In other words, the power plant equipment downstream equipment of the gasifier such as scrubber, heat exchanger, cooler, electrostatic precipitator, gas engines, which are directly exposed to the producer gas, suffer severe contamination causing problems like plugging, fouling etc [5, 6].

Recent technological developments of modern control and management technologies have increased the efficiency of producer gas cleaning procedures, subsequently reducing the emission levels [7–9]. In this context, wet-type ESP units are well-known for over 100 years for their highly efficient removal of tar from town gas

and generator gas [10, 11]. The electrostatic precipitation technique is not only considered for its high efficiency, but also for its low pressure drop and low operating costs [12, 13]. The particles and aerosols that are present in the producer gas are electrically forced towards the collecting electrodes [7–9, 14]. In this way, problems like plugging and fouling that arise in producer gas utilization devices and equipment like gas engines, boilers, generators and other stand-alone power conversion devices are avoided. On the contrary, it is challenging achieving complete removal of tar from the producer gas even after the ESP unit has undergone design improvements, field optimization and performance-wise enhancement [5, 15, 16]. Inevitably, in particular the mono-aromatic compounds which manifest high vapor pressure like benzene, toluene, styrene and so on, escape the optimized electric field and deposit in their liquid state of aggregation on all the exposed surfaces, thereby causing problems in the downstream processing [4, 17, 18]. Even at producer gas temperatures of 30 °C and 40 °C. In consequence of surface deposition on the High Voltage (HV) insulator, its dielectric surface condition is sooner or later compromised, thus the performance of the ESP unit is cumulatively limited.

Naturally, the ESP unit, being an important member in the gas cleaning process, requires more attention to maintain high cleaning efficiency and emission control levels since an unnoticed degradation of its removal efficiency provokes in the short or medium term, pollution of the downstream equipment.

Summarizing all, the following questions naturally arise:

- Although certain organic compounds of tar manifest dielectric properties, why does the insulator fail?
- Is it possible to quantify the dielectric quality of a ceramic insulator in polluted condition, contaminated with tar, by employing offline and /or online diagnostic test methods?
- What would be the collective response of tar forming compounds, aerosols of condensed water and quench liquid over a wide span of time and frequency?

This thesis intends to find out the answers for the above questions. It is believed that gaining such knowledge will help in enhancing cleaning measures and in improving the ESP performance, thereby ensuring the purity of producer gas and thus its reliable utilization.

1.2 Objectives, Structure of the Thesis and Limitations

1.2.1 Objectives

The objectives of the thesis are broadly divided into three, namely:

- *Determining the influence of tar on the dielectric integrity of the ceramic insulator and the pertinent impact of tar that is deposited on the insulator surface on the operating condition and performance of a wet ESP unit.*
- *Gaining a macroscopical insight in the collective dielectric behavior of a complex mixture of tar that is deposited on the surface of the ceramic insulator.*

Details of the respective procedures, test methods and results are presented in six chapters.

1.2.2 Structure of the Thesis

Chapter 1 provides the background of the presented research problem. A brief introduction reports the problems associated with gasification based power conversion, producer gas cleaning and in this regard the corresponding technological and operational difficulties of an ESP unit within a gasification unit applied for the removal of tar. Using this, the impact of tar onto the dielectric condition of ceramic insulators and the performance of an ESP unit is presented. Subsequently, the identified research problem and the possibilities of resolving the same are explored. In addition, the objectives, structure and limitations of the thesis are presented.

Chapter 2 presents a brief introduction into the fundamentals of biomass gasification, into the possible organic contamination present in producer gas of a biomass based power plant and into the significance of an ESP unit in the gas cleaning process. The tar removal efficiency of an ESP unit and the possible species of tar that can be expected in the producer gas even after cleaning are discussed. A brief review about the classification of aromatic compounds and the definition of tar that is applied in this thesis are presented. Furthermore, the electrical properties of pure aromatic hydrocarbon compounds that are typical constituents of tar and its dipole moments are reviewed. In addition to this, the present know-how

and concepts that are presently used by the industry with regard to the common mechanical measures, process measures and maintenance procedures of ESP units are briefly presented.

Chapter 3 presents an overview of the involved test objects. Furthermore, the analytical equipment applied for measuring the surface condition of the test samples and test bushings under laboratory condition as well as the condition of the insulators installed in an ESP unit through offline and online test methods are briefly reported.

Chapter 4 presents the experimental investigations initiated on a test sample that has been extracted from an actual ceramic insulator, which was contaminated mainly with mono-aromatic hydrocarbon compounds from producer gas during its service time in an ESP unit. The experiments include dielectric response analysis methods over a wide span of time and frequency. The surface characteristics of the samples of ceramic insulators before and after contamination are investigated. This implies measuring the time and frequency dependency of the dielectric properties, such as Direct Current (DC) insulation resistance, loss factor, capacitance and permittivity, of the clean and the contaminated samples and the characteristics of the electrical discharges that arise on the insulator surface with respect to its different surface pollution condition. The insulation material reference values of dielectric surface properties are gained on a virgin test sample with a clean and dry surface. Once this is accomplished, the findings of the test samples are experimentally cross-verified with a test insulator under laboratory condition. It follows that tests are conducted with test bushings that are identical to the one installed in the ESP unit and that are installed in a laboratory test rig designed following the installation situation of the insulator in the top chamber of the ESP unit. The electrical response of the test bushings is investigated under clean and manually contaminated surface conditions.

In **Chapter 5**, the experimental setup of a laboratory scale biomass gasifier and an ESP unit that are used for validation are introduced and the analytical procedure is presented. The findings of the test objects gained according to Chapter 4 are experimentally validated on an actual ceramic insulator installed in an ESP unit that operates in sequence with a fluidized bed gasifier. In addition to this, the collective response of the HV insulator under different pollution conditions is analyzed through online and offline measurement methods. Summarizing all, the results from the experiments on test samples are discussed and compared with the actual data obtained from a laboratory scale wet ESP unit.

Finally, **Chapter 6** summarizes the main results and the conclusions drawn from the present research work. Subsequently, the current limitations of the employed methodologies are presented and the future work that could be continued in this

direction is summarized.

In summary, it is believed that the findings of the present thesis will help not only to improve the performance of ESP units, but also to enhance current maintenance procedures of ESP units that are applied to them for removal of tar from biomass power plants. After all, the rationale of a diagnostic test is to initiate preventive action well before a system failure. In this regard, the present thesis gains its importance to provide the results of analytical procedures for monitoring the electrical condition of a HV insulator installed in an ESP unit to enable early identification of surface deposition leading into fault condition sooner or later. This provides on the one hand the possibility for appropriate maintenance activities, and on the other hand minimizes service costs and limits the need for disposal of polluted equipment.

1.2.3 Limitations

These are some limitations in the design of this thesis, which are listed below:

- All measurements are made under ambient temperature conditions while the actual gas temperature might be slightly higher.
- The possible species of tar relevant to the gasification of pine-wood chips is alone investigated here. In reality, several other species might arise from different feedstock material which is used for generation of producer gas.
- The apparent characteristics of a complex mixture of tar evolved from wood chips that are gasified in a fluidized bed reactor are alone investigated. In all, the attention is provided in understanding the collective behavior of these species using macroscopic methods.
- Since it is not possible to reproduce the same condition on a virgin HV test insulator surface that are investigated in section 5.4, viz. thickness and composition of the tar contamination layer, the Ultra High Frequency (UHF) based Partial Discharge (PD) analysis of section 5.5 is limited to the operation of the ESP unit equipped with a clean HV insulator.

Background

2.1 Biomass Power Plants Based on Gasification

The biomass-based power generation based on the gasification method involves three major stages, viz. gasification (production of producer gas), gas cleaning (removal of by-products like particles, ash and tar) and energetic utilization of the cleaned producer gas (conversion of low heating value fuel gas into electric power, e.g. by a pilot-injection gas engine combined with a generator). The underlying principle is schematically described in Figure 2.1 appropriately. Initially, the feedstock is suitably prepared from the biomass. After pre-treatment (e.g. milling, drying), the feedstock is fed into the gasifier unit where it is thermo-chemically converted into a fuel gas (producer gas) and other by-products such as gaseous aromatic compounds, solid charcoal and ash respectively. Since the main thermo-chemical conversion reaction like Boudouard reaction, steam gasification and steam reforming are endothermic in nature, the thermal energy for the conversion of the feedstock has to be provided either by exothermic reaction through partial combustion of feedstock amounts with the gasification agent, so-called allo-thermal process, or by an external source, so-called auto-thermal process. The generated producer gas further streams upwards into the gas cleaning unit where solid particles and ash are removed. After this cleaning procedure, the producer gas flows subsequently into a utilization unit where its caloric value is converted into mechanical energy driving a generator for the production of electric power. The thermal energy stored in the exhaust gas is further transferred by a heat exchanger for providing of thermal power.

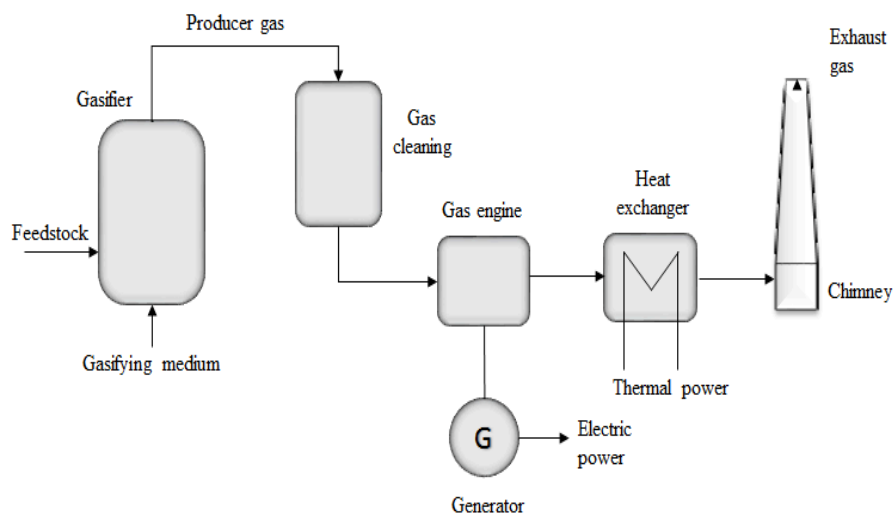


FIGURE 2.1: Schematic of an biomass power plant based on the gasification technique.

2.1.1 Producer Gas and its Contamination

The primary difficulty of producer gas cleaning is the reliable removal of tar that is inevitably present in the generated low heating value fuel gas or synthesis gas. The biomass, that is fed into the gasification reactor, reacts partly with the gasification agent, thereby providing the thermal energy for the degradation of cellulose, hemicellulose and lignin into smaller gaseous hydrocarbon molecules and permanent gas. The permanent gas consists of inert compounds like nitrogen (N_2), carbon dioxide (CO_2) and steam (H_2O_{steam}). Furthermore, producer gas contains gaseous compounds like hydrogen (H_2), methane (CH_4) and carbon monoxide (CO), which exhibit heating values of 10.112 MJ/kg for that of CO, 141.8 MJ/kg for that of H_2 and 55.5 MJ/kg for that of CH_4 , respectively. The producer gas also comprises several gaseous inorganic components such as ammonia (NH_3) and hydrogen cyanide (HCN), compounds of sulfur atoms bonded with hydrogen, oxygen or carbon like hydrogen sulfide (H_2S), sulfur dioxide (SO_2), carbon disulfide (CS_2) and carbonyl sulphide (COS) or chloride atoms like hydrogen chloride (HCl). All inorganic compounds are generally impurities which have to be removed to a certain amount out of the producer gas since each utilization unit has to be operated within its restriction of the applicable fuel. In addition to this, the producer gas also comprises amounts of several hetero-cyclic aromatic compounds, mainly with nitrogen or sulfur as hetero atom. Particularly sulfur containing hydrocarbon and aromatic compounds are well-known for its in-habitation of metal catalysts. The solid fraction of producer gas contains mainly char, carbon, soot, alkali metals and ash.

The formed gaseous hydrocarbon compounds consist of chain-like branched and unbranched aliphatic molecules that can contain one or more hetero-atoms, mono-cyclic or poly-cyclic aromatic molecules that can be either carbo-cyclic or hetero-cyclic. Figure 2.2 shows the possible species of condensable hydrocarbons (such as styrene, phenol, naphthalene etc.) that predominantly evolve with the producer gas during gasification of wood chips. Figure 2.2 is an outcome of a Gas-phase Chromatograph (GC)/Mass Spectrometer (MS) reconstructed ion chromatogram of an online producer gas tar measurement.

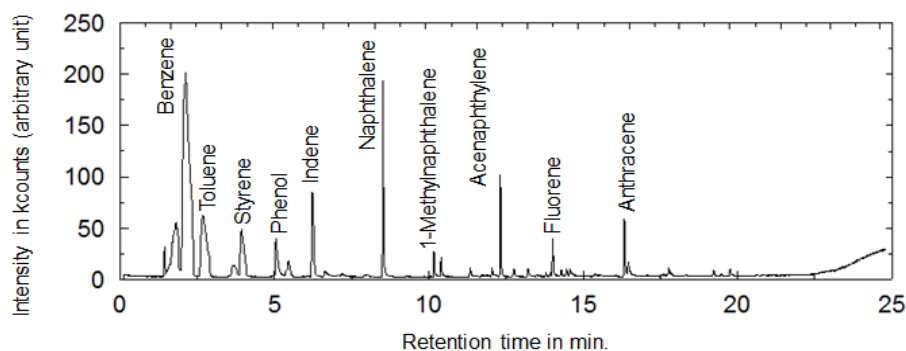


FIGURE 2.2: GC/MS reconstructed ion chromatogram from an online producer gas measurement.

The composition and the amounts of tar can be controlled, up to a certain extent, by proper pre-treatment of feedstock, by proper selection of type and design of gasifier, operating temperature, gasifying agent and in a minor degree depending on the raw material of biomass [6, 19]. Despite all, there will always remain a condensable fraction of aromatic hydrocarbon and hetero-cyclic compounds as well as their derivatives in the cleaned producer gas.

2.1.2 Classification of Tar in Producer Gas

Historically, tar was defined as all aromatic hydrocarbon and hetero-cyclic compounds that condensed from the producer gas. Nowadays, different definitions of tar exist that define tar related to technical or operational aspects like plugging or fouling [20–24]. An established distinction of tar groups the compounds into four categories related to its formation during the gasification and pyrolysis process [19, 25]. Another common distinction of tar species is the division into light tar and heavy tar [26]. The most common method of tar uses five groups [23, 27]. This classification subdivides the individual compounds, related to its molecular weight and physical properties like solubility in water, into five classes where light tar species are those with a molecular weight equal or less than that of anthracene

[23]. Class 1 tar species are molecules with high molecular mass that make them undetectable with the use of a gas-phase chromatograph [9, 23]. Class 2 tar are all heterogenic species comprising one or more hetero atom in the aromatic structure that induces a polar characteristic. Class 3 tar, 1-ring molecules represent the light hydrocarbon species that manifest solubility in water [9, 23]. Class 4 tar, 2-ring and 3-ring molecules represent the light polyaromatic hydrocarbon species. Class 5 being 4-ring and 5-ring aromatic species with a molecular mass greater than that of anthracene representing the heavy tar species that start condensing at high temperatures.

Franck et al. [20] described tar as "flüssige bis feste Erzeugnisse, die durch zersetzende thermische Behandlung organischer Naturstoffe gewonnen werden" ¹. Tar is always a mixture of various organic molecules containing estimated 10,000 chemical compounds of which so far less than half of have been identified [20, 28, 29]. Several fractions of tar, containing compounds with a molecular mass of benzene up to anthracene, that have been further processed by extraction and distillation into valuable raw materials for the chemical industry, were classified as oils and were in most cases not considered as tar in the past [29]. In the course of the decades, the historically-based term was in many cases adjusted with respect to economic or technical concerns. Under economical aspects, liquid fractions that can be processed into valuable raw materials ranging from light oil (beginning from the simplest mono-aromatic hydrocarbon compound: benzene) up to anthracene oil were used and only the amount of non-useful condensed compounds with higher molecular mass than that of anthracene was considered as tar [10]. An overview of the processing, technical procedures and obtained various raw materials exemplified by stone coal tar is given in [10, 20]. Nowadays, with respect to technical issues mainly the compounds causing problems in the downstream equipment through fouling and/or plugging are considered as highly problematic and therefore termed as tar.

2.1.3 Significance of Cleaning Producer Gas

The producer gas that is generated through the thermo-chemical conversion process of biomass in the gasification unit is streamed into the power-generation equipment or utilized for catalytic conversion into bio-fuels, but only after undergoing extensive gas cleaning procedures. Such cleaning procedures are necessary since the producer gas contains, as mentioned before, several species of organic contaminants which are condensable in nature and which are normally considered as

¹Citation translated: "liquid up to semi-solid products obtained by decomposing thermal treatment of natural products"

highly problematic substances [6, 17]. These species purely depend on the type of feedstock, type and design of gasification reactor, gasifying agent, operating conditions etc. and invariably emerge during the gasification process. Besides the organic compounds, producer gas contains further amounts of solid particles and several other inorganic gaseous species. In all, producer gas has to undergo sufficiently-designed gas cleaning steps in order to reach the acceptable level of purity before its further processing. A proven practice is to employ an ESP unit in cleaning the producer gas [2, 10, 30–34]. Being highly efficient in removal of dust, aerosols, particles of certain dimension and removal of multiple species of tar, ESP units have become an integral component of conventional industrial processes and emission control applications [2, 14, 30, 35–37].

2.1.4 Producer Gas Cleaning Procedures

The producer gas that is generated by thermo-chemical conversion in a gasification unit requires, depending on the kind of its utilization, a more or less extensive treatment to meet the needs of gas purity determined by the limitation of the utilization aggregates [38, 39]. In this regard, the primary objective is to ensure a stable and reliable process, therefore different methods of gas cleaning are applied. Beside the limitation of solid particle concentration present in the gaseous phase, the major restriction of utilization aggregates is their permissible value of condensable compounds when producer gas has to be utilized at temperatures below 350-400 °C.

The cleaning procedures applied to producer gas can in general be subdivided into the mechanical/physical removal of solid particles and ash and the removal or conversion of tar by means of mechanical/physical, catalytic or thermal methods, which can be further subdivided into primary and secondary methods [40, 41]. Separation of solid particles and ash is performed above the dew points of water and tar at temperatures around 400 °C or higher and is in general termed as hot-gas filtration, where ceramic or metallic candle filter, cyclone or dry ESP units are applied [42, 43]. The hot producer gas, free from solid particles, is then further cleaned to lower the level of tar by procedures like partial oxidation by free oxygen, thermal decomposition by micro-waves or by catalytic cracking [40]. The oldest procedure for the removal of tar is cooling of producer gas phase and the subsequent mechanical/physical removal of tar by scrubbers, cyclone, sand filter or wet ESP units [39, 40, 42]. ESP units are applied for the removal of tar since around 100 years for the reason that they efficiently remove tar from producer gas. It is well-known since over five decades that two ESP units have to be applied in

sequence in combination with a gas cooling unit in between for a separate removal of heavy tar and light tar compounds, as shown in Figure 2.3 [34].

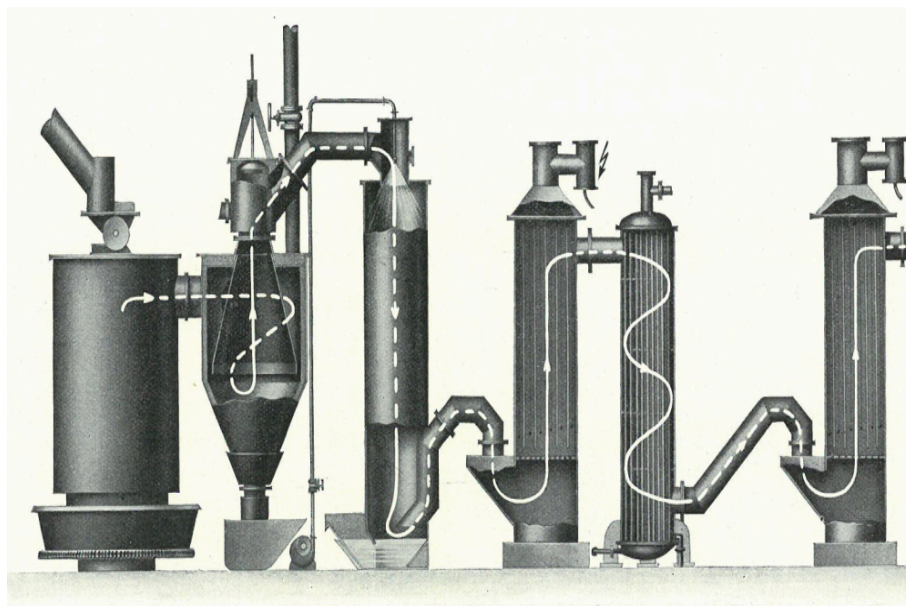


FIGURE 2.3: Biomass gasifier in sequence with 2 ESP units for removal of heavy tar (1st stage) and light oil (2nd stage).

The electrostatic precipitation technique is applied for its high efficiency, but also for its low pressure drop and low operating cost [12, 13]. The particles and aerosols that are present in the producer gas are electrically forced towards the collecting electrodes [7–9, 14]. In this way, problems like plugging and fouling that arise in end-user devices and equipment like gas engines, boilers, generators and other stand-alone power conversion devices can be avoided. It is found quite difficult to achieve a complete removal of tar from the producer gas even after the ESP unit has undergone design improvements, field optimization and performance-wise enhancement [5, 15, 16].

2.2 Definition and Properties of Tar

The gaseous phase evolving through gasification contains, aside from permanent gas compounds, solid particles, ash and several species of metals also various organic hydrocarbon and hetero-cyclic compounds as well as their derivatives. The organic compounds form liquid aerosols and drops in consequence of condensation when the producer gas temperature drops to a certain value, since each compound is at an equilibrium with its temperature related saturation vapor pressure. A general term commonly used for describing this liquid condensed phase from producer

gas is tar. However, the collective term has different meanings since gasification technology is applied.

2.2.1 Definition of Tar

In this thesis, the entire amount of organic aromatic hydrocarbon and hetero-cyclic compounds that condenses from producer gas is in general collectively termed as tar, in its semi-liquid state up to highly viscous state of aggregation. In addition to this, also the compounds that are derived from the mono-, poly- and hetero-cyclic aromatic compounds due to substitution of one or more hydrogen atoms of the aromatic ring structure, like phenol, has to be considered as constituents of tar while they are in a liquid state of aggregation. Thus, all compounds present in producer gas exhibiting the ability of condensation as a consequence of a temperature drop are considered as possible constituents of tar and are in the following termed as condensable hydrocarbons and hetero-cyclics while they are in gaseous state. However, it depends on the producer gas temperature whether the individual compounds will condense and thus become a constituent of tar. Since most of the possible species present in tar exhibit hydrophobic characteristics, condensed steam of producer gas forms a two-phase system together with tar. In most cases tar contains a certain proportion of dissolved and unsolved water, however, by the definition of tar, water is not considered as one of its ingredients. In the further course of this thesis the term contaminant(s), hydrocarbons and hetero-cyclics are used as synonym for tar. The term light tar is in the context of this thesis used as a collective term for all aromatic compounds with a molecular weight below that of naphthalene (128.17 g/mol) since these compounds exhibit high vapor pressures causing comparably high concentrations in the gaseous phase also at ambient condition. Light tar represents the light oil and middle oil fractions of tar following the recommendation from *Lin* [29]. These compounds present in the producer gas in gaseous state are termed as condensable light tar.

2.2.2 Electrical Properties of Tar Constituents

The hydrocarbons are grouped into different classes, based on their functional groups, presence of hetero-atoms and on the bonding between hydrogen and carbon atoms. In addition to this, the details corresponding to electrical conductivity of single or individual species of hydrocarbons in its pure form are currently available. However, the same for multiple species altogether in a complex mixture are yet to be investigated [44]. Most of the available data are pertaining to transformer oil and its mixture with paraffin, olefin and naphthalene [44, 45]. Also,

the variation of electrical conductivity depends not only on temperature but also on the molecule structure of the hydrocarbon species [45, 46]. For instance, the electrical conductivity of paraffin, which form un-branched straight chains of hydrocarbons without side chains (homologous series), decreases with its increasing chain and branching in a straight molecule. At the same time, the presence of bond configuration (single, double, triple) increases the conductivity in the same (ascending) order [47].

It is reported in literature that few individual species of hydrocarbons such as toluene, styrene, phenol etc. are di-polar in nature in their pure form. The obtained values of the dipole moment (unit represented as *Debye* or abbreviated as D) of toluene show that it is around 0.4 D (refer to [48]), where the same of styrene is 0.13 D (refer to [49]), and for phenol it is close to 1.396 D (refer to [50]), while o-xylene is about 0.62 D (refer to [49]) and m-xylene is about 0.33 D (refer to [49]) respectively. At the same time, certain species like benzene, naphthalene, 1-methylnaphthalene etc. are individually uni-polar with a dipole moment of zero and which are in pure form non-conductive in nature (refer to [49]). However, multiple species of pure hydrocarbons altogether manifest entirely different dielectric properties in consequence of their mixture, complex bonding structure and molecular interaction, molecular reactions due to the presence of impurities like moisture and/or dissolved gases [47, 51]. An overview about the physical properties of the aromatic hydrocarbons that predominantly evolve due to the gasification of biomass along with its dielectric properties is given in Appendix A.

2.2.3 Factors that Affect the Electrical Characteristics of Tar

The electrical characteristics of hydrocarbons primarily depend on the level of purity of their species and on the condition of the medium/environment in which they are present [45, 47, 51–53]. For instance, the electrical conductivity of individual species of solid and liquid hydrocarbons increases with temperature and pressure up to a certain critical point [47]. At the same time, the conductivity of refrigerant species decreases with an increase of its dielectric constant value while the alcohol species shows an inverse trend where the conductivity increases with an increasing dielectric constant of the pertinent species [47]. Besides the possible impurities, the electrical conductivity of dielectric liquids are affected by light, cosmic radiation and ionization sources such as x-rays, β -rays etc. [47]. Additionally, the accuracy of measurement is highly dependent on the geometry of the measuring cell [51, 54]. It is recommended that a three-terminal measuring cell with a shielded electrode should be used in order to minimize the adverse effects of

side phenomena [54]. Furthermore, it is reported that the conductivity of mineral oil depends on the magnitude of the applied electric field [55]. The conductivity decreases with an increase of the applied field, reaches a minimum value as the field strength is close to 2 kV/mm and subsequently increases with the magnitude of the electric field. This behavior is in consonance with the findings reported in [56].

2.2.4 Measurement of Electrical Conductivity of Aromatic Compounds

Hydrocarbon liquids are dielectrics in nature with a specific conductance less than 10^4 pS/m [54]. The bulk electrical conductivity of hydrocarbon liquids like fuels, oils, additive solutions etc. indicates the presence of free-charge carriers which move under the influence of an electric field [51]. Such measurements require a well-designed test cell with shielded electrodes in order to avoid edge effects which is described in [54]. Two test methods viz., DC and Alternating Current (AC) techniques are employed while measuring the bulk electrical conductance in liquid hydrocarbons. The DC field method is preferred for measuring conductivity of hydrocarbon species [54]. At the same time, the influence of DC voltage on polarization and depolarization is limited to switch on and switch off and hence is usually neglected [54, 57].

2.3 ESP Tar Removal Efficiency

A wet ESP unit is known for its high cleaning efficiency (higher than 98 %) in removing tar from the producer gas [33, 34, 58–61]. However, in this context it has to be mentioned that the reported tar removal efficiency of 98 % has to be considered on the one hand with respect to the applied sampling method and on the other hand related to the definition of tar. In other words, the ESP removal efficiency depends on which compounds present in producer gas are considered as constituents of tar. ESP units are well-known for their high capability in removing solid particles and liquid aerosols from a gaseous phase. On the contrary, compounds in its gaseous state of aggregation pass the electric field of an ESP unit more or less unaffected. Since the sampling method that is applied to an ESP unit is based on gravimetric procedures in general, like sampling according to VDI 2066 or DIN 13284, it becomes clear that the quantities of compounds present in the

gaseous phase which exhibit high vapor pressures, in particular the mono-aromatic hydrocarbon compounds together with water vapor, are not taken into account by the applied sampling procedure. Thus, the reported collection efficiency of an ESP unit would be much lower if the quantities of compounds present in the gaseous phase are not neglected. *Seidenschnur et. al* reported an ESP removal efficiency related to tar of close to 87 % with the remark that around 13 % of the light tar compounds remain as vapor in the gaseous phase [10].

2.3.1 Present Maintenance Procedures of ESP Units

Currently practiced maintenance procedures mainly concentrate on cleaning the contamination that are collected in the collecting chamber. In most cases, the ESP unit is operated until the insulator suffers a serious failure. Such a condition might result in intermittent service of the ESP unit causing not only an economic impact, but also raising serious environmental concerns. Upon contamination, the surface of the support insulator is dried out to regain its dielectric quality. One solution is that the insulator compartments are air-blown, which is commonly applied to ESP units in a cement plant [62]. However, the same procedure to keep the insulator surface dry is applicable to an ESP unit in a gasification plant only by the use of inert purging gases like nitrogen, argon or carbon dioxide that further dilute the producer gas and thereby lowering its heating value. The surface heating elements is applied to keep insulator surfaces above the dew point [11, 62, 63]. Nevertheless, cleaning the surface of the insulator seems to be highly recommended, since the replacement of an insulator is a critical procedure [62]. A possible way to avoid such a condition is to constantly monitor the condition of the ceramic insulator installed in the ESP unit [7]. Until now, the possibilities of employing modern diagnostic test methods in quality assessment of ceramic insulators contaminated with tar are not thoroughly researched [7]. Perhaps the reason is to be sought in the of lack of information about the collective behavior of several species of condensable hydrocarbon and hetero-cyclic compounds [63].

2.3.2 Performance of Electrostatic Tar Precipitator Units

The performance and the removal efficiency of a wet ESP unit depends on several factors [35–37, 63]. Amongst these factors are size and dimension of the contaminant [64]. Preliminary investigations indicate that in spite of multi-stage producer gas cleaning procedures the highly volatile constitutions of tar remain in the producer gas, condense and/or deposit on the HV insulator surface and thereby compromising its dielectric characteristic [4, 63, 65, 66]. It is reported

that mostly the light hydrocarbons of the tar species with a molecular mass equal or less than that of the naphthalene are influenced by an ESP only in a small degree [4, 17]. These light hydrocarbon compounds are condensable in nature, capable of forming a layer of semi-liquid deposition on the surface of the HV insulator and thereby lowering its dielectric condition [63]. The electrical discharges that arise as a result of the tar deposition on the surface of HV insulator further degrade the dielectric condition of the HV insulator, thereby compromising the operating condition of the ESP and aggravating aging phenomena [63].

2.3.3 Tar Sampling and Tar Analysis Methods

Appropriate sampling and analysis methods for producer gas that take also the compounds present in the gaseous phase into account are liquid sampling methods according to CEN/TS 15439 [22] as well as a combination of online GC/MS [17]. A further applied sampling procedure is the Solid Phase Adsorption (SPA) method [67] which is insufficient with regard to gaseous compounds like benzene, toluene and o-xylene, since they partly pass through the adsorbent of the SPA, causing deviations of around 10 % for toluene and o-xylene and more than 21 % for benzene [68]. The impact of the different definitions of tar that are available onto the tar removal efficiency of an ESP unit compared for two different sampling methods, is reported in [4]. If the applied definition of tar is according to CEN/TS 15439, which defines that all hydrocarbons with a molecular mass equal or less than that of benzene are not to be considered as constituent of tar, the ESP tar removal efficiency is around 63 % related to liquid sampling (offline) and around 53 % related to GC/MS sampling (online). In case that the useful by-products present in producer gas are not considered as constituents of tar related to the recommendation of *Lin et. al*, the ESP tar removal efficiency increases to 98 % related to liquid sampling and to 99 % related to GC/MS respectively.

Furthermore, it has been reported in literature that hydrocarbon and hetero-cyclic compounds in its gaseous state of aggregation can be decomposed into smaller gaseous molecules in pulsed corona, dielectric barrier discharge and gliding arc discharge applications [69–76]. Since the average of the specific energy density of industrial ESP units is in general equal to or less than 10 J/sdm³, it becomes clear that the decomposition of hydrocarbon and hetero-cyclic compounds into smaller gaseous molecules can be neglected. Nevertheless, the decomposition of gaseous compounds into smaller species would worsen the tar removal efficiency of an ESP unit, since smaller molecules are exhibiting in general higher vapor pressures, thus their amounts in the gaseous phase that can not be affected by the ESP unit would increase and further the efficiency would decrease.

2.3.4 Online Tar Measurement

Figure 2.4 shows the constituents of producer gas before (Figure 2.4 (a)) and after (Figure 2.4 (b)) the gas cleaning process by a wet ESP unit. These data are an outcome of online tar monitoring of producer gas at the inlet (raw gas) and outlet (clean gas) of the ESP unit, performed through the combination of a VARIAN 3900 GC, equipped with a VF-5MS column with a length of 30 m and a SATURN 2100 MS.

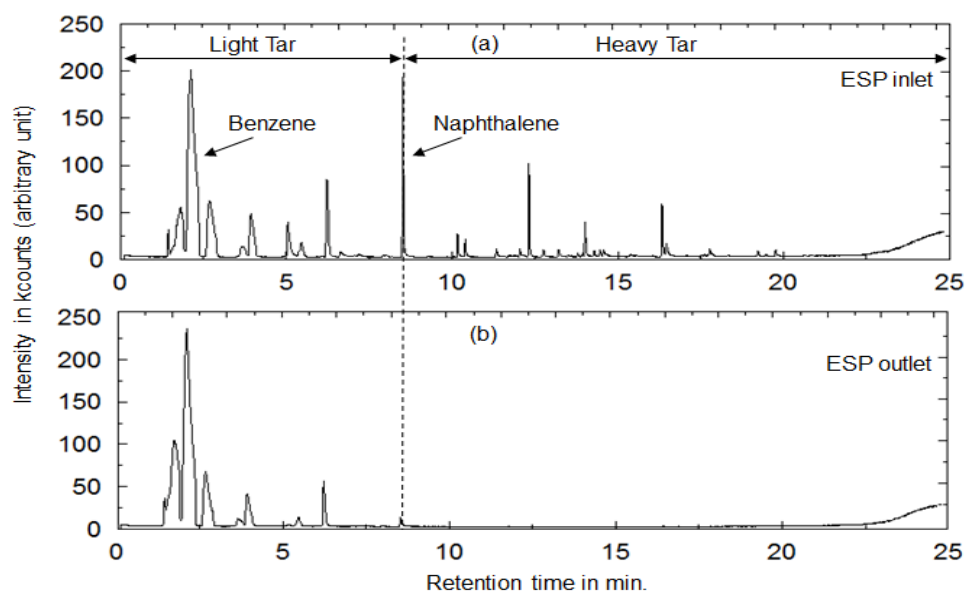


FIGURE 2.4: Reconstructed GC/MS ion chromatogram from an online tar analysis of biomass gasifier producer gas. (a): Raw gas sampled at the ESP inlet. (b): Clean gas sampled at the ESP outlet.

It arises from Figure 2.4 that in particular the mono-aromatic hydrocarbon compounds with a molecular weight below that of naphthalene (128.19 g/mol), which can be defined as light tar (refer section 2.2.1), pass the electric field nearly unaffected [4, 17]. These gaseous, condensable hydrocarbons, along with non-removed aerosols, deposit on the exposed surface of collecting electrodes and discharge electrodes, ceramic insulators, discharge electrode suspension and so on [17, 77]. Amongst all, the ceramic insulator is partly exposed to the condensable hydrocarbon compounds which passed the electric field of the ESP. The contamination deposited on the surface of collecting and discharge electrodes do not pose a threat to the normal operation of an ESP unit since clogging of the electric field is prevented due to deposition layer drain off under ambient condition by the force of gravity. Furthermore, the tar deposition layer compromises the surface resistance of the ESP collecting electrodes only by a minor degree.

2.4 The Course of Tar Deposition on an ESP High Voltage Insulator

The factors that influence the process of tar deposition on the HV insulator surface of a wet ESP unit are explained through a simple flow diagram (Figure 2.5). In a broader sense, these factors can be classified based on operation and design criteria.

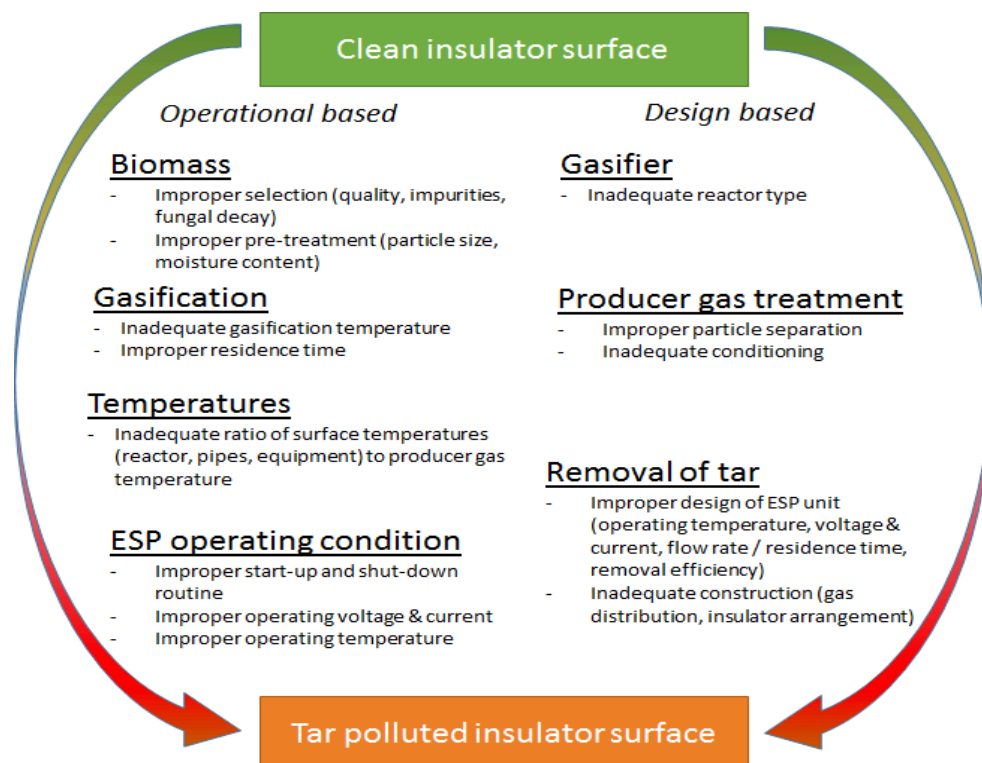


FIGURE 2.5: Overview of operational and design based influencing factors from producer gas cleaning causing insulator surface pollution.

It appears from Figure 2.5 that the factors and respective parameters individually and/or collectively contribute to the extent of the severity of HV insulator surface pollution. So, it becomes clear that through proper planning and appropriate selection of the design-based parameters the extent of insulator surface pollution can be controlled to a certain degree. At the same time, the severity of surface pollution is also affected by several operationally-based parameters, such as operating status, the mode of operation of the gasifier and the downstream devices.

The degree of severity of surface pollution based on the mode of operation of an ESP unit can be divided in three general operational conditions:

- Start-up and shut-off routine
- Normal operation and
- ESP fault condition.

In this regard, it has to be taken into account that the operation of the ESP unit is restricted with respect to the oxygen content present in producer gas since an O_2 concentration of more than 3 vol. % can create an explosive atmosphere. It becomes clear that any discharge in the ESP unit could ignite the producer gas, thus causing an explosion. In order to avoid the operation of the ESP unit under these conditions, a control unit automatically switches on and/or off the ESP unit by means of online monitoring the O_2 concentration of the producer gas.

The surface deposition arising over the period of start-up and shut-off routines highly depends on the applied routine, either by flushing with inert gas or by a bypass operation. A start-up period with inert gas flushing of ESP unit provides the advantage that the ESP unit is set in operation before the gasification reaction is started and producer gas is generated. This sequence of operation ensures that the producer gas is efficiently cleaned in the electric field of the ESP unit, thus only small amounts of tar present in the cleaned producer gas reach the insulator chamber and can condense on the exposed surfaces. Contrary, the flushing of the ESP with inert gas is a cost-intensive procedure that is in most cases not applied in industrial applications. A more common way is the use of bypass flow during the start-up routine. In this procedure the producer gas flows through a bypass until the gasifier has reached stable operating condition. Once this is reached the bypass is closed and the producer gas purges the ESP unit until its operating condition ($O_2 \leq 2$ vol.-%) is reached. In this period of purging the raw producer gas flows uncleaned through the ESP unit, thus high amounts of light tar together with heavy tar compounds reach the insulator chamber that could result in severe surface pollution. During this start-up routine, the level of surface deposition is much higher compared to inert flushing. Under normal operating conditions of the ESP unit, the aerosols of tar are efficiently removed from the producer gas, thus only small amounts of condensable species can reach and deposit on the HV insulator surface in its insulator chamber.

During normal operation of the ESP unit, initial contamination on the surface of the insulator that are accumulated during the start-up period mildly compromise its dielectric integrity. Repeated operation of an ESP unit with an even slightly contaminated insulator increases the level of surface contamination. In the course of time, the operating voltage of the ESP is drastically reduced and electrical discharges emerge on the contaminated surface of the insulator, which

further degrade the ESP operating condition [63]. Early identification of contamination on the surface of the insulator might provide an opportunity to prevent the occurrence of a premature failure. The insulator surface could be cleaned through manual intervention and the operating condition of the ESP unit could be restored. Nevertheless, if unnoticed, the depositions on the surface of the insulator would get glazed causing aging, permanent degradation and premature failure.

The worst case scenario causing high level of HV insulator surface deposition in short term is a malfunction of the ESP unit during operating condition. Since a failure of the ESP unit power supply is one possibility but of rare occurrence, the main reasons for an ESP fault condition are an electric short-circuit in consequence of a broken discharge electrode or an automatic shut-off of the ESP unit HV supply in consequence of an entry of oxygen. Under this operating condition when producer gas flows through the ESP unit while the electric field is not energized, light tar together with heavy tar compounds having dew point temperatures above 350 °C will inevitably condense on all exposed surfaces.

By means of external heating devices like electric trace heating elements applied for insulator surface heating, condensation of water and light tar can be prohibited. Since the electrical properties of the insulation material like electric strength and relative permittivity worsen with increasing temperature, it becomes clear that the degree of heating up is limited. Since it is proven that some heavy poly- and hetero-cyclic tar compounds exhibit dew points well above 350 °C it becomes clear that the condensation of tar species on the insulator surface under any operating condition would require an average surface temperature of around 400 °C.

2.4.1 Measures to prevent surface contamination

Since electrostatic precipitation is used for cleaning of product gas, it has been found that the integrity of the HV insulator surface has a major relevance for ensuring a constant performance. Several measures were developed in order to prevent the deposition of solid particles and liquid aerosols on the surface of the insulator which is installed in the insulator chamber. The common mechanical arrangements of insulator chambers, their purging based on the respective types of HV insulators (support insulator or feed-through bushing) are reported in [78]. In general, the applied measures can be subdivided in mechanical measures and process measures.

2.4.1.1 Mechanical Measures

An early applied mechanical measure was the installation of the HV insulator in a gas-tight insulator chamber or under an insulator hood that is separating the insulator body from the direct gas flow, to limit the deposition of solid particles on its surface [79]. Following this approach, the junction of electrostatic precipitator vessel and insulator chamber were optimized and equipped with nozzle-shaped baffle plates or bus rings [78] for further reduction of solid particle deposition on the insulator surface [80]. In addition, several peaks are placed on the discharge electrode suspension so that the electric wind that arises from these discharges provides a counter pressure to the gas flow, to avoid its inflow from the vessel into the insulator chamber.

2.4.1.2 Process Measures

It has been found that all mechanical measures are not sufficient to avoid insulator degradation in consequence of surface deposition. In short or medium term the surface of the HV insulator gets polluted. By means of further methods like purging or applying trace heating devices the process of surface deposition can be restricted to a minimum value [64, 81, 82].

Materials and Measurement Techniques

3.1 Test Objects

The experimental research on the objectives is carried out by using test samples taken from an actual HV feed-through type ceramic insulator and later on a test insulator. The chosen test samples, being fragments of actual bushings, and test insulators are designed according to the standard BS2562. They are made of silicious porcelain material (type C110 according to IEC 672-3) [83]. The dimension of the bushing (CB3M) is given in Appendix B and the respective basic material properties are tabulated in [83]. A brief overview of the chosen test objects and their respective surface condition is given in Table 3.1. The respective measurement techniques exercised to resolve the objectives of this thesis are provided in Table 3.2.

3.1.1 Test Samples

The test samples A and B are parts of two actual HV insulators. Test sample A is taken from a virgin bushing with a clean and dry surface condition. The data obtained from the sample A are marked as "Clean, dry" and used as reference. Test sample B was part of a contaminated HV insulator. This insulator was installed in an ESP unit and was exposed to producer gas of a fluidized bed gasifier. During service time, this insulator accumulated several layers of tar compounds on its surface. Subsequently, the data obtained from the sample B are marked as "TAR,

dry". Figure 3.1 shows a photo of the test sample B. It can be observed from the Figure 3.1 that the lower part of the insulator surface, which was directly exposed to the producer gas for less than 100 hours of discontinuous operation of the gasification plant, has accumulated severe surface deposition. Also, it can be observed that the deposition is not uniform due to frequent interruption and variation in the level of mild contaminants in the producer gas. Several areas show dark black, dry and glazed surface depositions where surface tracking (electrical treeing) can be observed. These areas exhibit comparably low surface conductivity. On the other hand, there are a few of the black areas covered with powdery carbon black or graphite-like deposition, exhibiting high surface conductivity. Since the producer gas is free from solid particles, it is assumed that the powdery surface deposition has emerged in consequence of localized surface treeing on the deposition layer of tar.



FIGURE 3.1: Photo of the test sample B that was part of an actual HV insulator with severe surface deposition of tar.

The surface of the chosen HV insulator is covered with a mild conducting glazed layer causing a certain amount of surface leakage current [84]. The main reason for such a level of surface conductivity is to warm up the insulator surface, preventing condensation of fog or moisture from the environment and to dry the wet insulator surface. In the present context, the surface deposited compounds of tar will subsequently evaporate and the insulator surface will dry to a certain degree. Nevertheless, certain compounds of tar exhibiting low vapor pressure will inevitably remain on the polluted insulator surface, thereby forming dark black, dry and glazed surface depositions. Since the surface leakage currents don't provide the thermal energy that it required to carbonize this surface deposition, the only

possibility for the carbonization are surface discharges. These discharge events can be categorized as PD phenomena.

3.1.2 Electrode Arrangement

An electrode arrangement is used for facilitating experiments with the chosen test samples. Figure 3.2 shows a three-dimensional sketch of the corresponding electrode arrangement. The samples are placed rigidly between the test electrodes in such a way that there is a good electric contact. The test electrode arrangement is prepared as recommended by standard IEC 60112 [85].

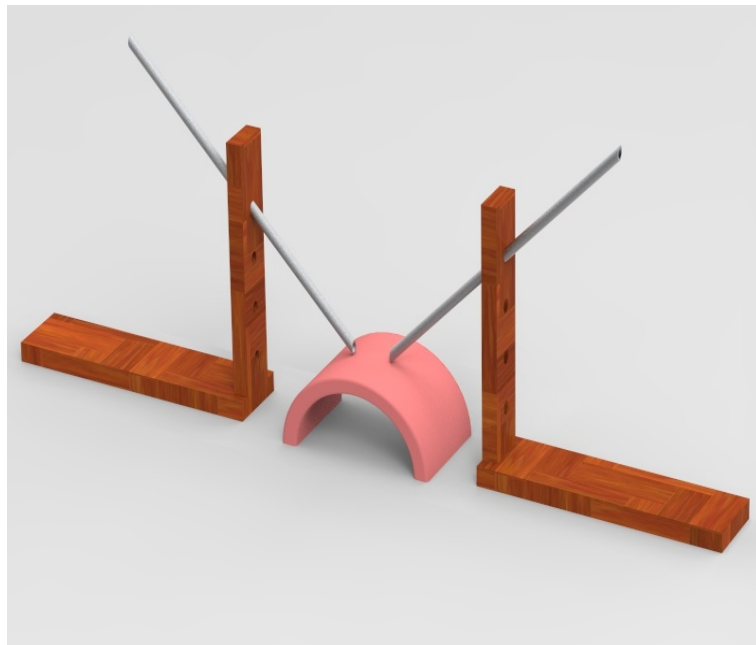


FIGURE 3.2: Three-dimensional sketch of the test electrode arrangement for measuring the dielectric response on the surface of the test samples.

The electrode arrangement consists of a base, two arms and two electrodes. The electrodes are made of stainless steel and the support unit (base and arms) is made of hard paper that exhibits excellent dielectric properties [86]. The broken insulator sample is placed on the base of the electrode arrangement while the electrodes are inserted into the arms appropriately. The two arms are designed with three angular provisions for holding the electrodes firmly towards the sample to provide a flat and punctual contact of the electrode top on the test sample surface, following the standard *IEC 60112* [85]. The electrode geometry recommended by [85] is slightly adapted to satisfy the given geometry of the test sample surface. The three provisions for holding the electrodes are designed in a way to form an angle of 30° ,

45°, and 60° to the base plate respectively. The present study employs angular provision of 45° and 2.5 cm of spacing with symmetrically arranged electrodes. This angle and spacing provides the electrodes with a good, firm and punctual contact (without space or gap between electrode and surface) on the surface of the contaminated sample. Prior to the experiments, it is ensured that the electrode support does not influence the sensitivity and accuracy of the measurements (i.e. the occurrence of PD due to plane surface contact). Once all the precautionary measures are ensured, dielectric experiments are exercised on the test samples A and B and the respective data are measured and analyzed.

3.1.3 Test Insulator

The test insulators involved in the present experimental study are investigated under laboratory conditions. The chosen test insulators are installed in a test rig (refer to section 4.3) and a laboratory-scaled ESP unit (refer to Chapter 5), respectively. A photo of the chosen test insulator is shown in Figure 3.3 and its respective dimension is shown in Appendix B.



FIGURE 3.3: Photo of the test insulator porcelain no. CB3M.

At first, the test insulator A with a clean and dry surface (condition A.1) is installed in a test rig and the reference data are measured. Later, the clean surface of the test insulator is covered by drops of water (condition A.2) and experiments are repeated. Finally, the surface of the test insulator is manually coated with a thin layer of tar (condition A.3) and the same experiments are repeated. The test insulator B is

installed in an actual wet ESP unit and subjected to online and offline diagnostic test methods and monitoring techniques. The slower degradation of the material and subsequent deviations in their respective dielectric properties are sequentially measured. The corresponding surface condition of the test insulator A (A.1, A.2 and A.3), investigated in a test rig under laboratory, and the test insulator B (B.1, B.2, B.3 and B.4), which undergoes an actual degradation during its service time in wet type ESP unit, are tabulated in Table [3.1](#).

TABLE 3.1: Overview of test objects applied in the present thesis.

Notation of test object	Explanation	Surface condition of test object	Test condition	Chapter
Test samples taken from two actual insulator				
Test sample A	Test sample taken from a virgin insulator	Clean, dry	Laboratory	4
Test sample B	Test sample taken from an actual insulator installed in the ESP unit	Severe pollution of tar from producer gas	Laboratory	4
Test insulator installed in the bushing test rig				
Test insulator A	HV insulator (type BS2562 C110)	A.1: clean, dry A.2: clean, wet (drops of water) A.3: tar covered, wet with unknown amounts of water	Test rig	4
Test insulator installed in an actual ESP unit				
Test insulator B	HV insulator (type BS2562 C110)	B.1: clean, dry B.2: tar-covered, wet with unknown amounts of water B.3: Condition from B.2 heated and dried for 4 hrs. B.4: Condition of B.3 heated and dried for 6 hrs.	ESP unit	5

TABLE 3.2: Overview of measurements taken from the respective test objects.

Test object	Index	Dielectric response		Partial discharge			
		Time domain	Frequency domain	AC	+ DC ⁽¹⁾	- DC ⁽¹⁾	UHF
Test sample	A	✓	✓	✓	✓	✓	✓
	B	✓	✓	✓	✓	✓	✓
Test insulator	A.1	✓	✓	✓	-	-	-
	A.2	✓	✓	-	-	-	-
	A.3	✓	✓	✓	-	-	-
Test insulator	B.1	✓	✓	-	-	-	✓
	B.2	✓	✓	-	-	✓	-
	B.3	✓	✓	-	-	✓	-
	B.4	✓	✓	-	-	✓	-

⁽¹⁾: QPRPD pattern

3.2 Techniques for Dielectric Condition Measurement and PD Monitoring

The condition of a HV apparatus, rotating machine and electrical equipment can be effectively determined by employing dielectric response and partial discharge test methods. Both methods combined define the current dielectric status of the chosen HV apparatus. During dielectric condition assessment, it is usual to exercise time domain as well as frequency domain measurement techniques over a wide span of time and frequency. The time domain methods require a longer span to initiate long range ion movements and/or allow sufficient time in order to detect the slow polarization phenomena of the dielectric material. The frequency counterpart of time domain method achieves this by employing frequencies in a sub-harmonic level such as in mHz and μ Hz appropriately. Later, the corresponding DC and AC insulation response of the chosen test object is measured and its characteristic properties are studied. In this context, the partial discharges are considered as not only indicative but also as causes of degradation. Although being a transient phenomenon (PD pulses in ns), the pulses can be significantly influenced by the chosen HV apparatus and the test object itself. The current practice is to employ conventional and non-conventional PD methods, the former being a wide-band detection (in range of kHz), while the later are in Very High Frequency (VHF) and UHF ranges. Nevertheless, the respective data collected from all the diagnostic measurements altogether qualify the dielectric condition of the chosen test object.

3.2.1 Dielectric Response Analysis

3.2.1.1 Time Dependent Dielectric Response

Time dependent dielectric response measurements imply measuring the DC insulation resistance over a longer period (in general 600 s.). In this regard, a device that directly measures HV DC insulation resistance which is popularly known as Megger (MIT 1020/2) is adopted. The device is shown in Figure 3.4. The corresponding schematic for measuring the dielectric response of the test samples, test bushings and test insulator is shown in Figure 4.1 (a) and Figure 5.7 (a) respectively. The MIT 1020/2 consists of an in-built HV DC source capable of supplying up to 10 kV DC test voltage, an adequate measuring unit up to 35 T Ω and well-designed excitation and measuring cables. The Megger device is commonly used during the dielectric condition assessment of cables, HV bushings, power transformers, etc.

The DC insulation resistance is an integral value comprising Leakage Current (I_L), Charging Current (I_C) and Absorption Current (I_A). The leakage current is in general time independent, of smaller magnitude, and flowing from the HV conductor to ground. It appears dominant in the DC insulation resistance value under the condition that the time dependent polarization current and charging current tend towards zero after a short measuring time and also through the degree of surface pollution. The charging current is dominant at the beginning of the measurement when the test voltage is applied to the test object and decreases towards zero when the geometric capacitance is charged. The charging current may be larger than the leakage current at the starting point of the measurement. Charging current decreases after short time of applied test voltage when the capacitance of the insulation is comparably low. In case of a high capacitive insulation the charging current can be dominant for a longer period, until the test object is fully charged. The absorption current results in consequence of polarization mechanisms that occurs in the bulk of the dielectric material and on the surface of the insulator.



FIGURE 3.4: Photo of the Megger MIT 1020/2 DC insulation resistance tester.

First, the Megger is set to Insulation Resistance (I_R) mode for measuring the DC insulation resistance of the individual test objects. The test signal of 5 kV magnitude is injected in one electrode through the positive terminal, while the response is measured from the other electrode through the negative terminal for a duration of 10 minutes. The current flow on the test sample surface is measured, the respective resistance is calculated in the Megger device and the results are transferred to the computer for further analysis.

3.2.1.2 Frequency Dependent Dielectric Response

The frequency dependent response of dielectric properties is analyzed with a Dielectric Response Analyzer (DIRANA) device from OMICRON electronics GmbH. It measures the dielectric response, namely the dissipation factor, AC impedance and capacitance of insulation systems. It is furthermore capable to determine the moisture content in oil-paper insulation of power transformers, oil-paper insulated cables, bushings and instrument transformers. This method employs a three-terminal measurement that includes the output voltage, the measurement current and a guard to prevent disturbances due to current paths caused by polluted bushings or electromagnetic fields. Figure 3.5 shows a photo of the DIRANA device. The corresponding schematic for measuring the frequency response of the test samples, test bushings and test insulator is shown in Figure 4.1 (b) and Figure 5.7 (b) respectively. The DIRANA has an inherent HV AC source that provides a test voltage of up to 200 V with a frequency range from 0.05 mHz to 5 kHz.



FIGURE 3.5: Photo of the Dirana (dielectric response analyzer).

The Frequency Domain Spectroscopy (FDS) method injects a spectral pure sinusoidal AC test voltage into the respective test object in discrete frequency steps through their terminal. The pertaining response of the test object is measured from the terminal from which the macroscopical dielectric properties such as capacitance, loss factor, etc. are calculated. This is achieved by considering the complete dielectric system as a simple RC equivalent circuit arrangement of a resistance and a capacitance, either in series or in parallel. Based on the selected measurement configuration, such as type of test object, wiring diagram and so

on, the DIRANA device fits the current measured with respect to the injected voltage in discrete frequency steps to an in-built model of the type of test object and thereby determines the dielectric properties of the test object. The principle of the DIRANA unit is based on an in-built capacitor that manifests an ideal dielectric behavior, i.e. the respective current (i_C) is displaced $+90^\circ$ to the applied test voltage. Thus, the loss angle (δ) is determined by a comparison of the phase displacement of the current measured from the test object with that of the in-built ideal capacitance.

A simple equivalent circuit that explains the electrical analogy of the dielectric behavior of insulating materials is shown in Figure 3.6 (a) (redrawn from [87]). The parallel circuit of resistance and capacitance represents the phenomenological dielectric behavior of the chosen insulator. The current vector \underline{I}_R (refer to Figure 3.6 (c)) in phase with the applied voltage \underline{U} (refer to Figure 3.6 (b)) represents the amount of dielectric loss current that dissipates in form of heat into the dielectric material, while the current vector with a phase displacement of $+90^\circ$ represents the charging current \underline{I}_C .

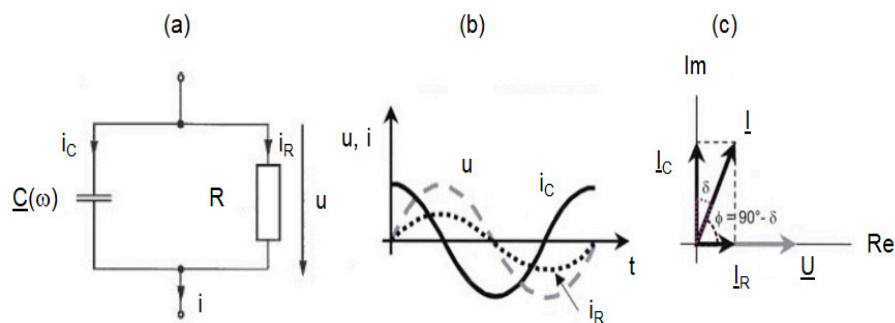


FIGURE 3.6: RC parallel circuit of the dielectric loss factor ($\tan(\delta)$). (a): Equivalent circuit diagram. (b): Voltage and current curve. (c): Vector diagram in the complex plain.

The loss factor $\tan(\delta)$ is defined as the ratio of power loss to capacitive reactive power and can be expressed, depending on the respective frequency value, by

$$\mathbf{\tan} \delta(\omega) = \frac{\underline{I}_R}{\underline{I}_C} \quad (3.1)$$

Based on the equivalent circuit (refer to Figure 3.6) the $\tan(\delta)$ can to be considered as an accumulated quantity that consists of the losses due to conductivity (represented by the ideal resistor R) and polarization (represented by an ideal capacitor

$C(\omega)$) that can be expressed by

$$\mathbf{tan}(\delta) = \tan(\delta_C) + \tan(\delta_P) \quad (3.2)$$

The dielectric loss in consequence of conductivity (σ) can be expressed by

$$\mathbf{tan}(\delta_C) = \frac{\sigma}{\omega \varepsilon'_r(\omega) C_0} \quad (3.3)$$

The possible frequency dependent polarization mechanisms and the amount of dielectric loss of a material in consequence of induced polarization are represented, based on the complex dielectric relative permittivity by

$$\mathbf{tan}(\delta_P) = \frac{\varepsilon''_r(\omega)}{\varepsilon'_r(\omega)} \quad (3.4)$$

where $\varepsilon''_r(\omega)$ represents the amount of dielectric loss in consequence of polarization mechanisms, while $\varepsilon'_r(\omega)$ represents the amount of the reversible storage of charges of the dielectric material.

Considering that only pure DC conductivity is present in a dielectric material, that does not contribute to the charging current, it can be concluded that the loss factor is dominated by the finite value of the residual DC conductivity ($\sigma_0 = \text{const.}$) of the material in absence of polarization mechanisms ($\varepsilon''_r(\omega) = 0$, $\varepsilon'_r(\omega) = \varepsilon_{rs} = \text{constant}$) [88–90]. Thus, the loss factor exhibits a behavior indirectly proportional to the frequency that can be expressed by

$$\mathbf{tan} \delta(\omega) \sim (1/\omega^{-x}) \text{ or } \sim \omega^x \quad (3.5)$$

with a slope of $x = -1$ (or -20 dB).

This approach is commonly applied to power transformer. It is reported, that the loss factor of a power transformer in the lower frequency range (0.1 - 100 Hz), where the electric field can be assumed as quasi-static, is dominated by the finite value of the residual ionic alternating current conductivity of the dielectric liquid in consequence of the migration of mobile charge carriers such as ions [88, 91]. This implies a rise of the imaginary part of the relative complex permittivity at very low frequencies with a slope of -1.0, while the real part of the complex relative permittivity has reached the value of the static relative permittivity that gives a straight line of slope 0 (refer to Figure 3.7) [89].

Since the dielectric loss that is determined by the DIRANA device is an additive value, where the amount of dielectric loss in consequence of polarization mechanism is superimposed by the finite value of the residual conductivity (σ_0), it becomes clear that the measured complex relative permittivity has to be expressed by

$$\varepsilon_{\mathbf{r},\mathbf{DRA}}''(\omega) = \varepsilon''(\omega) + \frac{\sigma_0}{\varepsilon_0\omega} \quad (3.6)$$

and

$$\varepsilon_{\mathbf{r},\mathbf{DRA}}'(\omega) = \varepsilon_r'(\omega) \quad (3.7)$$

so that

$$\underline{\varepsilon}_{\mathbf{r}}(\omega) = \varepsilon_r'(\omega) - i\varepsilon''(\omega) + \frac{\sigma_0}{\varepsilon_0\omega} \quad (3.8)$$

as reported by [89, 92].

Following this, the measured loss factor can be expressed by

$$\mathbf{tan} \delta(\omega) = \frac{\varepsilon''(\omega) + \frac{\sigma_0}{\varepsilon_0\omega}}{\varepsilon_r'(\omega)} \quad (3.9)$$

Furthermore, it is reported that the Debye relaxation law, which explains excellent the frequency response of non-interacting polar dielectric gases and some liquids with a single relaxation time, is insufficient in describing the experimental results of the condensed state of matter where the so-called *many-body universal model for dielectric relaxation* has to taken into account for a sufficient interpretation of the Low frequency dispersion (LFD) and High frequency (HF) power law regimes [89, 90]. The frequency dependent dielectric response of such dielectric materials can be further separated into two or more regimes following individual fractional power laws with characteristic values of the exponents (m and n , below and above the peak frequency (ω_p)) for the real and imaginary part of the complex relative permittivity [89, 93].

$$\sim \omega^{-1+n} \quad (3.10)$$

The reason for the LFD phenomena, which can to be considered as an integral response of several superimposed dielectric relaxation phenomena, that can be addressed to slowly moving charge carriers such as ions, the occurrence of interfacial

polarization phenomena (at material interfaces such as electrode-sample contacts or surface pollution layers, space charge polarization in the bulk and/or at the grain-boundary of the dielectric material, electrode polarization due to ion conduction) or by hopping of electrons [89, 94, 95]. The latter is addressed as the major reason of electronic conduction of organic material [93, 96]. It is reported that a slope between - 0.2 to - 0.4 ($0.6 \leq n \leq 0.8$) is an indication for alternating current conductivity by hopping electrons, while a slope between - 0.5 to - 1.0 can be addressed to the presence of slowly moving charge carriers [97–99]. Furthermore, it is reported that under certain condition the rising slope of $\varepsilon_r''(\omega)$ towards - 1.0 can be attributed to the increase of humidity content [97]. Nevertheless, it has to be taken into account that the experimental data ($\varepsilon_r''(\omega)$ and $\varepsilon_r'(\omega)$) are of macroscopic information since the dielectric response at low frequency values is an integral response of several possible superimposed microscopic polarization mechanisms [100, 101].

Figure 3.7 (redrawn from [87]) shows the frequency-dependent resonance and relaxation behavior that can occur in a dielectric material in consequence of polarization mechanisms, viz. electron polarization, ionic polarization, orientation polarization, space charge polarization and interfacial polarization. Interfacial polarization can occur in the presence of unbounded charges that accumulate under the force of the applied electric field at the grain boundaries and inter-phase boundaries (macroscopically) and/or at the juncture of clustered compounds and/or particles in inhomogeneous mixtures with different conductivities (microscopically), while space charge polarization occurs in the bulk material of the insulation due to the presence of bounded charges. At the same time, molecules with permanent dipole moment manifest orientation polarization, while ionic polarization occurs in consequence of the deflection of cations and anions in molecules with hetero-polar bond structure when a dipole moment is induced in the same due to the applied external field. Since in covalent-bonded compounds free electrons that are able to move are absent, the bounded electrons will interact due to electronic polarization with the applied electric field. In this context it should be noted that in dielectric materials of covalent bonding a small amount of charges is able to move for a certain distance inside the bulk of the material. Thus, in a dielectric material there is also a certain value of dielectric loss in consequence of conduction.

However, it becomes clear from Figure 3.7 that the imaginary part ($\varepsilon_r''(\omega)$) of the relative permittivity exhibits several peaks with increasing magnitude, while the frequency decreases. $\varepsilon_r''(\omega)$ indicates the amount of loss current of the dielectric material (as a result of loss either due to conductivity or polarization). Thus, also the loss factor ($\tan(\delta)$) shows its maximum values in the same ranges of frequency [102].

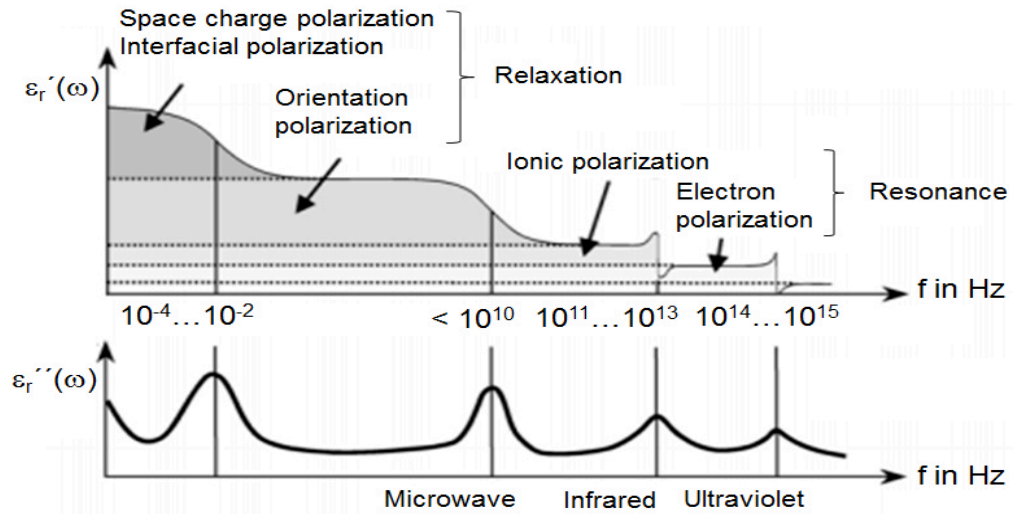


FIGURE 3.7: Frequency dependent resonance and relaxation behavior of a dielectric material. Top: Real part $\epsilon_r'(\omega)$ (dispersion spectrum). Bottom: Imaginary part $\epsilon_r''(\omega)$ (loss spectrum).

Furthermore, it can be observed from Figure 3.7 that a di-polar response involved in the relaxation process will result in a rise of the real part of the relative permittivity up to a certain value, while the imaginary part will show a maximum and further decreasing values with decreasing frequency values. On the other hand, a pure DC conductivity will result in a rise of $\epsilon_r''(\omega)$ to lower frequency values, while the real part ($\epsilon_r'(\omega)$) exhibits a frequency independent behavior. A clear distinction of the nature of the LFD phenomena is quite difficult since the reason of a rise of $\epsilon_r'(\omega)$ to lower frequencies, that was in the past addressed to interfacial processes (so-called *Maxwell-Wagner* effect), can be caused by ionic charge carriers or hopping electrons [93].

3.2.2 Partial Discharge Analysis

The PD-detection-based pollution level assessment has been already investigated [103]. It has been attempted to correlate the PD activity with the type of pollution. These investigations mainly aim at quantifying the pollution level based on Phase Resolved Partial Discharge (PRPD) pattern, PD level and so on [104]. Recent investigations on condition assessment of online PD detection have been based on usage of a Radio Frequency (RF) antenna [103–106]. In addition to this, UHF-based PD investigations are also exercised to ascertain the dielectric quality of the ceramic insulators [107]. Recent assessment shows the influence of polarity and

magnitude of test voltages on the PD occurrence on a HV insulator surface. Furthermore, the electrical discharges on the surface of the ceramic insulator appear stronger under negative DC voltages [108].

Multiple stress mechanisms emerge behind a PD activity in the insulation system of a HV apparatus. In the present context, in addition to electrical stress, that is provoked by electrical discharges arising on the surface of the insulation, leads the resulting thermal stress of the low temperature plasma further into mechanical stress. Subsequent mechanisms purely depend on the type of fault and its location, which are unique and distinguishable. So, it is natural to expect employing conventional and non-conventional PD detection and analysis methods that might widen the potential of understanding the deduced mechanisms. The currently practiced electrical methods on PD detection involve two approaches viz., measurement of the individual discharge pulse and the pertaining total and integrated loss in the insulation system arising due to discharge activity [109, 110]. The first method of PD detection requires a suitable measuring sensor for decoupling PD signals. The pattern manifested by the discharge current is evaluated to identify or discriminate failure conditions [111]. The second method is an alternative for the PD detection which measures the total loss in the insulation system [109, 110]. Recent methods combine pattern analysis along with spectral information of the measured PD signals, which altogether describe the dielectric integrity of the cable insulation [111]. It is believed that such an approach might provide a deep insight in understanding the PD mechanism. This might also help in improving the currently practiced measurement and interpretation strategies popularly adopted during commissioning and acceptance tests.

The electrical discharges that might arise on the surface of a ceramic insulator are extremely fast current pulses of nanosecond rise time and comprise tremendous information. Each current pulse of a PD has a unique rise time and carries a unique amount of charge that can be gathered by measuring indirectly or directly the current pulse in an electrical circuit. Furthermore, each PD event causes in parallel emissions of sound waves and photons, providing an alternative possibility to gather the PD information by acoustic or optical PD measuring procedures. The PD signal processing of modern, digital PD measuring units is shown in Figure 3.8 [112].

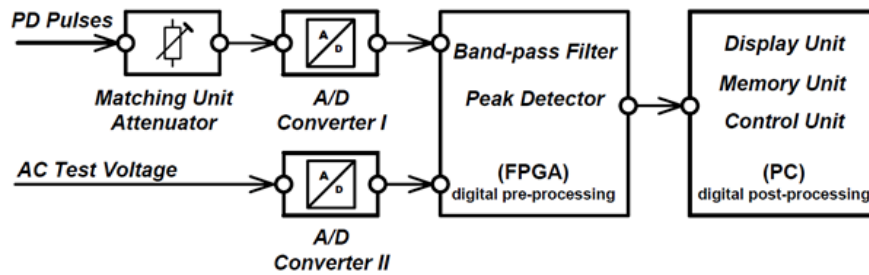


FIGURE 3.8: Block diagram of an advanced digital PD measuring system.

Analogue-digital-converters are available and are capable to perform the digitalization of a PD pulse from a test object in real-time. Band-pass filtering and peak detection are performed in advanced digital PD measuring system in its pre-processing unit. By this way the capabilities of waveform detection and de-noising are improved [112]. A common method is to measure the voltage jump of a measuring impedance that arise in consequence of the current pulse of each PD event. Inductive PD sensor (e.g. High Frequency Current Transformer (HFCT)) or UHF coupler (e.g. LDWS-T) can be applied for capturing these PD pulses. In this context it should to be noted that applying such sensor and coupler is not in consonance with the standard IEC 60270 since the standard defines a measurement circuit where the apparent charge of the PD events is accessed by the amount of charge that is provided by a coupling capacitor in parallel to the test object [113]. The conventional PD analysis methods use a frequency range from 1 kHz up to 1 MHz, modern diagnostic test procedures gather the PD information in a frequency range from 1 MHz up to 10 MHz, while UHF use a frequency range from 100 MHz up to 1 GHz respectively (refer to Figure 3.9 [114]).

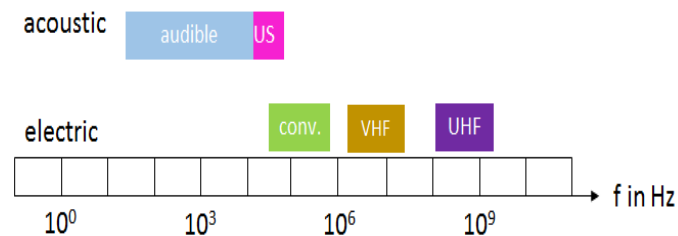


FIGURE 3.9: Frequency band-width of conventional, VHF and UHF PD analysis.

3.2.2.1 Conventional PD Analysis

The MDP 600 device, designed for PD analysis of cables, transformers and rotating machines, is a partial discharge measurement and analysis device from OMICRON electronics GmbH. Figure 3.10 shows a photo of the MPD 600 device connected to a MCU 502 unit and a notebook.



FIGURE 3.10: Photo of the partial discharge measurement and analysis device (MPD 600) and the optic fiber bus controller interface (MCU 502).

The system provides a standard frequency domain bandwidth in discrete steps from 9 kHz up to 1.5 MHz with a center frequency from 0 up to 32 MHz and 200 ns up to 8 μ s time domain, respectively. It is controlled by a MCU 502 optic fiber bus controller interface, providing two optic fiber networks for fiber data transmission between the MPD 600 and further accessories like calibration units, sensors and modern PD measurement devices in acoustic or UHF range. Furthermore, the optic fiber link between the individual devices provides several advantages, e.g. galvanic isolation and lower interference coupling that improves the signal-to-noise ratio. The PD signals detected by a MCT 100 high-frequency current transformer are measured by the MDP 600 unit and further transmitted by the optic fiber link to the MCU 502 unit. The results are visualized by the MPD software either in a PRPD diagram, in 3-Phase Amplitude Relation Diagram (3PARD) or, in case of DC test voltage applied to test object, in a Quasi-Phase Resolved Partial Discharge (QPRPD) diagram respectively. The respective experimental setup for measuring the PD events of the individual test objects under applied AC and DC test voltages are provided in the corresponding subsections in chapter 4 and 5.

3.2.2.2 Non-conventional PD Analysis in UHF Range

The UHF Partial Discharge Measurement (PDM) system from Doble Lemke GmbH is consisting of the ultra-high frequency measuring instrument (LDS-6-UHF) with a frequency range of PD pulse processing unit from 110 MHz up to 1.7 GHz, a pre-amplifier (LDA-5) and the UHF-PD-coupler (LDWS-T PD Sensor) respectively. Figure 3.11 shows a photo of the LDS-6-UHF 3 HE desktop version front panel.



FIGURE 3.11: Photo of the LDS-6-UHF PD measurement system.

The schematic of the LDS-6-UHF device connected to the UHF sensor, Digital Storage Oscilloscope (DSO) and notebook is shown in Figure 5.19 respectively. The LDSW-T sensor is connected to the *PD IN* jack of the processing unit, the DSO is connected to the *CHARGE* jack of the digital control unit to display the signal while the notebook is connected to the *USB* interface on the back panel.

Performing the UHF measurements in a power utility or a substation emerges as complicated since the presence of other equipment will clearly introduce interference. Also, the corona discharges that can appear e.g. at the HV terminals of transformer, at overhead line and/or line insulator will mask the actual UHF signal of a PD event, thereby compromising the sensitivity of the method. Therefore, the detection frequency adopted during the UHF method is initially obtained. This is the frequency in which the other interference remains minimized, if possibly eliminated. The UHF detector is tuned to the detection frequency and the pertinent PD signals radiated from the discharge are measured.

Experiments on Samples

4.1 Procedure

The present study is about the experimental investigations on clean and tar contaminated ceramic insulators used in an actual ESP unit. This includes experiments on insulator surfaces covered with tar from producer gas in dry and wet state. Such an approach becomes necessary to emulate the conditions in an actual ESP unit. Initially, a test sample (test sample B) is taken from a broken ceramic insulator which surface is polluted with tar. Following this, state-of-the-art diagnostic test methods are exercised on the chosen test sample B, in a certain order. First, the dielectric response of the glazed and dry tar on the surface of the test sample B is measured over a wide range of time and frequency. Following this, the electrical discharges that arise on the tar polluted surface of the insulator test sample B are measured through conventional PD test method and PD test in UHF range. During PD measurements, the insulator test sample B is energized with high voltage AC sinusoidal test voltage and the respective PD level is measured. The PD signals are synchronized with the test voltage to obtain their respective PRPD pattern. Later, the measured real time PD signals are de-convoluted in frequency domain and analyzed. For gaining the reference values of the insulator surface a test sample is selected from a test insulator, in the following termed as "test sample A", that provides virgin (clean and dry) surface condition. Once this is completed, the findings of the insulator sample are experimentally verified on an actual feed-through type ceramic test insulator installed in a test rig arrangement.

The subsequent experimental verification involves three ceramic test insulators investigated under laboratory condition in a test rig (refer to section 4.3). Two important aspects are taken into account for designing the test rig in order to

resemble the mechanical arrangement of a HV insulator in an ESP unit. The insulator is placed on a plate while it is fastened by a grounded flange connection. Furthermore, the top HV terminal of insulator is accessible while the lower half of the insulator is sealed gas-tight by the housing of the test rig. Thereby, the test rig resembles the leakage path over the insulator surface of an actual wet ESP unit. The test signals are injected at the top feed-through electrodes while the response is measured from the grounded flange. Following the installation, the baseline data of the test insulators with clean and dry surface condition are measured. Once this is ensured, the insulators are prepared with different surface condition. In order to emulate the actual conditions in an ESP unit, only the bottom part of the ceramic insulator is contaminated. One of the insulators remains with clean and dry surface and is termed as A.1 (clean, dry). The second insulator is prepared with drops of water on its surface and termed test insulator A.2 (water sprayed) while the third which is termed as test insulator A.3 (tar coated) is manually contaminated with tar on its surface. Following the preparation of the surface condition, the dielectric status of the test insulators are determined over a wide span of time and frequency. The findings of the three insulators (A.1, A.2 and A.3) are used for comparing the data measured from clean and contaminated condition of the ceramic test insulator installed in the ESP unit (refer to chapter 5).

During measurements, the test signal is injected through the high voltage terminal/electrode while the response is measured at the grounded flange. Prior to measurements, it is experimentally ensured that the usage of jumpers, connectors and other relevant factors don't influence the sensitivity and accuracy of the data. The optimal operating bandwidth of the setup, electrode arrangement, test object holder, test rig are experimentally identified and carefully considered in order to avoid their influence. Additionally, uniform sets of connecting leads, wires, electrode spacing and other arrangements are applied. Also, the repeatability of each measurement is cross-verified.

4.2 Experiments on Test Samples

Figure 3.1 shows the photo of the contaminated test sample B that is involved in the present study. There are locations on the surface of the tar contaminated sample indicating occurrence of localized electrical discharges (tracking) that have partially bridged the area. These areas indicating the possibility of surface tracking are surrounded by black depositions that exhibit in contrast to the glazed tar deposition high surface conductivity. Since measurements on these areas might

not reveal the actual electrical behavior of the pollution layer, these locations are carefully avoided.

4.2.1 Dielectric Response Analysis

It is widely known that the dielectric spectroscopy, or dielectric response analysis, in the time and frequency domains offers an excellent opportunity for insulation condition assessment of power apparatus and their predictive maintenance [92, 115–119]. Appropriate methods for power transformer, assessment of transformer insulation and transformer oil condition, outdoor insulator and so on and their interaction with the theory of dielectric response are already available. In summary, the dielectric response of insulations can be measured in time and frequency domain and provides information about the current surface condition of the insulation such as pollution level and degree of humidity as well as information about volumetric condition of the insulation material like structural changes due to mechanical, thermal and/or electrical stress. The DC insulation resistance measurements are used to ascertain the condition of the insulation from the time domain measurements, while the frequency domain dielectric response measurements are derived from the well-known *Tangent Delta* ($\tan(\delta)$) test method. Subsequent test procedures involved measurement of the loss factor or $\tan(\delta)$, complex impedance, capacitance and permittivity over a wide frequency ranging from μHz to kHz. Figure 4.1 (a) and Figure 4.1 (b) show the schematic of the test setup used for measuring the time and frequency dependent dielectric response of the chosen test sample, respectively. The corresponding photography of the setup is shown in Figures 4.2 (a) and 4.2 (b), respectively.

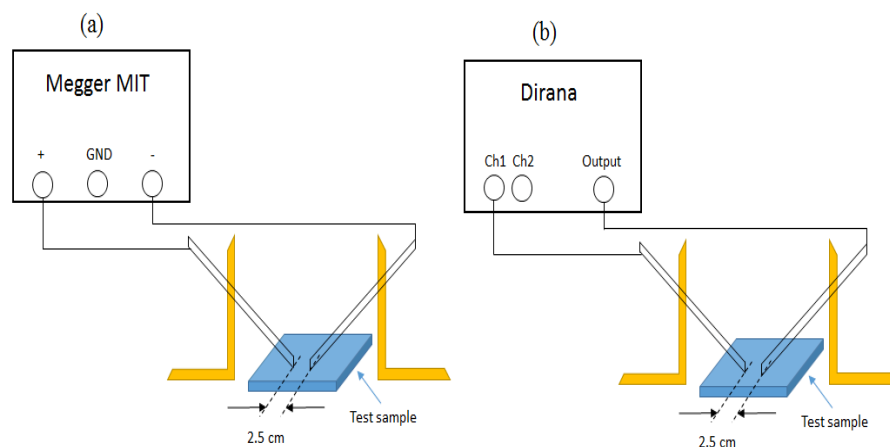


FIGURE 4.1: Schematic of the dielectric response test setup. (a): Time domain.
(b): Frequency domain.

During service of the ESP unit the dielectric condition of the HV ceramic insulator becomes compromised in consequence of surface deposition of tar. Such condition prevails despite the fact that the several constituents of tar exhibit excellent dielectric properties, while only a few of them are polar in nature. Modern dielectric response measurements could provide the ability to reveal the current dielectric condition of the ceramic insulator. Therefore, this thesis adopts time and frequency dependent measurement methods to ascertain the dielectric condition of the ceramic insulators and to understand the collective behavior of tar.



FIGURE 4.2: Photo of the dielectric response test setup. (a): Time domain.
(b): Frequency domain.

For measuring the DC insulation resistance of the test sample surface the applied Megger MIT 1020/2 device is set to I_R mode. The test signal of 5 kV magnitude is injected in one electrode through the positive terminal of the Megger, while the response is measured from the other electrode by the negative terminal of the Megger device for a duration of 10 minutes. The current flow on the test sample surface is measured, the respective resistance is calculated in the Megger device and the results are transferred to the computer for further analysis.

4.2.1.1 Dielectric Response in Time Domain

Figure 4.3 shows the DC resistance of clean and contaminated (dry) surface condition of the ceramic insulator sample. Two observations can be made from this Figure 4.3. First, a clear discrimination between the clean and tar polluted state of the test sample can be made. The relative difference between clean and dry polluted surfaces is comparatively large. This finding points out the possibility of using this method in determining the individual surface condition of the test samples. A second observation is regarding the collective behavior of tar in dry state. Normally, a good insulator would manifest a very low conductivity (high

insulation resistance), while the same under surface polluted condition might result in higher conductivity. Contrary to this, the condition of the insulator sample with dry tar on its surface seems to emerge as better than its clean counterpart. The dry tar polluted surface (Figure 4.3) manifests a high resistance ($\approx 80 \text{ G}\Omega$) and shows an increase of the resistance with respect to the test duration, while the clean state of the insulator surface shows a comparatively slight increase during the measuring period and exhibits a lower value which is close to $10 \text{ G}\Omega$. In other words, the test sample polluted with tar in a dry state of aggregation manifests with lower surface conductivity than its clean counterpart.

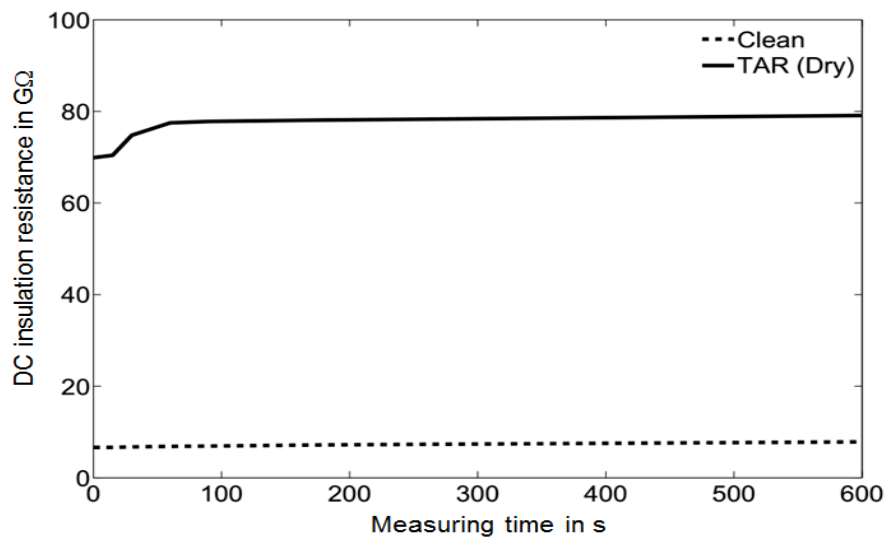


FIGURE 4.3: DC insulation resistance of test sample A and B measured at 5 kV.

The DC insulation resistance of the test sample with clean and dry surface condition remains more or less constant with respect to the measuring time. This indicates that the surface resistivity is dominated by the amount of leakage current, while the impact of charging and absorption current are of short duration. The finding that the DC resistance of the clean and dry test sample surface shows a minor increase with respect to the test duration might be due to the fact that the insulator surface is covered with a glazed layer. It is reported in literature that the surface of outdoor insulators is glazed to provide them a constant value of leakage current to dry the hydrophobic insulator surface in shorter time [84]. Thus, the DC insulation resistance will show a constant value over the test duration which is constant to the finding from the clean test sample. The DC insulation resistance of the tar polluted test sample surface shows a constant value during the first few seconds and further increases within the first 100 s of the test period after which the finite value is reached. This indicates that the resistance value of the dry deposition layer of tar is dominated by the charging current and the absorption current within the first seconds of the measurement duration.

4.2.1.2 Dielectric Response in Frequency Domain

The setup used for measuring the dielectric response of the test samples A and B over a wide frequency range and the corresponding schematic are shown in Figure 4.2 (b) and Figure 4.1 (b), respectively. For measuring the frequency dependent dielectric response the type of test object of the measurement configuration tab of the DIRANA software is set to General Dielectric. Following this, the maximum output of the sinusoidal test voltage is set to 100 V, start and stop frequencies are set to 1.0 kHz and 0.01 Hz respectively and the type of measurement sequence is set to FDS. Once this is finished, the measurement is started and the measurement duration of the set frequency range in the FDS mode is about 25 min.

Figure 4.4 shows the AC impedance of clean and tar polluted surface condition of the chosen insulator test samples over a wide frequency. Altogether, it is found that the dry pollution layer on the surface of the insulator sample have improved surface DC resistance (refer to Figure 4.3) and AC impedance (refer to Figure 4.4). Such an improvement of the dielectric condition can be attributed to the mono-aromatic hydrocarbon compounds, i.e. benzene, toluene, styrene, xylene and naphthalene (refer to Figure 2.2), which are mainly present in the dry deposition layer of tar. The frequency dependent AC impedance under clean surface condition is close to 10 G Ω at low frequencies (10 mHz) exhibiting a slight decreasing trend to higher frequencies. However, the AC impedance of the tar polluted surface is around 180 G Ω at 10 mHz. Consequently, a clear distinction between the clean and tar polluted conditions of the insulator sample is achievable. At the same time, the AC impedance of clean and contaminated conditions of the insulation seem to exhibit a quasi-matching at frequencies ranging from 1 kHz to 100 Hz.

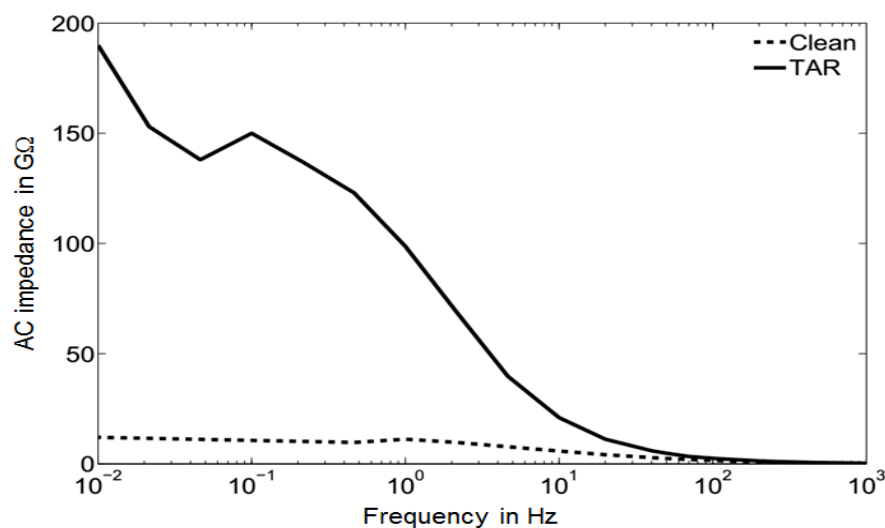


FIGURE 4.4: AC Impedance of test sample A and B measured at 200 V.

In addition to this, another interesting observation can be made from Figure 4.4. The elevation of frequency dependent impedance under tar polluted condition of the ceramic insulator seems to point out the collective dielectric behavior of the several compounds of tar. In other words, the frequency dependent conductivity at low frequencies is very low, while the same increases with increasing frequency values and exhibits a clear peak at around 0.1 Hz. Consequently, it is possible to expect that the loss factor of the tar polluted sample is lower than the clean state of the insulator sample.

Figure 4.5 shows the absolute value of the complex capacitance that is measured from the two test samples. The capacitance of the tar polluted insulator surface is at 10 mHz around 25 pF, while the same for the clean insulator is close to 200 pF. Hence, the permittivity of the tar polluted surface is decreased compared to baseline condition. Furthermore, since the baseline condition exhibits a strong rise of the complex capacitance below 1 Hz it follows that the dielectric material is steadily stressed at low frequencies. However, it can be noted that the dry deposition layer of tar exhibits a significant capacitive behavior at frequencies below 0.05 Hz.

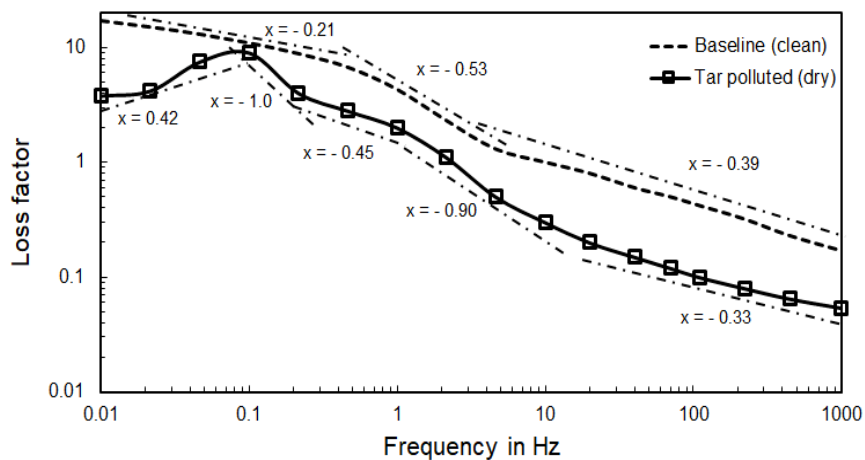


FIGURE 4.5: Loss factor of the clean and tar-coated test samples.

The loss factor of the test samples is shown in Figure 4.6. The first observation that can be made from Figure 4.6 is that both samples exhibit an increasing loss towards low frequency values. Furthermore, the critical frequency of the clean test sample and thereby the maximum value of loss is located somewhere below 0.01 Hz, while the loss factor of the tar polluted surface (test sample B) shows comparatively low values over the frequency range and a clear maximum around 0.1 Hz. Secondly, the tar deposited surface shows an inverse S-shape. A clear difference of the loss factor response between the 2 surface condition can be noted. At frequencies above 20 Hz, the rise of the loss factor matches (slope around

0.3) while below that frequency the slopes show a divergent trend indicating the occurrence of different polarization mechanisms. At 10 mHz, the loss factor of the tar polluted state of the insulator sample is around 4.0 Per Unit (p.u.), while the same for the clean insulator is approximately 18 p.u. respectively. It appears that the frequency response of the clean test sample follows 3 different slope values with a transition at around 5 Hz and 0.4 Hz, respectively.

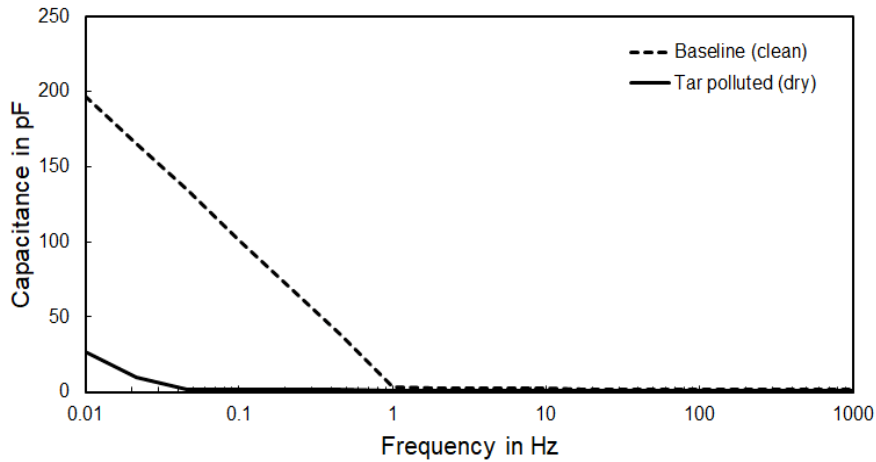


FIGURE 4.6: Complex capacitance of the clean and tar-coated test samples.

The presence of mobile charge carriers like ions, that can migrate under the impact of an applied external electric field, is negligible since the surface of both test samples is of dry state. Thus, it can be concluded from Figure 4.5 that the loss factor increase of test sample A from 1 kHz to 5 Hz is a dominated by electron hopping in consequence of the residual AC conductivity. Below the frequency value of 1 Hz the capacitance increases significantly. It appears that the rising amount of charging current is not capable to compensate the dielectric loss with decreasing frequency values. However, it can be noted that the increasing capacitive behavior towards lower frequency values reduces the rise of the loss factor slope. Nevertheless, the increasing capacitance indicates a dominant lossy polarization mechanism with decreasing frequency values (so-called LFD phenomena). It is expected that this behavior is a result of interfacial polarization mechanisms inside the glazing layer of the insulator, where the capacitive charging and discharging of the interfacial causes loss current producing thermal heat that dissipates into the glazed layer to warm it up. Instead, the slope value of around - 1.0 above 0.1 Hz of the tar deposited test sample can be attributed to residual DC conductivity, while the loss factor below 0.05 Hz is dominated by interfacial polarization.

4.2.2 Partial Discharge Analysis

Electrical discharges inevitably arise on the surface of the tar deposited ceramic insulator. The PD signals are extremely fast current pulses of nanosecond rise time and comprises tremendous information. These information can be unfurled in time and frequency domain. The current trend employs PRPD pattern and 3PARD to understand the characteristic pattern and deduced mechanisms.

4.2.2.1 PD at AC Test Voltage

Employing AC test voltage during PD measurements is widely practiced. The pattern-based analysis has received wide attention and is popularly used to investigate the PD phenomena. The decoupled PD signals are synchronized to the test voltage. Simultaneously, the PD pulse magnitude and the instantaneous values of the test voltage are captured and stored. By synchronizing the sinusoidal test voltage and PD pulses, the unique patterns that are manifested by each type of PD and the pertaining defective conditions can be distinguished and thereby analyzed. In this way, an overview about the dielectric conditions and the possible sources of defects is made available.

4.2.2.1.1 PRPD Pattern

The PRPD technique provides the phase correlation of the determined apparent charges through quasi-integration of the measured PD pulses in relation to the determined amount of charge that is gained from the calibration procedure [88, 120]. The PRPD pattern provides the phase on the horizontal axis (x-axis) that consists of one complete cycle of the applied test voltage while the PD charge magnitude on the vertical axis (y-axis) consists of the apparent charge level magnitude. Therefore, a PRPD pattern shows the occurrence of PD activity at a specific phase related to the applied test voltage, while the apparent charge magnitude is integrated within the numbers of test voltage cycles during the measurement.

4.2.2.1.2 3PARD Diagram

During propagation of electrical discharges, the respective PD signal faces deterioration, damping, attenuation, reflection and also suffers other transmission related problems. Multiple PD events in the same high voltage apparatus tend to overlap on each other masking other PD sources. Additionally, PD pulses can occur from other power units, electrical machines and devices that are inductively and/or capacitively interconnected. Due to their complex propagation and coupling characteristics, every possible PD source has a unique PD-triple magnitude relation

and consequent characteristic signature. In order to visualize the amplitude ratio of PD triple pulses, the so called 3PARD diagram is employed for analysis along with PRPD pattern.

4.2.2.1.3 PD AC Test Setup

A photo of the setup used for measuring the electrical discharges is shown in Figure 4.7 while the corresponding schematic is given in Figure 4.8, respectively. The PD detector is set to a band-width of 160 kHz with 360 kHz as center frequency. An AC test voltage is applied to the surface of the test sample through one electrode, while the other electrode is grounded. The PD signals that arise from the test object are decoupled from the ground connection through an HFCT (split core, 80 kHz to 5 MHz, MCT 100).



FIGURE 4.7: Test setup for measuring the electrical discharges (PD) on the surface of test sample A and B under AC test voltage.

The decoupled PD signals are transmitted to a PD detector (MPD 600) which is popularly used in measuring PD on several high voltage apparatus. The measured data are later replayed with respect to time and the corresponding PRPD pattern and the apparent PD levels are analyzed. Subsequently, the measured PD data are unfurled and the frequency domain information of the PD signals is analyzed.

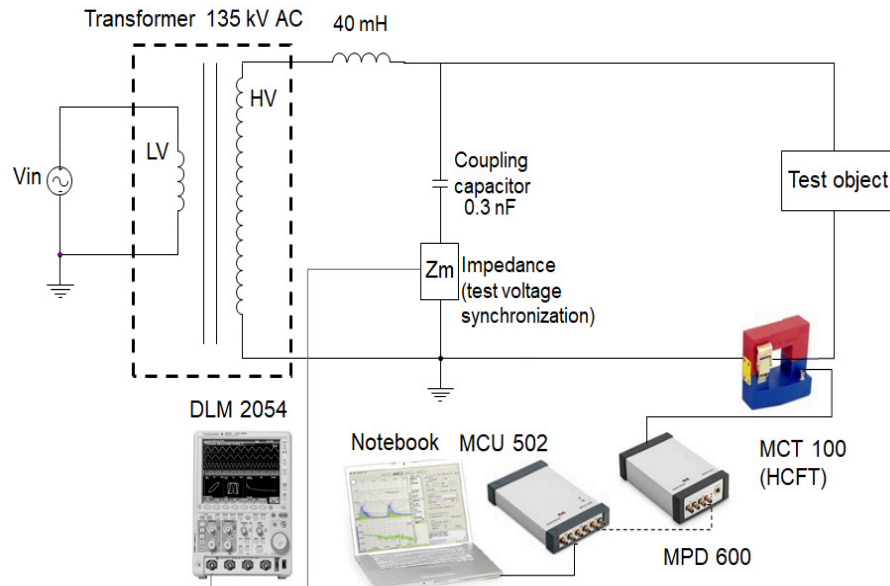


FIGURE 4.8: Schematic of the PD test setup under AC test voltage (shown in Figure 4.7).

4.2.2.1.4 PD AC Calibration

Practically, it is not possible to measure the actual amount of charge of an PD event. Instead, another related electrical quantity termed as Apparent Charge (Q_a) is applied for quantification. The apparent charge is the charge of a pulse which closely resemble an actual PD pulse current. Injecting such a pulse at the terminals of the device under test which is connected to the PD measuring circuit gives the same reading as the actual PD pulse which emerges from the calibration method. The calibration procedure involves a calibrator that injects pulses that closely emulate a PD current in absence of high voltage supply. Figures 4.9 and 4.10 show the setup used for calibration of the PD measuring circuit respectively.

A calibrator unit (LDC-5) that consists of a step voltage generator and a series capacitor, that injects pulses equivalent to a PD signal, is applied for calibration. The pulses are injected at the terminals of the test object to emulate an actual condition faced by the measuring circuit. Following this, the PD detector frequency is suitably adjusted to achieve a better signal-to-noise ratio and the value of the measured pulse magnitude is calibrated to the value of the injected pulse. Following this, the baseline noise (digital) and other possible noise sources that intervene with the PD test circuit are determined. Thereby, it is ensured that the baseline noise lies within the acceptable level of less than 2 pC. In addition to this, it is ensured that additional PD sources, that can possibly interfere with the measurements, are absent.

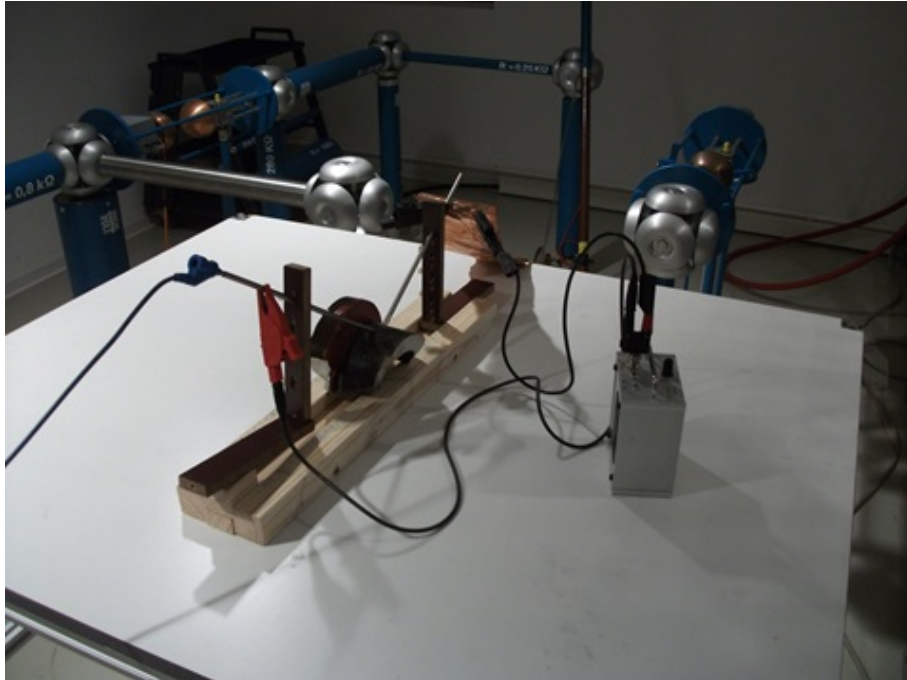


FIGURE 4.9: Calibration setup of the PD AC test circuit.

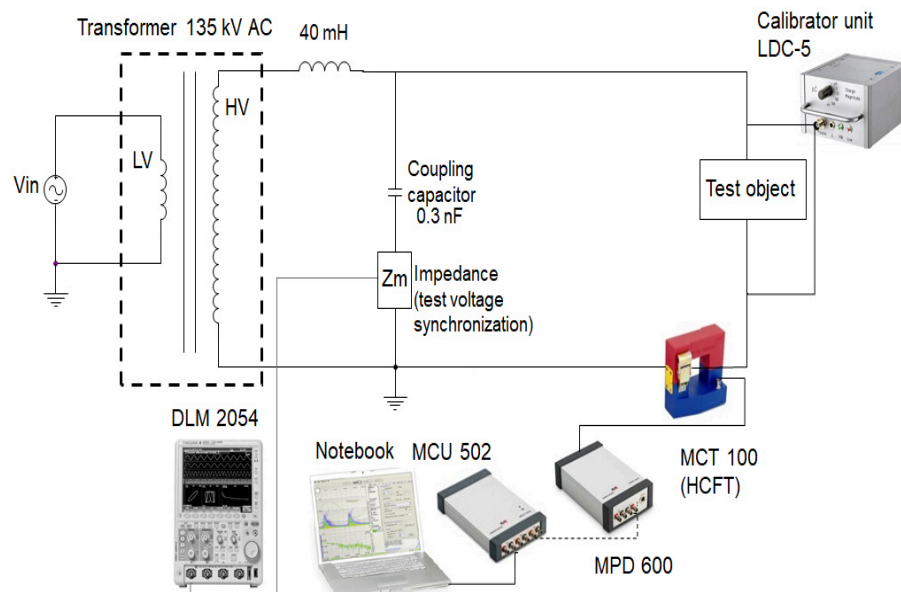


FIGURE 4.10: Schematic of the setup used for calibration of PD AC test circuit (shown in Figure 4.9).

4.2.2.1.5 PD AC Analysis

4.2.2.1.5.1 Pattern Analysis

Figure 4.11 shows the PRPD pattern pertaining the electrical discharges that arise on the surface of the chosen insulator test sample B. It can be observed from Figure 4.11 that the electrical discharges are stable PD pulses that remain correlated to the phase of the sinusoidal test voltage. Such electrical discharges are not observed on the surface of test sample A with clean and dry insulator even at a test voltage up to 5 kV AC. The phase correlation of PD pulses remains close to the first and third quarter cycle. Based on their phase correlation, it can be concluded that the electrical discharges arise on the surface of the tar layer in between the electrode arrangement. It can be found from the pattern that the PD level magnitude of the discharges in the first and third quarter differ by a factor of 3. Since the surface deposition layer of tar can be assumed as dry insulating layer between the two test electrodes this conclusion is in consonance to the findings reported in [44]. Following this, the frequency content of the measured PD signals are de-convoluted in frequency domain and analyzed.

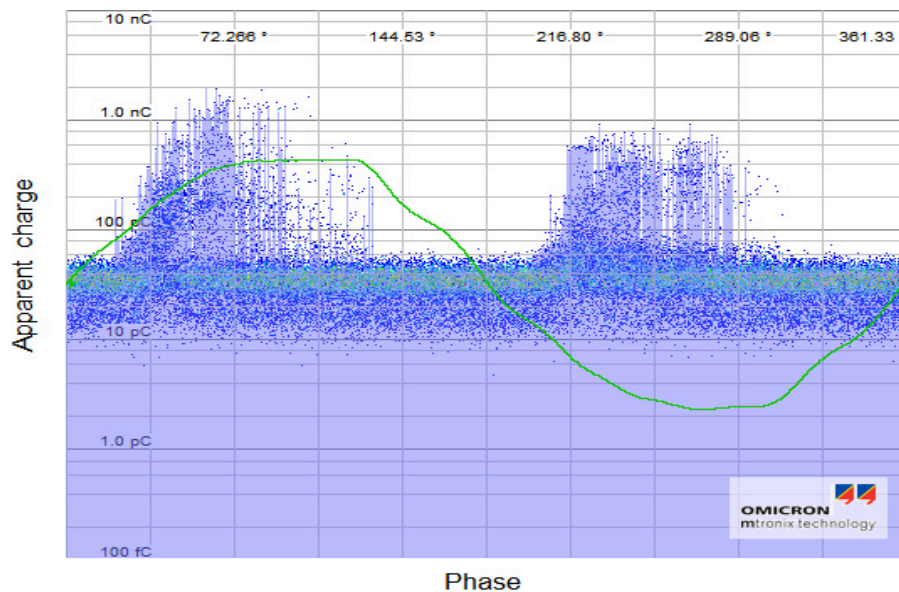


FIGURE 4.11: PRPD pattern of test sample B measured at 4.96 kV (PD level of 594.4 pC).

4.2.2.1.5.2 PD Analysis in Time and Frequency Domain

The raw PD signals are filtered and processed using the blackmann window function in the PD detector. Following this, the filtered signals are unfurled and the

gained frequency domain information is analyzed. Figures 4.12 (a), 4.12 (b) and 4.12 (c) show the real time PD signals measured from the HFCT of baseline, calibration and PD activity, respectively. The Figures 4.12 (d), 4.12 (e) and 4.12 (f) show the frequency content of baseline, with calibration and PD signals shown in Figure 4.12 (a), 4.12 (b) and 4.12 (c), respectively. It becomes clear from the Figures 4.12 (a) and 4.12 (d) that interference due to presence of external PD sources is insignificant since the determined signal intensity of the calibration pulse and the actual PD pulse is much larger. In addition to this, a correlation can be made between the calibration pulse (Figure 4.12 (e)) and actual PD signal (Figure 4.12 (f)) in frequency domain. It appears from the Figures 4.12 (b) and 4.12 (c) that the calibration and PD signal contain more or less the same information below 5 MHz, while the measured calibration signal contains more information in the frequency range above 5 MHz. Furthermore, the calibration pulse manifests a dominant peak in frequency domain around 2 MHz (Figure 4.12 (e)) indicating the frequency span in which an actual PD signals should appear. As expected, the actual PD signal gained from the test sample surface contaminated with a layer for tar in dry state (Figure 4.12 (f)) manifests a dominant peak exactly in the same frequency range.

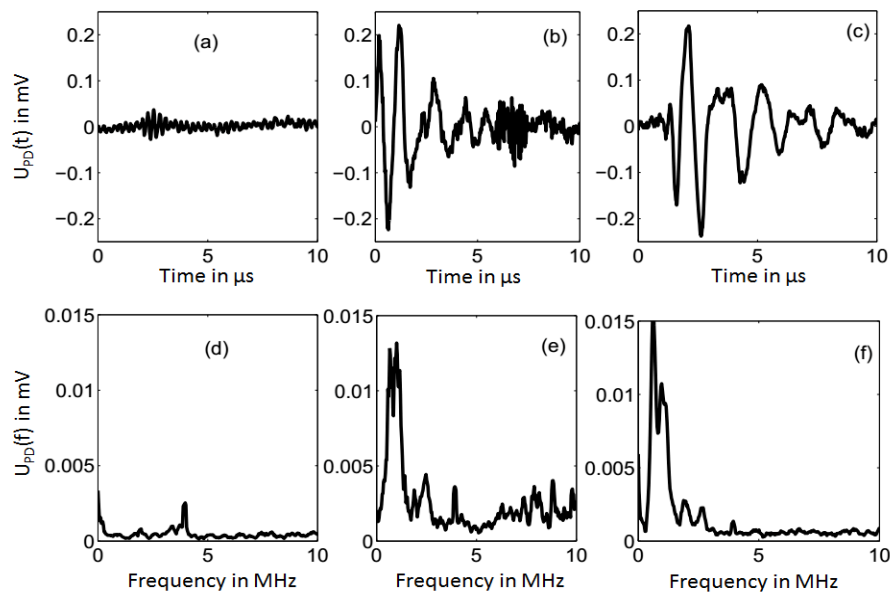


FIGURE 4.12: PD signal waveform in time and frequency domain. (a): Baseline in time domain (test sample A). (b): Calibration pulse in time domain (test sample A). (c): PD signal in time domain (test sample B). (d): Baseline in frequency domain. (e): Calibration pulse in frequency domain. (f): PD signal in frequency domain.

4.2.2.2 PD at DC Test Voltage

The test circuits used during PD measurements under AC and DC test voltage are quite similar while the analysis and interpretation of measured data is different. Since a pure DC test voltage exhibits no dynamic variation of the test signal it is common that the number of PD pulses and their respective magnitude are counted with respect to measuring time.

4.2.2.2.1 PD DC Interpretation

The applied AC based PD signal analysis and interpretation procedures cannot be directly extended to the data measured under DC voltage since the synchronization to the phasing of the applied frequency is not possible. Therefore, the current trend during PD investigations under DC voltage is more or less a quality check procedure [121]. The PD pulses of different magnitude are measured with their appropriate time stamps. Depending on the magnitude of the measured PD pulses related to the value of the applied test voltage, the quality level of the insulation is ensured through a "GO" or "NO-GO" result.

4.2.2.2.2 Quasi-Phase Resolved PD Pattern

The current trend of counting the number of PD events that arise due to DC voltage appears reasonable since there is no dynamic variation in the test voltage. There might be a few PD events which might occur during the transient part of the DC voltage. However, upon steady state, the discharge might stop as long as the DC voltage remains the same, since the charges at the PD site don't recombine or diffuse into the surrounding dielectric medium. So, there is no possibility to perform a pattern analysis similar to that of the AC investigations. However, the adopted high voltage setup employs a half-wave uncontrolled bridge rectifier for converting AC into DC. Although the test voltage applied to the sample is DC, the actual input to the rectifier unit is an AC signal. Ideally, the output voltage of the rectifier unit with capacitive load is DC. However, even a small conduction would result in ripples. Consequently, there are two components, one being DC and another being AC, respectively. So, there is a possibility to correlate and/or synchronize the PD signals to the AC input of the rectifier unit. By this way, the dynamic variations of the PD pulses are still (indirectly) correlated to the AC input of the rectifier unit. At the same time, it is not appropriate to term the corresponding pattern analysis as Phase Resolved PD (PRPD). Hence, the phase resolving of PD signals, in the present context, is technically termed as QPRPD pattern.

4.2.2.2.3 PD DC Test Setup

The test setup used for measuring the electrical discharges under the influence of DC test voltage is shown in Figure 4.13, while the corresponding schematic is shown in Figure 4.14. The adopted PD test circuit comprises a half-wave high voltage arrangement (up to 135 kV DC), a coupling capacitor and a digital PD detector (MPD 600). A HFCT (MCT 100) is applied for the decoupling of the PD signals, while the PD signals are measured in the PD detector.

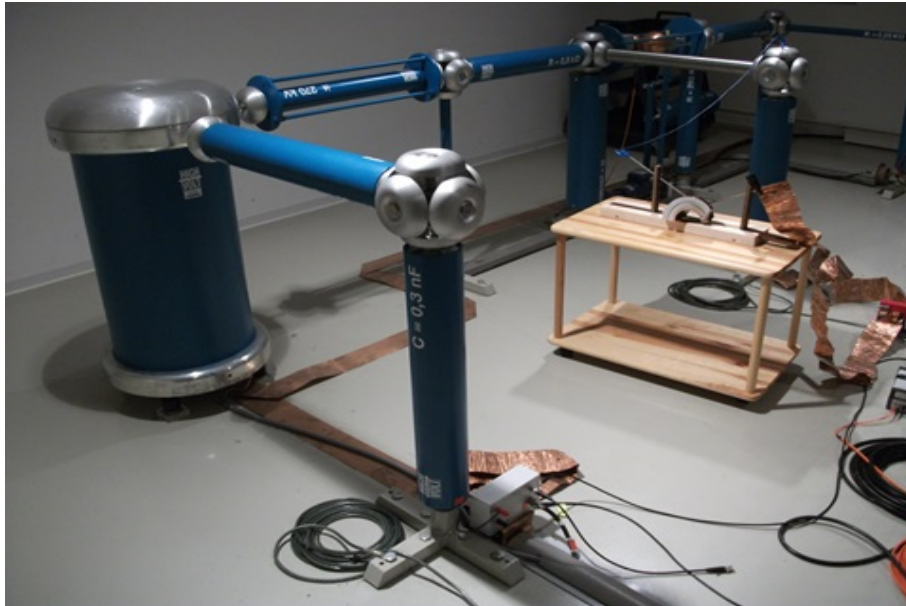


FIGURE 4.13: Photo of the PD DC test setup.

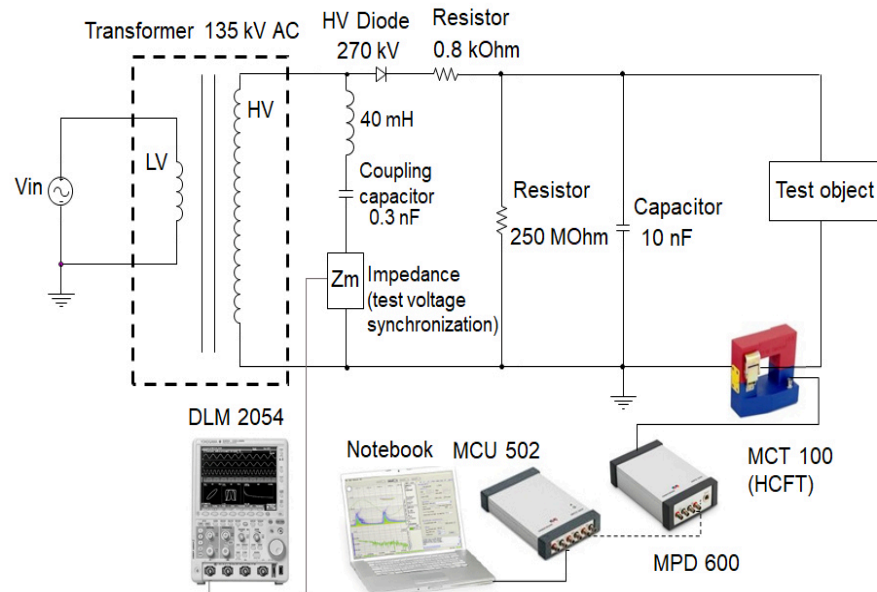


FIGURE 4.14: Schematic of the PD DC test setup (shown in Figure 4.13).

4.2.2.2.4 PD DC Test Voltage

Figure 4.15 exemplifies the wave shape of the rectified test voltage that is applied to the test object during the DC test voltage experiments. It can be observed from Figure 4.15 that a minor ripple exists in the DC test voltage which is predominantly due to the nominal smaller amount of charging and displacement current of the applied capacitor due to the presence of a certain amount of loss current drawn by the complete test setup arrangement.

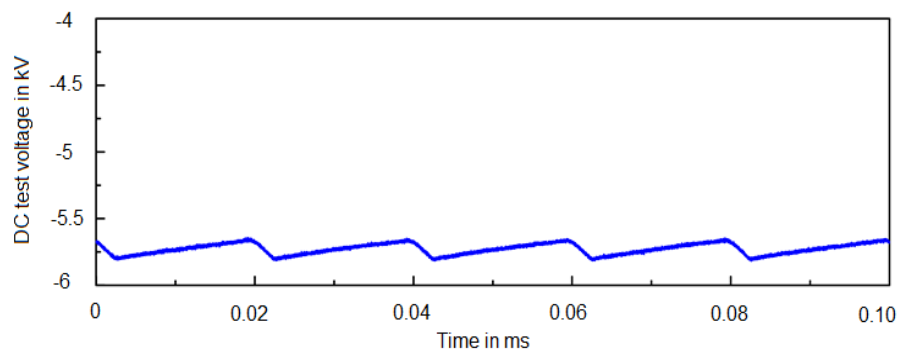


FIGURE 4.15: Wave shape of the DC test voltage.

4.2.2.2.5 PD DC Calibration

Prior to measurements, it is important to calibrate the test circuit to ensure PD detection sensitivity and measurement accuracy. Hence, the PD test circuit adopted

in the present study is calibrated to a known calibration signal. The schematic of the calibration setup is shown in Figure 4.16.

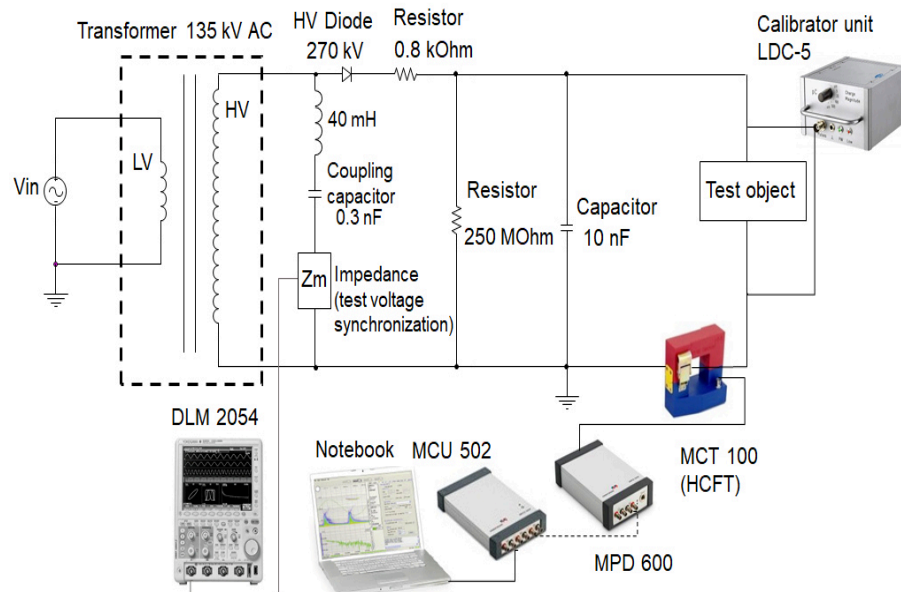


FIGURE 4.16: Schematic of the calibration setup of the PD DC measuring circuit.

Figure 4.17 (a) shows the QPRPD pattern and Figure 4.17 (b) shows the 3PARD diagram of calibration, respectively. The adequacy of such calibration procedure remains well accepted since the respective calibration pulse closely resembles a PD signal. The calibration pulse (of 100 pC) is injected onto the surface of the test sample and the respective charge measured by the PD detector is calibrated to the magnitude of injected pulse. Once calibrated, the baseline data is measured and its respective QPRPD pattern (Figure 4.17 (a)) and 3PARD (Figure 4.17 (b)) is analyzed to ensure that there is no interference coupled to the PD measurement circuit respectively. Additionally, the possible location of a PD signal that can be observed in the 3PARD diagram is also identified. By this way, a clear distinction between noise or interference from PD can be made.

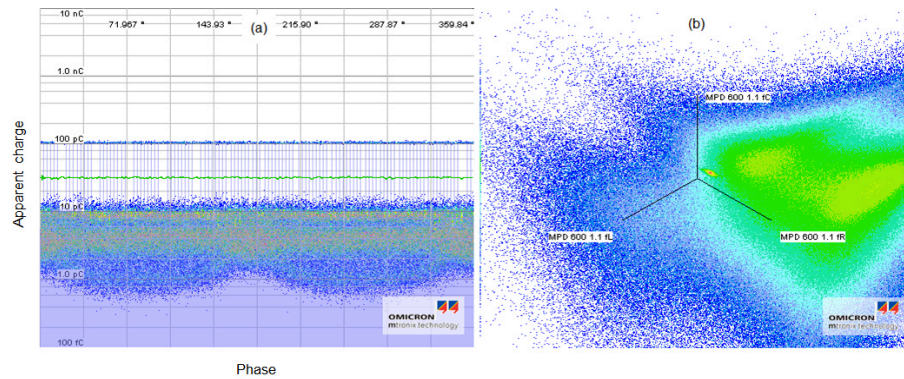


FIGURE 4.17: Calibration pulse of PD DC test circuit on the test sample A. (a): QPRPD pattern. (b): 3PARD diagram.

4.2.2.2.6 PD DC Analysis

4.2.2.2.6.1 PD Analysis at positive DC Test Voltage

Figure 4.18 and Figure 4.19 show the QPRPD pattern pertaining to electrical discharges arising on the surface of the chosen sample under the influence of a positive DC voltage. It becomes clear from Figure 4.18 that the PD pulses are stable, phase correlated and emerge at the positive cycle of AC voltage input to the rectifier unit. Such electrical discharges arise only when the test voltage reaches + 8.1 kV. The number of PD events increase drastically with rising of the test voltage. It can be found from Figure 4.19 that stronger and stable pulses evolve with an increase of the applied test voltage up to + 10.4 kV DC.

The pulses occupy the complete first half of the voltage cycle with more dominance in the rising part of the test voltage, while their apparent charge level of close to 600 pC remain constant upon further increase of the test voltage. In addition to this, there are a few pulses with less PD activity that appear over the full cycle of the synchronization voltage. The apparent charge level of these pulses increase from around 20 pC to close to 40 pC upon further increase of the test voltage.

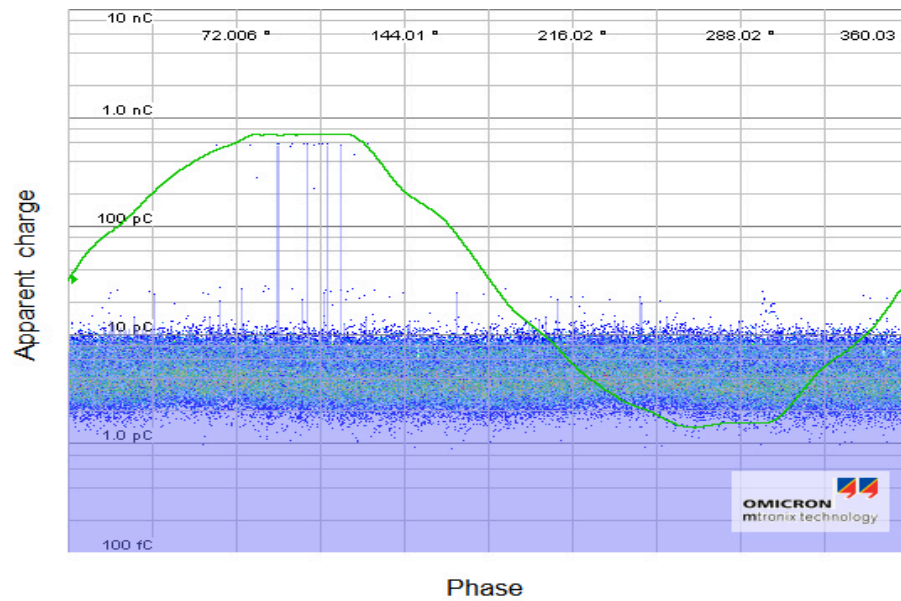


FIGURE 4.18: QPRPD pattern of test sample B under positive DC test voltage measured at + 8.1 kV DC (PD level of 358 pC).

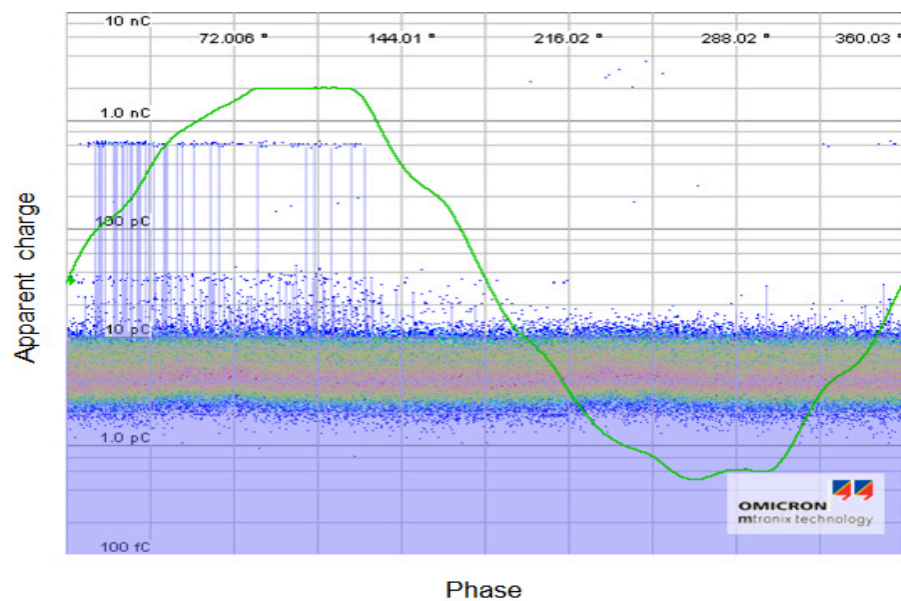


FIGURE 4.19: QPRPD pattern of the electrical discharges on the test sample B at + 10.4 kV DC (PD level of 623 pC).

Since there are two types of PD events (one phase correlated and another one independent) the charge time (q-t) characteristic of electrical discharges are measured. Figure 4.20 shows the charge-time (q-t) characteristics of the electrical discharges which arise in the presence of positive DC test voltage.

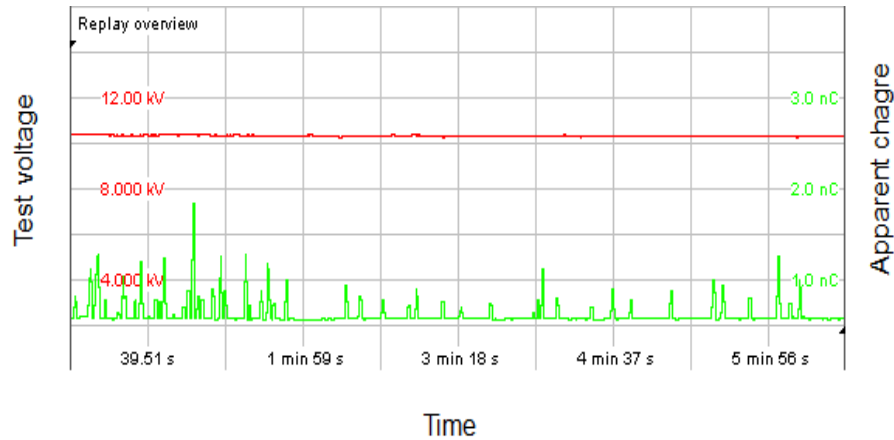


FIGURE 4.20: Charge-time (q-t) characteristics of intermittent electrical discharges on the test sample B measured at + 10.4 kV DC.

Two phenomena can be observed from this Figure. The electrical discharges arise intermittently throughout the measuring time. At the same time, the amount of intermittent PD events reduces with respect to time and the apparent charge level seems to stabilize in the range of 1 nC. The positive polarity of the applied voltage causes a leak of electrons at the positive test electrode, while the formation of positive interfacial charges reduces the magnitude of the resulting field strength around the electrode. This provokes an increase of electric field strength magnitude between the two test electrodes causing its equalization. Thereby, the number of surface discharges with respect to time is comparable low in case of applied positive DC test voltage.

4.2.2.2.6.2 PD Analysis at negative DC Test Voltage

Figures 4.21 and 4.22 show the QPRPD pattern of the electrical discharges arising on the tar polluted test sample surface during negative DC voltage. It can be found from Figure 4.21 that the PD pulses appear in the negative half cycle of the synchronization voltage, while their apparent charge level is within the range from 40 pC up to 80 pC. Also, the surface discharge inception voltage of negative DC test voltage is of smaller magnitude compared to the condition of applied positive DC test voltage (refer to Figure 4.18 and Figure 4.21) since the field strength magnitude around the negative electrode is comparatively higher in case of negative DC test voltage, while the same in case of positive DC test voltage is reduced due to the formation of positive charges in consequence of the leak of electrons that recombine at the positive test electrode. At the same time, the PD charge level is of less magnitude compared to the condition in case of positive DC test voltage.

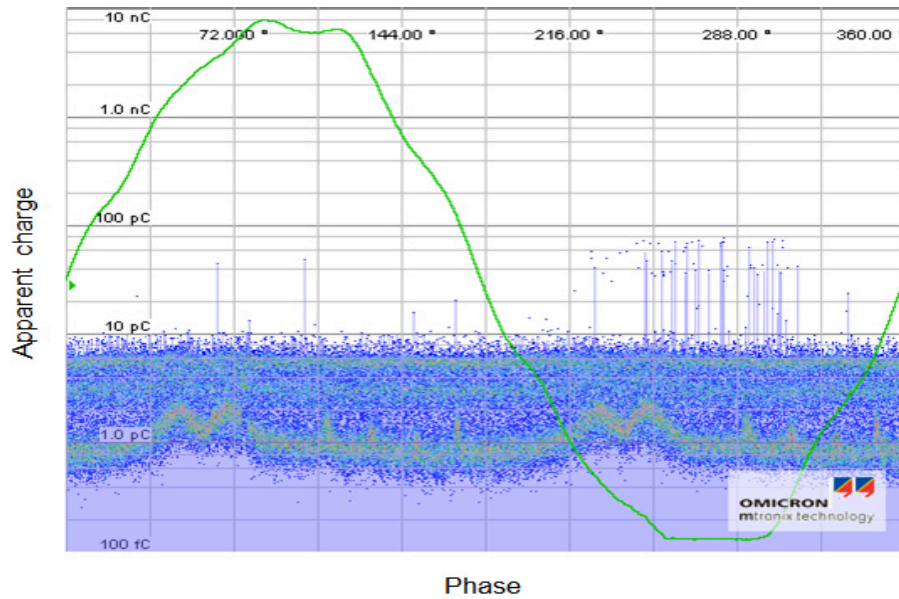


FIGURE 4.21: QPRPD pattern of electrical discharges on the test sample B measured at - 6.9 kV DC (PD level of 46.8 pC).

Figure 4.22 shows the QPRPD pattern pertaining to elevated negative DC voltage conditions. The first observation that can be made from Figure 4.22 is that the number of PD pulses is drastically increased. Also, two different discharge patterns are present exhibiting apparent charge level of 100 pC and close to 150 pC, respectively. The PD pulses emerge over a wider range of the cycle of the synchronization voltage under elevated DC voltage conditions. Furthermore, there are a few PD events that arise over the full synchronization voltage cycle, exhibiting apparent charge level from 40 pC to close to 100 pC.

Figure 4.23 shows the charge-time ($q-t$) characteristics of an electrical discharge arising on the tar deposition during negative DC voltage. As opposed to positive DC voltage conditions (Figure 4.20), the electrical discharges are continuous and not intermittent. Also, the apparent charge level increases with respect to time from 800 pC at the beginning of the measurement to a level of close to 1.2 nC that is reached after 90 s of the measuring period. However, there are some intermediate discharge events in between the first seconds. This might be due to the fact that the initial formation of negative surface charges cause a reduction of the field strength of the negative electrode since the surface charge flow off on the dry tar layer is of smaller magnitude than the velocity of charge injection at the negative test electrode, causing the charge pulses at the start of the measurement. It can be found from Figure 4.23 that amount of surfaces charges around the negative test electrode lowered the local field strength two times drastically (after around 30 s and around 60 s) causing the expiry of that the discharge mechanism. The

constant apparent charge value that is reached after around 90 s indicates that the equilibrium of charge injection and flow off is reached.

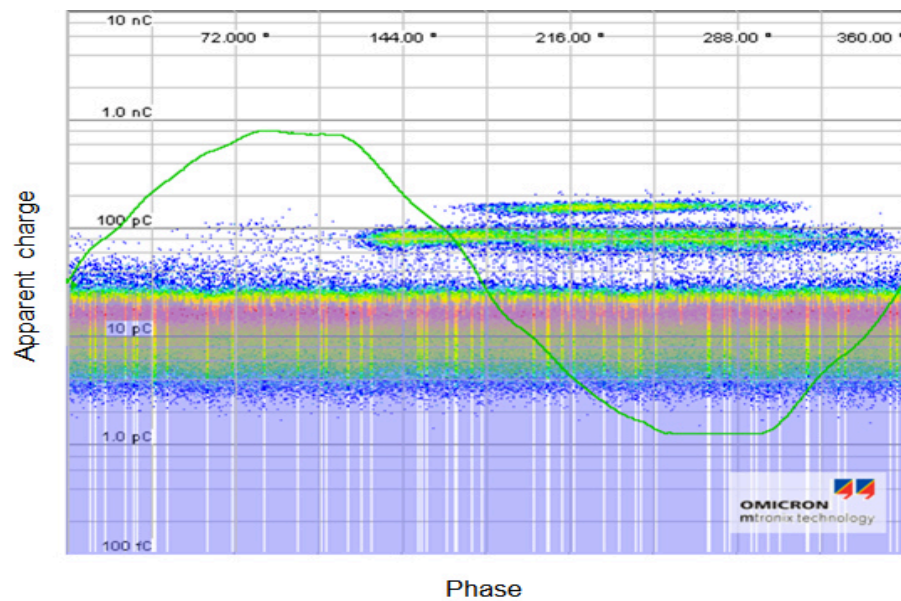


FIGURE 4.22: QPRPD pattern of electrical discharges on the test sample B measured at - 8.1 kV DC (PD level of 144.2 pC).

Figures 4.24 (a) and 4.24 (b) show the 3PARD diagram of Figure 4.18 and Figure 4.21, respectively. It can be found from the Figures 4.24 (a) and 4.24 (b) that irrespective of the polarity of the test voltage, the location of PD pulses remain the same in the 3PARD diagram. Also, there exists a possibility of two PD sites on the insulator test sample. This observation is consonant with the finding from Figure 4.22.

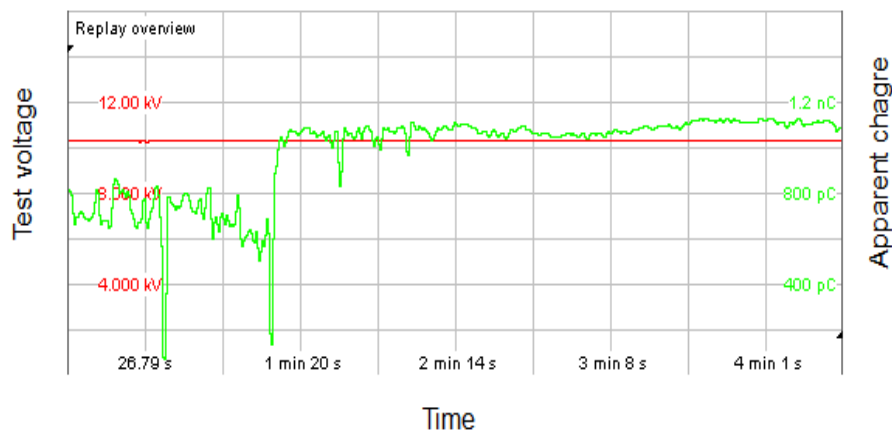


FIGURE 4.23: Charge-time (q-t) characteristics of continuous electrical discharges on the sample B measured at - 10.4 kV DC.

In addition to this, it can be concluded from Figure 4.24 (b) that the electrical stress in consequence of the discharges that arise along with the applied test voltage is comparatively higher at negative polarity. This is consonant to the finding from the Figures 4.20 and 4.23 that the apparent charge level is on the one hand of higher magnitude and reaches a constant value with respect to time, while the apparent charge level at positive polarity of the test voltage shows an intermittent behavior with several peaks of decreasing intensity and declining numbers over the measuring period.

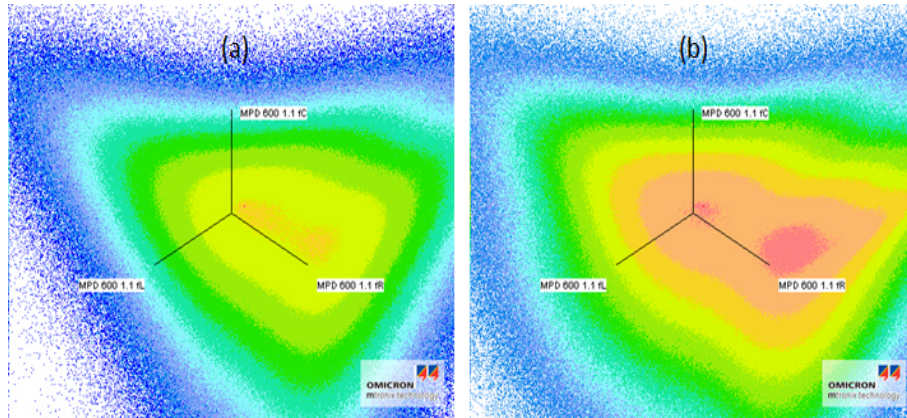


FIGURE 4.24: 3PARD diagram of electrical discharges on the test sample B. (a): Measured at + 8.1 kV DC. (b): Measured at - 6.9 kV DC.

Comparatively, it can be concluded that the stress condition corresponding to the positive and negative polarity are different. The positive polarity comprises momentary charging and subsequent discharge, while the negative test voltage comprises continuous charging and very few discharges. By comparison, it is possible to expect that an insulator under DC test voltage with negative polarity is stressed severely in consequence of the constant charging. This is a common problem in an ESP unit that the negative test voltage charges the insulator.

4.2.3 Non-conventional PD Analysis in UHF Range

Electrical discharges normally manifest as electrical pulses of shorter duration ranging from ns (sometime ps) to μ s. Naturally, the information in frequency domain spans from few kHz to several MHz and sometimes even to GHz. So, it is customary to use sensors of broader bandwidth for the detection of PD signals of short duration. Currently practiced UHF-based PD detection methods measure the radiated electromagnetic signals with frequencies ranging from 100 MHz to 3 GHz. The dominance of signal frequencies purely depends on the type of fault, material, power apparatus etc., while the radiated electromagnetic signals

are detectable using antennae, UHF probes or UHF couplers. The type of sensor, connection method and other relevant procedures are chosen based on the type of apparatus and deduced mechanism. For instance, considering a transformer, the UHF antennae sensors are used at the drain-valve and/or at the top hatch of the grounded tank. The present study uses a high impedance UHF coupler which is popularly used at the indoor/outdoor power cable termination and gas insulated substation [122]. Figure 4.25 shows the frequency response of the applied broadband UHF coupler. It becomes clear from this Figure that the UHF coupler offers high impedance to frequency signals below 100 kHz, while manifesting low impedance for the signals at ultra high frequencies up-to 1.5 GHz. The applied UHF coupler inductively decouples the signals at the ground termination by using a bypass connection at the grounded terminations. The test setup used for measuring the UHF PD signals emerging due to the electrical discharges on the surface of the chosen insulator sample is shown in Figure 4.26. It is more or less similar to the one adopted during AC analysis (refer to subsection 4.2.2.1.3). The only difference is the usage of a measuring sensor (broadband UHF coupler) for decoupling the PD signals in the UHF range from the ground path.

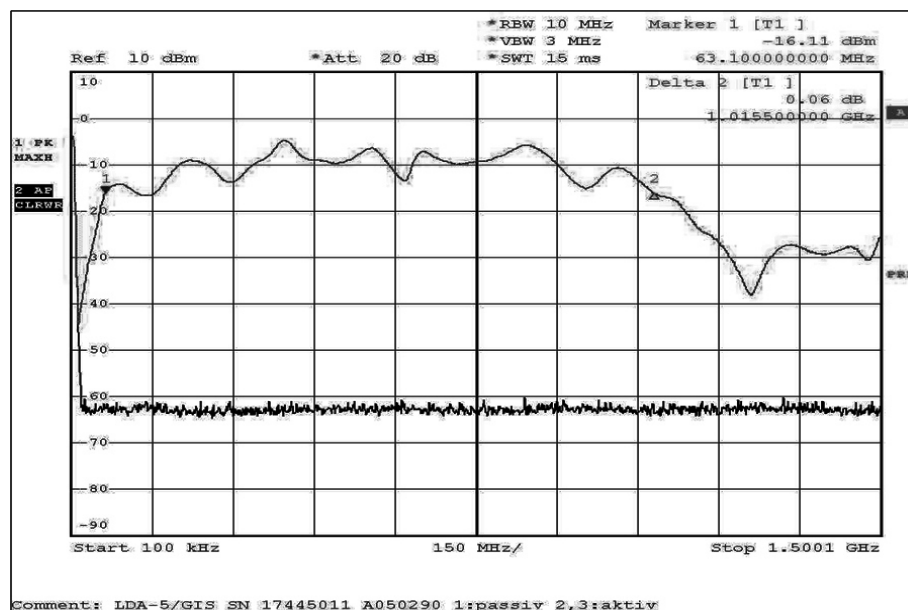


FIGURE 4.25: Frequency response of the broadband UHF coupler LDWS-T (top line).

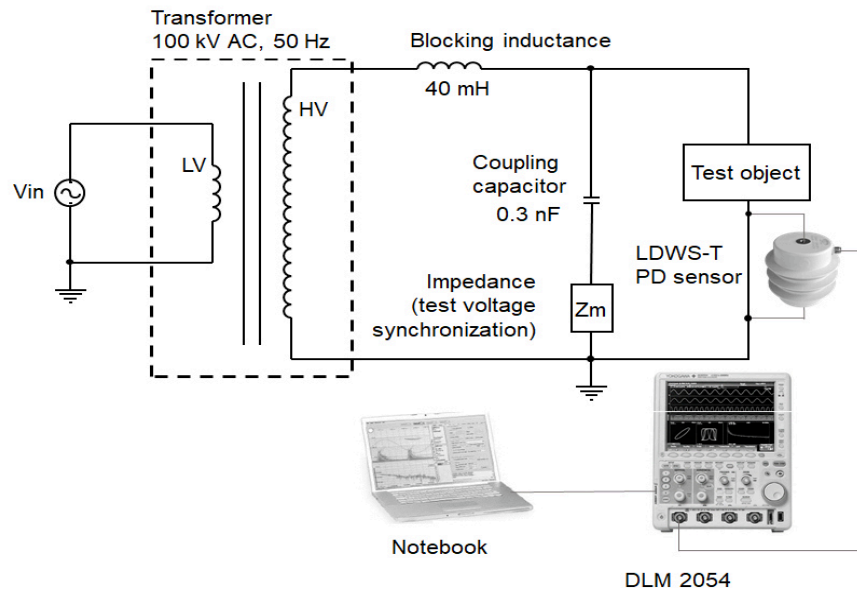


FIGURE 4.26: Schematic of the test setup used for measuring UHF PD signals on the test sample B.

The decoupled signals are measured in a DSO (Yokogawa DLM 2054) and later transferred to a computer and analyzed in time and frequency domain. Prior to experiments, it is a usual procedure to check the performance of the measuring circuit by injecting an UHF pulse. For this purpose, an UHF pulse generator (LDC-7/UHF) was used. The adopted pulse generator produces UHF pulses with magnitudes adjustable from 0.1 V to 60 V, ≤ 200 ns rise time and 500 ns tail time repeated at every 10 ms interval. This pulse generator is used for the verification of the sensitivity of PD measuring circuits operating in the UHF/VHF range. The chosen pulse generator can be operated only in horizontal position since it consists of a relay with mercury covered contacts. Otherwise, the device would generate slow pulses or would get damaged [123]. The pulse generator (LDC-7/UHF) produces pulses that are relatively wide compared to the width of the actual PD signal. Nevertheless, these pulses are sufficient for performing a sensitivity check of the PD measuring circuit. Prior to all, it is experimentally ensured that the test circuit doesn't influence the sensitivity and accuracy of the measurement.

4.2.3.1 Performance Check

Figures 4.27 (a) and 4.27 (b) show the time domain and their corresponding frequency domain representation of UHF pulses generated by the pulse generator, employed for performance check. The rise and tail time and corresponding frequency information becomes clear from the Figures 4.27 (a) and 4.27 (b). Although the

rise time is too short (200 ps), the apparent pulse width is quite broader. Hence, the frequency information is wider until 10 MHz. However, the time and frequency response of an actual PD event would be different. The pulses would be still shorter in its duration and its magnitude, that can be attenuated based on the length of the transmission path.

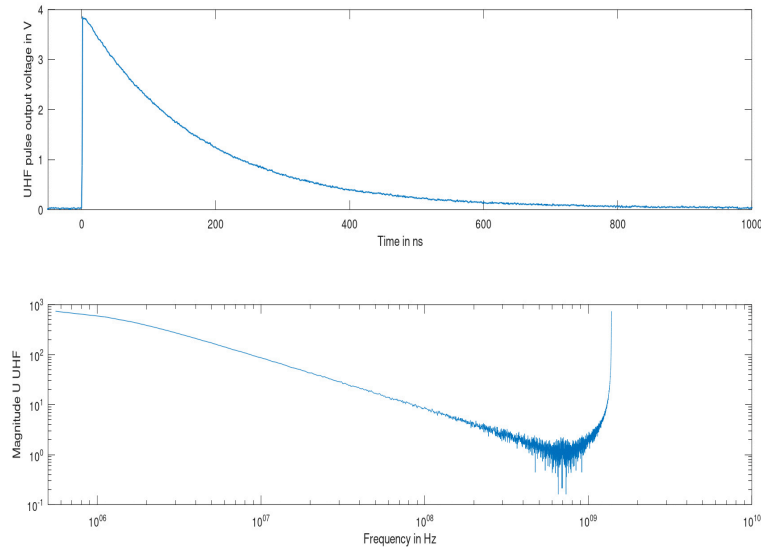


FIGURE 4.27: Time and frequency representation of UHF pulse used for performance check of UHF PD measuring circuit. (a): Time domain. (b): Frequency domain.

4.2.3.2 Signal Analysis in Time and Frequency Domain

Figures 4.28 (a) and 4.28 (b) show the real time representation of UHF PD signals of surface discharges arising on the surface of the insulator test sample. It becomes clear from these figures (Figure 4.28 (a) and Figure 4.28 (b)) that the apparent UHF signals, decoupled through the broadband coupler, are significantly faster than the pulses used for performance check. The rise and tail times are in the range of ‘ns’ as opposed to the UHF pulse used during the performance check. The oscillations are due to the influence of the measuring circuit while the high frequency content might indicate PD activity. Also, the intensity of PD activity is proportional to the elevated test voltage which can be observed as increased peak value of the measured UHF pulses. In other words, the UHF PD pulse magnitude is higher at a test voltage of 5 kV, while the same is reduced for 3 kV. Figures 4.28 (c) and 4.28 (d) show the frequency contents corresponding to the real time representation of the UHF PD signal.

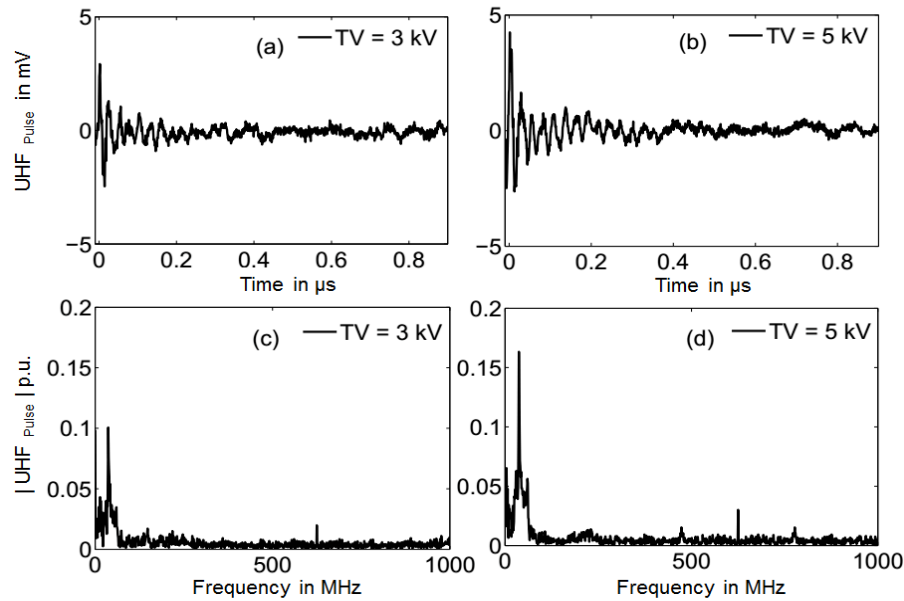


FIGURE 4.28: UHF PD signal pertaining to the electrical discharges arising on the surface of the tar contaminated broken insulator sample. (a) Real time representation at test voltage of 3 kV. (b) Real time representation at test voltage of 5 kV. (c) Frequency content at test voltage of 3 kV. (d) Frequency content at test voltage of 5 kV.

The frequency domain information of the UHF signals corresponding to surface discharges are manifested as peaks in the magnitude frequency response function. Two observations are possible from Figure 4.28 (c) and Figure 4.28 (d). The peaks appear dominant up to 100 MHz irrespective of the magnitude of test voltage. In addition to this, the magnitude of the peaks is proportional to the nominal amount of the applied test voltage. A second frequency response range in consequence of the surface discharges can be identified in the higher frequency span ranging from 500 MHz to 700 MHz. The peak is stable in the frequency span, while its magnitude also increases with rising test voltage. This indicates, that surface discharges of a tar-layered test object exhibit the corresponding frequency domain information in low and high frequency span.

4.3 Experiments on Test Insulator

The experiments on test insulator A are conducted in a test rig arrangement. Figure 4.29 shows the test rig that houses the test insulators involved in the present study. The test rig is mechanically designed in such a way that the complete arrangement closely emulates the actual electrical conditions of a ceramic feed-through bushing installed in a wet ESP unit.



FIGURE 4.29: Test rig used for housing the bottom half of the test insulators during the measurements.

4.3.1 Test Insulator Arrangement

The framework of the test rig is manufactured of aluminum and covered with aluminum sheets, while the top part is made of hard paper. The geometry of the flange connection, that are made of stainless steel (1.4301), is designed according to the mechanical support of the ESP chamber in which the HV insulator is fastened. The test rig surrounds the bottom part of the test insulator gas-tight, while the top part of the insulator is exposed to ambient condition. This provides an opportunity to gain control over the contamination like water droplets, tar coating etc. on the bottom part of the insulator.

4.3.2 Dielectric Response Analysis

4.3.2.1 Dielectric Response in Time Domain

Figure 4.30 shows the DC insulation resistance of the test insulator A.1 (with clean and dry surface), test insulator A.2 (with clean surface that is covered with

water drops) and test insulator A.3 (with a thin layer of wet tar on its surface), respectively.

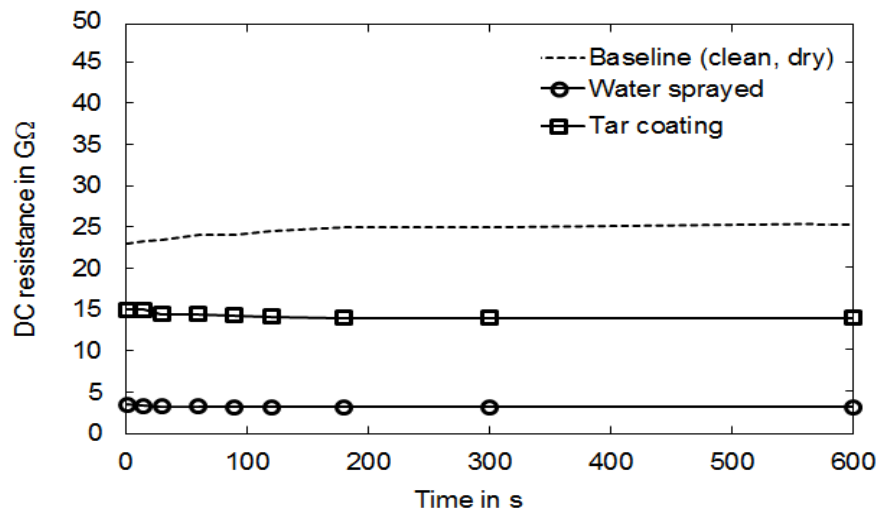


FIGURE 4.30: Time dependent dielectric response of the test insulator.

It appears from Figure 4.30 that the test insulator A.1, with clean and dry surface, emerges with a higher insulation resistance than that of the tar polluted test insulator (A.3) and the test insulator covered with drops of water (A.2). Comparatively, the test insulator with water drops on its surface seems to emerge as a severe case with higher conductivity compromising the dielectric quality of the insulator. The DC insulation resistance of the clean and dry test insulator (A.1) slightly increased over the measuring time from 23 GΩ to close to 25 GΩ, while the DC resistance of the test insulator with tar coated surface (A.3) and the test insulator that surface is covered with drops of water (A.2) show a slightly decreasing trend over the measuring time. The DC resistance of test insulator A.3 dropped from 15 GΩ to 14 GΩ, while the values of test insulator A.2 dropped from 3.5 GΩ to close to 3 GΩ. In other words, the test insulator A.2 with water drops on its surface emerges with higher conductivity than the tar coated (A.3) and the clean and dry (A.1) test insulator.

4.3.2.2 Dielectric Response in Frequency Domain

The Figures 4.31-4.37 show the results of the frequency-dependent dielectric behavior of the test insulators in a frequency range from 0.01 Hz to 1 kHz. Figure 4.31 shows the results of the loss factor, while Figure 4.32 (a) and Figure 4.32 (b) show the absolute values of the complex AC impedance and capacitance, respectively. It can be observed from Figure 4.31 that the loss factor of the clean and

dry insulator surface (baseline condition) emerges with a low value of 0.003 p.u. at 1 kHz, while the same increases with decreasing frequency to a value of 0.2 p.u. at 0.01 Hz. This loss factor shape is reported in the literature as the characteristic dielectric response of a homogeneous insulation [44]. Comparatively, the tar coated test insulator shows the same trend at high frequencies up to a value of around 2 Hz. Below this frequency of 2 Hz, the results show a clear deviation with a rising trend towards lower frequencies. However, the loss factor of the water sprayed test insulator surface shows a clearly different behavior. It matches at high frequency of 1 kHz more or less to the one of the baseline and the tar coated test insulator condition and shows a different shape with decreasing frequency values, with two inflection points (at 4 Hz and 0.04 Hz) and a comparably high value of 2.5 p.u. at 0.01 Hz.

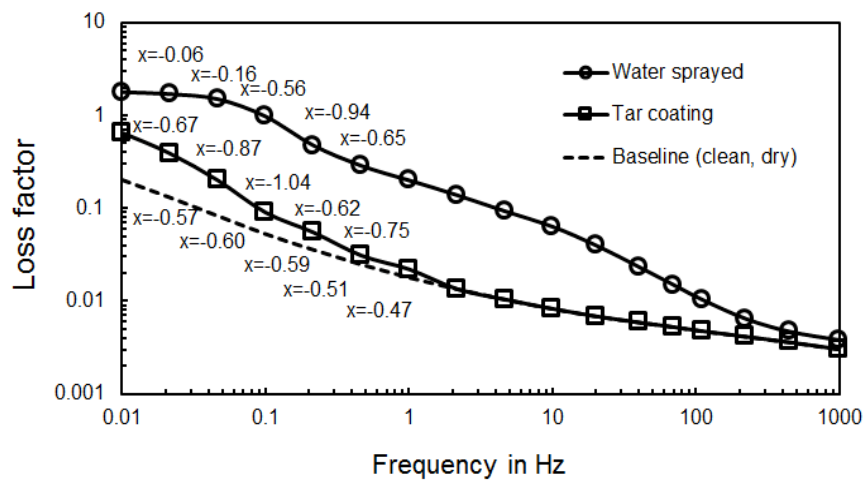


FIGURE 4.31: Loss factor ($\tan(\delta)$) of the test insulator installed in the test rig.

In addition to this, it can be observed from Figure 4.31 that the baseline condition of the clean test insulator exhibits a slope of close to $x = -0.6$ that is more or less constant at frequencies below 100 mHz. However, the surface polluted test insulator (tar under wet condition) exhibits a slope of around - 1.0 at 100 mHz, with a slightly decreasing trend to lower frequency values ($x = -0.67$ at 10 mHz), while the water sprayed test insulator shows a slope value of close to - 0.95 at 200 mHz that further decreases to close to $x = -0.1$ at a frequency of 10 mHz.

Figure 4.32 (a) shows the AC impedance of the clean and dry, tar coated and water sprayed insulators over a wide frequency range. The AC impedance matches at high frequency, while it deviates at low frequency. It can be observed from Figure 4.32 (a) that the test insulator with drops of water on its surface emerges with lower AC impedance. The test insulator surface coated with tar emerges to be better and closely line-up with the clean test insulator.

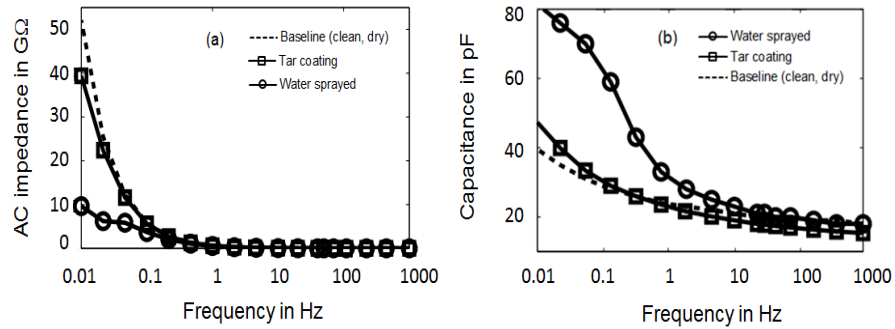


FIGURE 4.32: Frequency dependent dielectric response of the test insulator installed in the test rig. (a) AC impedance. (b) Capacitance.

However, such differences are found only at lower frequencies. At high frequencies, the AC impedance pertaining to clean, drops of water and tar coated insulators are similar. Comparatively, the DC resistance at low frequencies is less than the AC impedance (at least 2 times). Figure 4.32 (b) shows the capacitance of the three test insulators. It emerges from Figure 4.32 (b) that the permittivity of the insulators manifested by the clean and tar coated surfaces are more or less the same. Both the insulators (clean and tar coated) exhibit lower permittivity indicating no change in their condition. A slight increase in permittivity might appear for a tar coated insulator at very low frequency. The test insulator with drops of water on its surface emerges with drastic increase in permittivity.

Figure 4.33 and Figure 4.34 show the imaginary part and the real part of the permittivity over the measured frequency range, respectively. It becomes clear from Figure 4.33 that the dielectric loss of the clean test insulator manifests a low value of 0.003 p.u. at a frequency of 1 kHz and increases up to 0.2 p.u. at low frequencies. These findings are consistent with the fact that the outdoor and indoor ceramic insulators are prepared with low permittivity [103]. However, the tar coated test insulator shows a clear trend of increasing values with lower frequencies compared to the values of the baseline condition. On the contrary, the trend of the water sprayed test insulator shows a clearly different shape with comparable high dielectric loss values around 20 times higher than those of the baseline condition. The presence of water molecules on the test insulator surface clearly dominates the amount of the apparent loss current, while that one of the tar coated test insulator is comparably low.

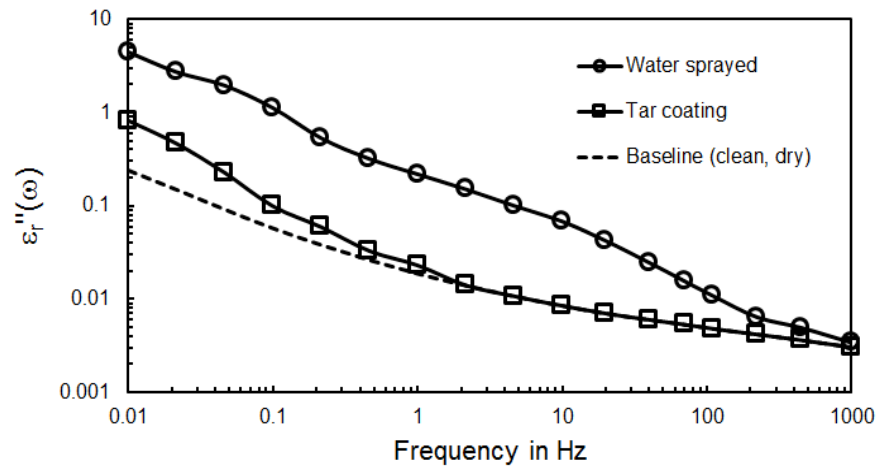


FIGURE 4.33: Imaginary part $\varepsilon_r''(\omega)$ of complex dielectric permittivity.

Figure 4.34 shows the frequency dependence of $\varepsilon_r'(\omega)$ of the different surface conditions of the test insulator. It can be observed from this Figure that the $\varepsilon_r'(\omega)$ values of the clean and the tar coated insulator are constant from 1 kHz to 100 Hz with a slight increasing trend to lower frequency values indicating the rising impact of polarization with decreasing frequencies.

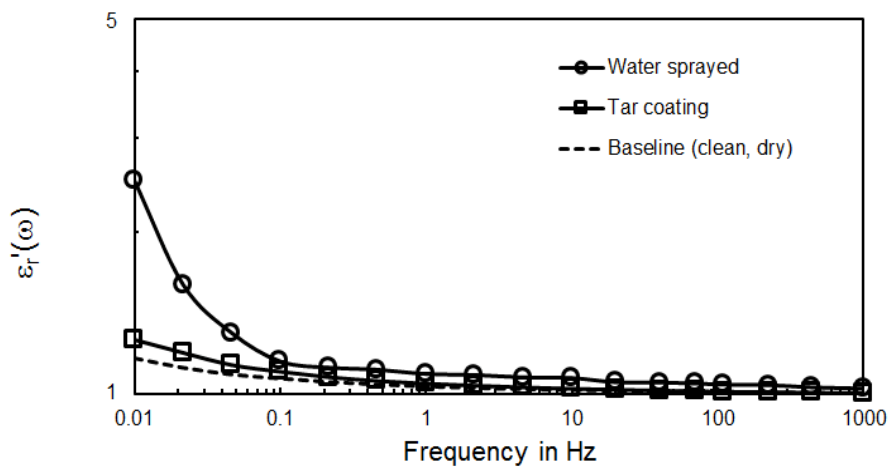


FIGURE 4.34: Real part $\varepsilon_r'(\omega)$ of the complex permittivity.

It can be concluded that the loss factor of the clean and tar coated insulator from 1 kHz to 100 Hz is a result of residual conductivity, while the $\tan(\delta)$ values below 100 Hz are affected by polarization. Furthermore, the water sprayed insulator shows a slight increase of the $\varepsilon_r'(\omega)$ values starting from 1 kHz, while the same increases drastically on the frequency is below 0.1 Hz. This indicates that the drops of water exhibit polarization mechanisms that becomes dominant at low frequencies.

Figures 4.35, 4.36 and 4.37 show the real part and imaginary part of the complex relative permittivity of the test insulator with the surface condition: baseline (clean and dry), tar-coated and water-sprayed. It can be observed from the Figures 4.35 and 4.36 that the real part of the relative permittivity exhibits a slope close to 0 at high frequency values and increases slightly once the frequency is below 10 Hz (refer to Figure 4.34). Instead, the imaginary part of the permittivity shows a steady rise with decreasing frequency values.

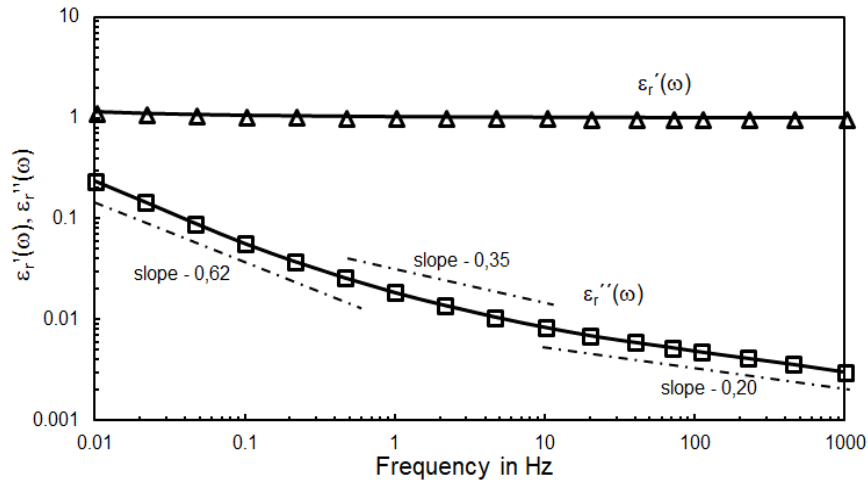


FIGURE 4.35: Complex relative permittivity of test insulator under baseline condition.

In addition to this, the water-sprayed test insulator surface shows a slight increase between 1000 Hz to 1 Hz and a strong dispersion at frequencies below 0.1 Hz, indicating a significant increase of the charging current towards low frequencies (refer to Figure 4.37). It appears from the Figures 4.35 and 4.36 that the imaginary part of the complex relative permittivity can be split into 3 regimes. At high frequencies the exponent values match, while the slope of the tar coated surface exhibits a stronger increase with decreasing frequency values.

It becomes clear from Figure 4.37 that the crossing over of $\varepsilon_r'(\omega)$ and $\varepsilon_r''(\omega)$ is around 0.1 Hz. This indicates the critical frequency, where the dielectric loss exhibits higher values than that one of the reversible charging current (represented by $\varepsilon_r'(\omega)$) [98]. Below this critical frequency the loss factor decreases in consequence of the rising amount of charging current (refer to Figure 4.31). It can be observed from the Figures 4.35 and 4.36 that the dielectric response of the clean and tar coated test insulator surface is comparable with that one of a *RC parallel circuit* with a leaky capacitor, where the slope of the real part of the complex relative permittivity is more or less 0 over the analyzed frequency range, while the imaginary part exhibits an exponential rise (linear in double logarithmic scale) with decreasing frequency values. Nevertheless, the rise of $\varepsilon_r''(\omega)$ under clean and

tar-coated surface condition shows a slight different shape that is similar to the dielectric response of solid dielectrics reported in [98, 99, 124].

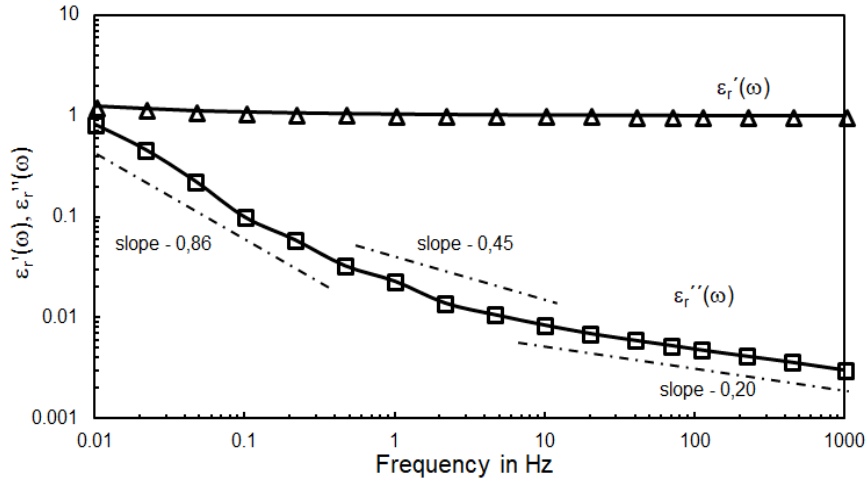


FIGURE 4.36: Complex relative permittivity of test insulator under tar-coated surface condition.

The dielectric response of the clean test insulator can be considered as the basic LFD behavior of ceramic material in consequence of low frequency polarization mechanisms in the bulk and at the grain-boundary, the occurrence of space-charge as well as electrode-sample polarization [99, 125]. The rising trend of $\epsilon_r''(\omega)$ towards lower frequencies indicates an increasing polarization phenomena in a frequency band below 100 Hz, which has to be considered as superimposition of individual polarization mechanisms (electron hopping, interfacial polarization, ohmic conduction and in the presence of moisture and polar molecules the migration of mobile charge-carriers and dipolar response) [100].

In addition to this, it can be observed from the Figures 4.35 and 4.36 that the slope of the imaginary part is around -0.20 at high frequencies, that can be attributed to an electron hopping mechanism ($0.6 \leq n \leq 0.8$). The stronger dispersion of $\epsilon_r''(\omega)$ to lower frequencies in the presence of tar (refer to Figure 4.36), where the slope is > 0.7 , can be as well attributed to relaxation phenomena of hopping charges [97, 99, 125]. On the other hand, the water-spayed surface with distributed single water droplets shows the same behavior at high frequencies > 100 Hz, while the frequency response below 0.1 Hz seems to be dominated by interfacial polarization mechanisms that are comparable with a uniform distributed *RC network*, where the slope of $\epsilon_r'(\omega)$ and $\epsilon_r''(\omega)$ exhibits a value of around $-1/2$ ($n = 1/2$) representing the physical phenomena of diffusion mechanisms [97]. However, it is reported that the dielectric response can be described mathematically by asymmetrical and asymptotic power laws [101]. Nevertheless, a deeper insight into the

individual mechanisms of the LFD phenomena and their contribution to the integral dielectric response that is measurable could be gained only by further analysis on microscopical scale.

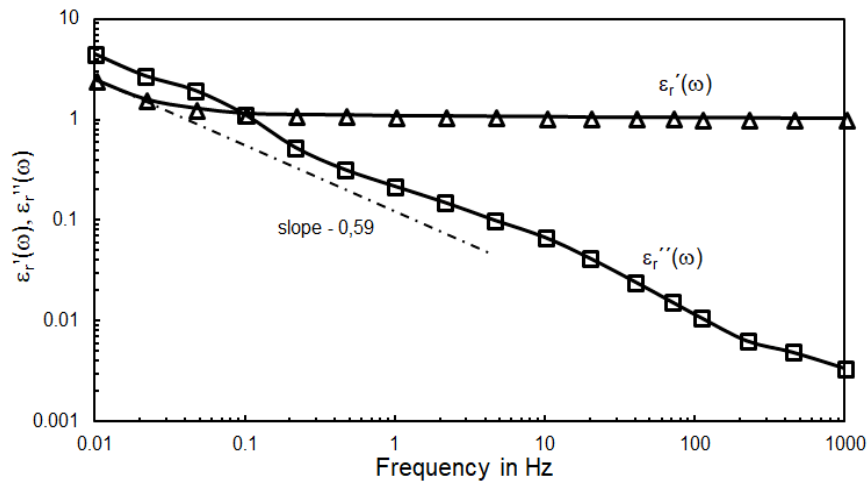


FIGURE 4.37: Complex relative permittivity of test insulator under water-sprayed surface condition.

In all, the results of the test insulator under laboratory conditions (refer to Figure 4.31, 4.32, 4.33 and 4.34) show that it is possible to employ modern diagnostic test methods in assessing the dielectric condition of the insulator surface. The clean insulator emerges with a low loss factor at 1 kHz that slightly increases throughout the frequency range. At the same time, the loss factor of the water sprayed insulator emerges as the highest, which is as expected. It appears from Figure 4.31 and Figure 4.33 that below a frequency of 1 Hz the tar depositions on the insulator surface clearly influences the values of $\tan(\delta)$ and $\varepsilon_r''(\omega)$ with increasing trend of deviation to lower frequencies. The findings from the water sprayed insulator can be assumed as indication of the worsening dielectric condition on the tar polluted insulator under the impact of the increasing content of moisture. Since the $\varepsilon_r'(\omega)$ values increases in the lower range of the test frequency (refer to Figure 4.34), it arises that the minor rising trend of the loss factor values, indicated by the decreasing values of the slope (refer to Figure 4.31), is a result of the increased charging current in consequence of polarization that compensates the loss current and thereby exhibiting an approximately linear increasing trend (refer to Figure 4.34).

4.3.3 PD Signal Analysis in Time and Frequency Domain

Figure 4.38 shows the time domain representation of the PD signal that arises on the surface of a clean (test insulator A.1) and a tar polluted (test insulator

A.3) test insulator (Figure 4.38 (a) and Figure 4.38 (b)), while their respective frequency domain representation is shown in Figure 4.38 (c) and Figure 4.38 (d).

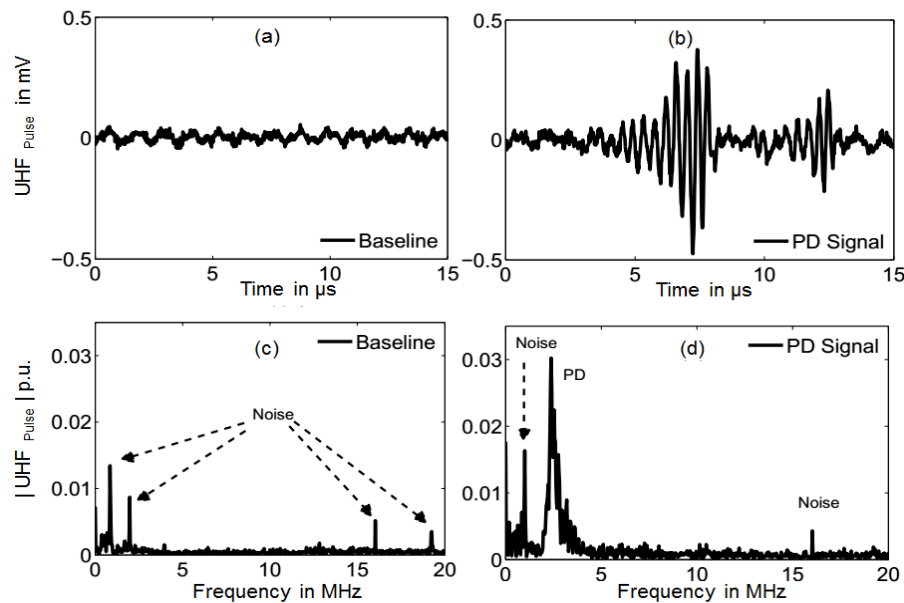


FIGURE 4.38: Time and frequency domain of the PD signals that arise on the clean (test insulator A.1) and with tar contaminated surface (test insulator A.3) measured at 3 kV AC. (a) Time domain of the test insulator A.1. (b) PD signal in time domain of the test insulator A.3. (c) Frequency domain representation of A.1. (d) Frequency domain representation of A.3.

The condition of the clean test insulator is labeled with baseline. It can be observed from Figure 4.38 (c), measured from the clean test insulator A.1, that there are few noise sources that coupled with the measurements. Such noise sources render practically invisible in real time PD signals (refer to Figure 4.38 (a)). However, the measured PD signals appear dominantly. It can be noted from Figure 4.38 (b) and Figure 4.38 (d) that the measured PD signal becomes clearly observable in its respective time and frequency domain representation. Similar to the investigations of the test sample with dry deposition layer of tar (refer subsection 4.2.2.1.5.2) manifests the frequency domain representation of the PD signal from a wet tar layer likewise a dominant peak at around 2 MHz. It also can be observed that the amplitude of noise sources in the low frequency range is slightly elevated.

Validation

5.1 Procedure

The test object used in the present work for validation purpose is a wet type ESP unit installed in a laboratory scaled biomass gasification plant. Figure 5.1 shows the respective flowchart of the biomass gasification plant with the downstream apparatus for producer gas cooling and cleaning, respectively. The gasifier unit consists of 3 reactor segments: a hopper with screw conveyor for volumetric dosing of the biomass feedstock (pine-wood chips), the fluidized bed reactor where the auto-thermal thermo-chemical conversion of the feedstock together with the gasifying agent (air) at ambient pressure and a temperature of 700-900 °C occurs and a freeboard segment for ensuring a certain value of residence time of producer gas at around 800 °C. Before each operation the fluidized bed reactor is filled with a certain amount of charcoal particles as reactive bed material and the gasification plant is flushed with N_2 in order to purge oxygen out of the plant avoiding the risk of explosion during the start-up procedure. Once this is ensured, the electrical trace heating elements of the gasifier, freeboard and hot gas particle filter are set to 800 °C and 400 °C respectively. After the reactor surfaces have reached a temperature of around 600 °C wood-chips with a mass flow rate of 3 kg/h are fed into the fluidized bed and the flow rate of gasifying agent is set to a value ensuring an equivalent ratio of 0.2-0.3. The producer gas of around 6 Nm³/h generated in the fluidized bed streams upwards into the freeboard and is subsequently cooled by a heat exchanger ensuring the operating temperature of the hot gas filter of approximate 400 °C where solid particles, i.e. char particles and ash, are removed out of the producer gas without condensation of its containing gaseous hydrocarbon and hetero-cyclic compounds. Subsequently, the producer gas is cooled in a

quench unit by spraying bio-diesel into the hot producer gas. In consequence of the temperature drop to around ambient condition (less than 35 °C) gaseous hydrocarbon and hetero-cyclic compounds together with steam condense and form liquid aerosols. These aerosols entering into the wet ESP unit are charged by the applied electric field and further deposit on the ground electrode of the ESP, where they are collected. The cleaned producer gas containing certain amounts of non-condensed hydrocarbon and hetero-cyclic compounds flows subsequently into a natural gas supported gas burner, where the producer gas is oxidized.

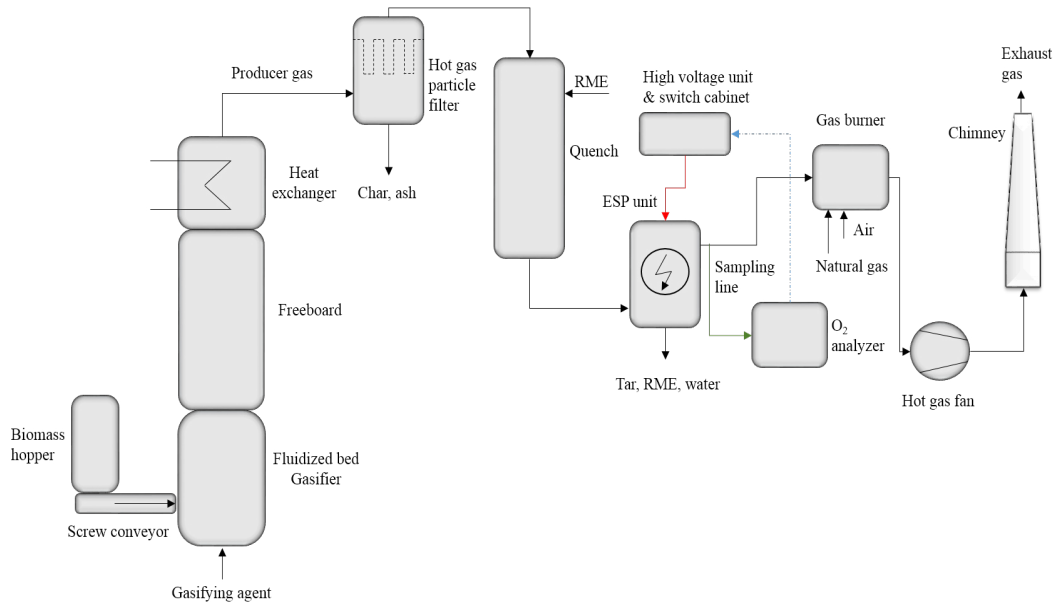


FIGURE 5.1: Flowchart of laboratory scaled fluidized bed biomass gasification plant.

The chosen wet ESP unit (shown in Figure 5.2) is laboratory-scaled, designed as single stage single wired filter, and contains a circular-cylindrical shaped collection electrode and a coiled discharge electrode. The operating voltage of the ESP unit is supplied by an HV rectifier unit (type ESO-40-42-70 Si, with $U_{eff} = 42$ kV and $I_{eff} = 70$ mA at the secondary terminals) and is controlled by an analog HV control unit (type 835) from Rico-Werk Elektronik ensuring high level of HV supply voltage to the electric field of the ESP unit, while limiting the events of sparks to a minimum. At first, a new feed-through type ceramic insulator and discharge electrode suspension are installed in the HV chamber of ESP unit. The baseline data is measured and the dielectric integrity of the new insulator, with clean and dry surface condition, is ensured. The baseline data comprises recording the surface dielectric properties over a wide span of time and frequency and exercising online PD test methods. Once this is ensured, the ESP unit is flushed with Nitrogen (N_2) in order to remove the Oxygen (O_2) from the chamber. This is necessary to ensure the operating conditions of the wet ESP unit well before

producer gas flows through it to avoid that high concentrations of condensable hydrocarbon and hetero-cyclic compounds reach the HV insulator causing immediate surface pollution and thereby a degradation of the ESP removal efficiency within the shortest time. Furthermore, a continuous monitoring of the producer gas O_2 concentration is necessary for safety reasons while the combustible producer gas is cleaned since the presence of small amounts of O_2 lead into a potentially explosive atmosphere that could be sparked by any discharge of the ESP unit. Once safe operating conditions for cleaning of producer gas are ensured ($O_2 \leq 2$ vol.-%), the ESP unit is turned on and the space between the high voltage discharge and collecting electrode is energized. The N_2 flushing is stopped and the producer gas generated by the gasification of wood-chips flows by forced convection due to pressure differences into the cleaning chamber of the ESP unit, while for safety purpose the O_2 content in producer gas is continuously monitored.

The electrical discharges that arise between the discharge and collecting electrode and on the surface of the ceramic insulator are monitored through online PD measurements. The PD signals are decoupled from the ground wire through a HFCT. In parallel, the operating voltage and current consumed by the ESP unit are measured. This approach is necessarily exercised in support of online PD measurements in order to identify if the discharges are between electrodes or on the surface of the insulator. Once surface discharges arise, the ESP unit is brought to offline and the time and frequency dependent measurements are exercised. The measured data is then compared with the baseline to assess the condition of the insulator. This process is repeated until the ESP fails or is unable to charge the discharge area with more than 5 kV. Once this condition is reached, it is understood that the surface of the insulator is highly contaminated, the ESP operation fails and the HV insulator has to be exchanged. Following this, the surface of the insulator is heated and the dielectric and PD behaviors are measured respectively at 3 hrs. and 6 hrs. Subsequently, the measured data are analyzed to understand the influence of a tar contaminated surface on the integral dielectric condition of the HV insulator.

5.2 Electrostatic Tar Precipitator Unit

A laboratory scale wet ESP unit is chosen for validation purposes. Figure 5.2 shows a 2-dimensional sketch of the wet ESP unit along with the installation arrangement of the ceramic insulator on the top chamber and the pertaining high voltage supply unit, respectively. The ESP unit is designed for an integral collecting efficiency of 96 % with an operating voltage of around 35 kV DC, while the pertaining

discharge current is limited to around 20 mA. The operating parameter of the ESP unit (applied voltage and secondary current) are measured on the secondary side of the thyristor module. A voltage divider is applied to determine the secondary voltage while the secondary current is gained from a feedback voltage signal that is provided by a shunt-resistor based on the thyristor secondary current rating. A HV ceramic insulator is used for providing mechanical support and electrical insulation between the HV electrode and grounded tank. The chosen ceramic insulator is a feed-through type and made of siliceous porcelain which is popularly used in ESP units [64, 126]. It is manufactured according to the standard BS 2562 and has a glazed surface.

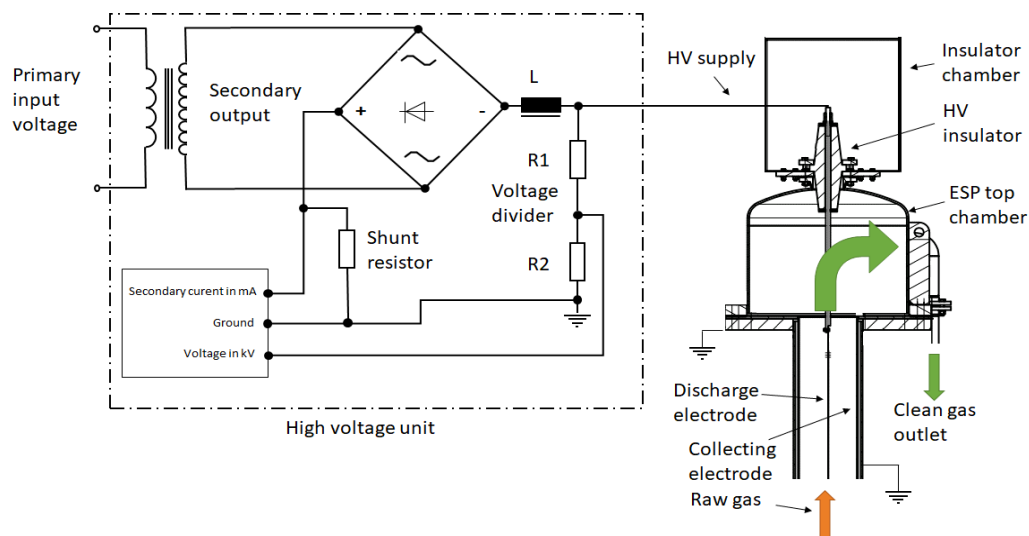


FIGURE 5.2: Wet ESP unit involved for experimental validation.

5.2.1 Conventional Operation Performance Monitoring

By far, the most convenient solution for the determination of the ESP performance is to record the applied voltage and secondary current (U-I curve) during the start-up process. Thereby, it is possible to evaluate the condition of the pertaining HV insulators by referencing to the baseline data recorded from the same ESP unit after mechanical installation [78]. Figure 5.3 shows the U-I-curve of the actual ESP unit, which is applied for validation purpose. It becomes clear from this Figure that the U-I-curve of the ESP unit exhibits an exponential rise under clean insulator surface condition. Furthermore, the increase of leakage current in consequence of depositions on the HV insulator surface lowers the exponential rise, while an ESP unit with a highly compromised insulator surface exhibits a clear linear rise of the U-I-curve.

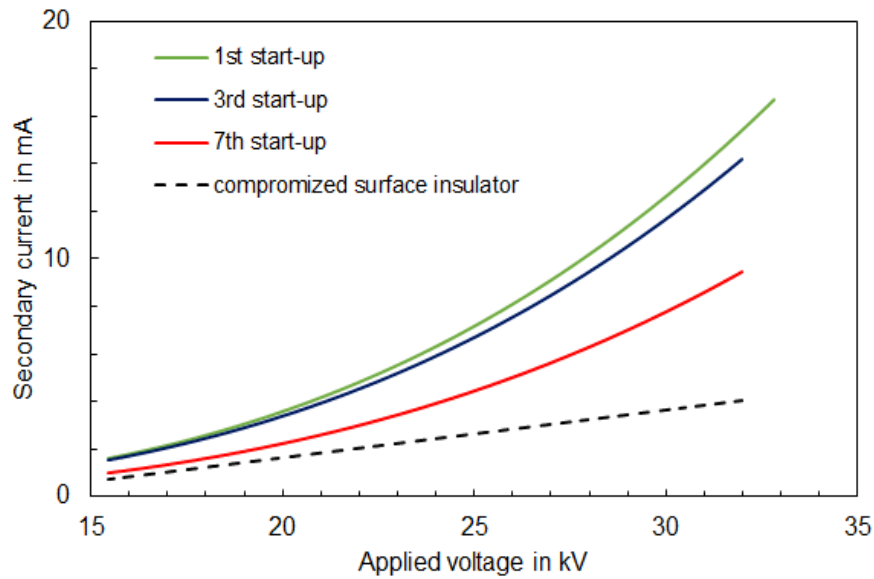


FIGURE 5.3: ESP voltage-current curve.

In addition to this, the impact of the glazing layer on the insulator surface onto the operation performance is shown in Figure 5.4. The blue U-I-curve is recorded at the beginning of the 8th start-up of the gasification plant, while the black U-I-curve is recorded after the ESP unit has performed around 15 min. of operation. The gray U-I-curve corresponds the 11th start-up of the plant, while the green U-I-curve is recorded after around 20 min. of operation, respectively. It becomes clear from Figure 5.4 that the U-I-curve is recovered to a certain amount after the ESP unit has operated for several minutes. This "self-recover" can be addressed to the amount of leakage current on the insulator surface provoked by the glazed surface layer that provides a certain amount of thermal heat to the insulator. In consequence, the surface deposition layer dries and the amount of loss current caused by the deposition layer is reduced, while the nominal discharge current is slightly increased.

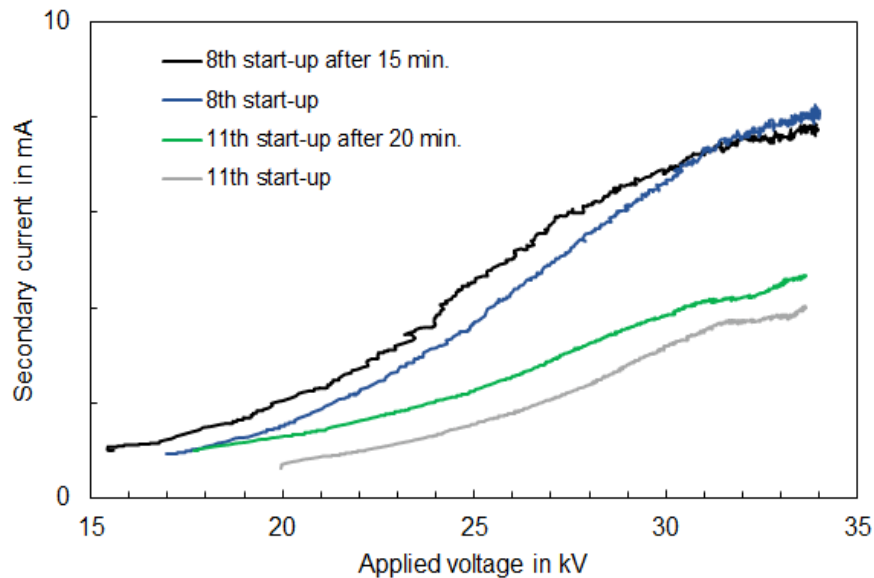


FIGURE 5.4: ESP unit voltage-current-curve.

5.2.2 Recovery of Operational-Based Performance Loss

Being a feed-through type, one half of the ceramic insulator remains clean in the HV chamber, while the other half remains in the cylindrical cleaning chamber exposed to a stream of relatively contaminated producer gas. The continuous exposure of the insulator to the mildly contaminated gas has compromised the performance of the ESP and has limited its service time. In consequence, the operating voltage of the ESP unit is reduced from 35 kV to 5 kV. The degree of reduction of operating voltage can be correlated to the amount of tar deposited on the surface of the ceramic insulator. Once the operating voltage has reached 5 kV, the ESP cannot be operated further since the electric field between the discharge and collecting electrode remains insufficient in ionizing the aerosols of tar that are present in the producer gas. The deposition layer on the surface of the insulator behaves like a conductor of low resistance that permits a further rise of the operating voltage. A possible way to regain its dielectric quality is to dry the surface of the insulator by surface heating which is experimentally investigated through monitoring of the operating voltage and current of the wet ESP unit. Figure 5.5 (a) and Figure 5.5 (b) show the operating voltage and the respective secondary current of the ESP unit during producer gas cleaning. It can be observed from Figure 5.5 (a) that the contamination on the insulator surface reduced the operating voltage of the ESP unit from 35 kV to 5 kV. At the same time, it is possible to increase it from 5 kV to 20 kV through surface heating. However, it appears from Figure 5.5 (a) that beyond 6 hrs. of heating a further increase in

the operating voltage is not notable.

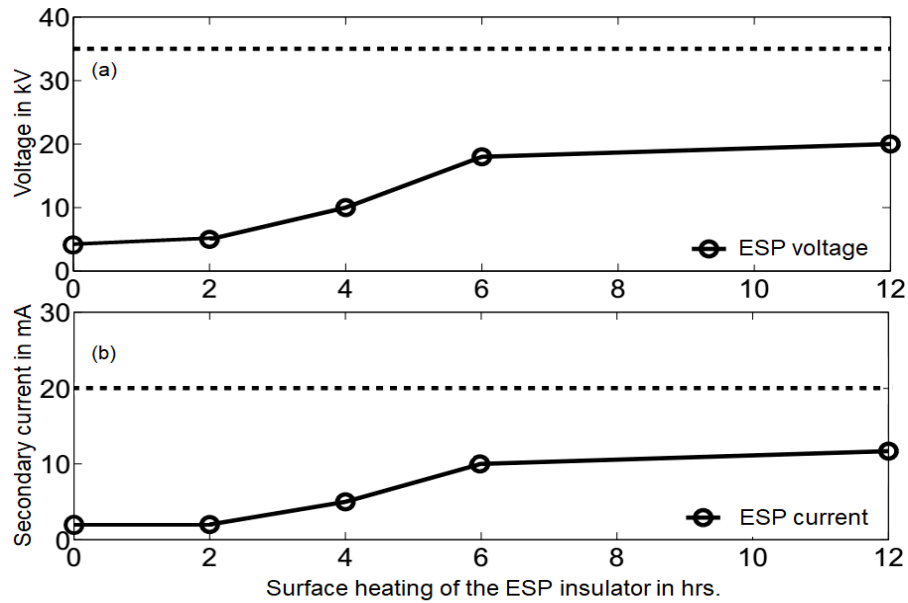


FIGURE 5.5: Operating voltage and current of ESP unit with tar contaminated ceramic insulator. (a) Voltage. (b) Current.

5.3 Dielectric Response Analysis

A photo of the test setup adopted for resolving the dielectric condition of the ceramic insulator installed in the chosen wet ESP unit is shown in Figure 5.6 (a) and Figure 5.6 (b), while the corresponding sketch of the test setup applied for measuring the time and frequency response of the test insulator is shown in the Figures 5.7 (a) and 5.7 (b), respectively. The test equipment (MIT 1020, DIRANA) and respective procedures are similar to the method adopted on test sample and test insulator. The test voltage is fed through the high voltage electrode, while the time and frequency dependent responses are measured from the grounded top flange of the ESP.

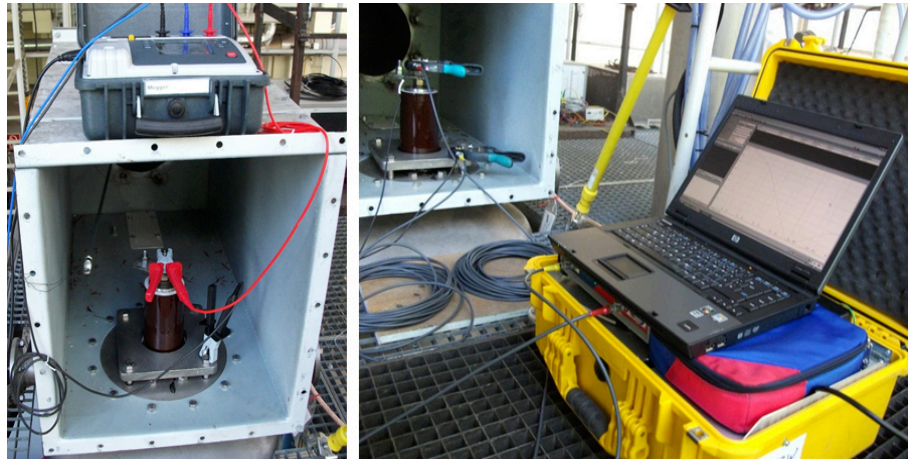


FIGURE 5.6: Photo of the dielectric response test setup. Left: Time domain analysis (MIT 1020). Right: Frequency domain analysis (DIRANA).

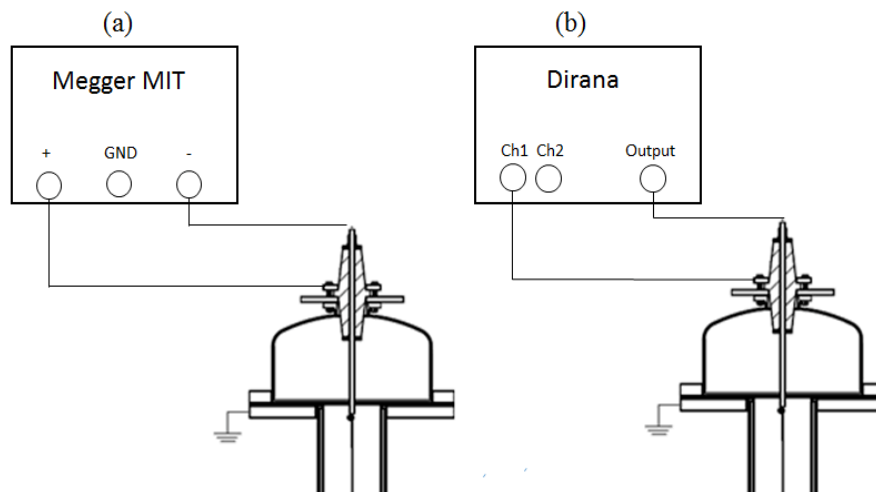


FIGURE 5.7: Schematic of test setup used to measure the dielectric response of test insulator installed in the test rig and the wet ESP unit over a wide range of time (a) and frequency (b).

5.3.1 Dielectric Response in Time Domain

Figures 5.8 (a) and 5.8 (b) show the dielectric condition of the clean and tar polluted surface of the support insulator in time domain. The measurement is made directly at the grounded flange of the insulator, while the same remains installed in the chosen wet ESP unit. As explained earlier, the bottom half of the insulator is polluted with wet tar, while the top half remains clean and dry. Nevertheless, the apparent dielectric condition of the insulator seems to be highly compromised which can be assessed through the time dependent DC insulation

resistance measurements. Figure 5.8 (a) shows the insulation resistance of the new insulator with clean and dry surface installed in the chosen ESP unit. It becomes clear from the Figure 5.8 (a) that the insulator with clean and dry surface manifests a high insulation resistance.

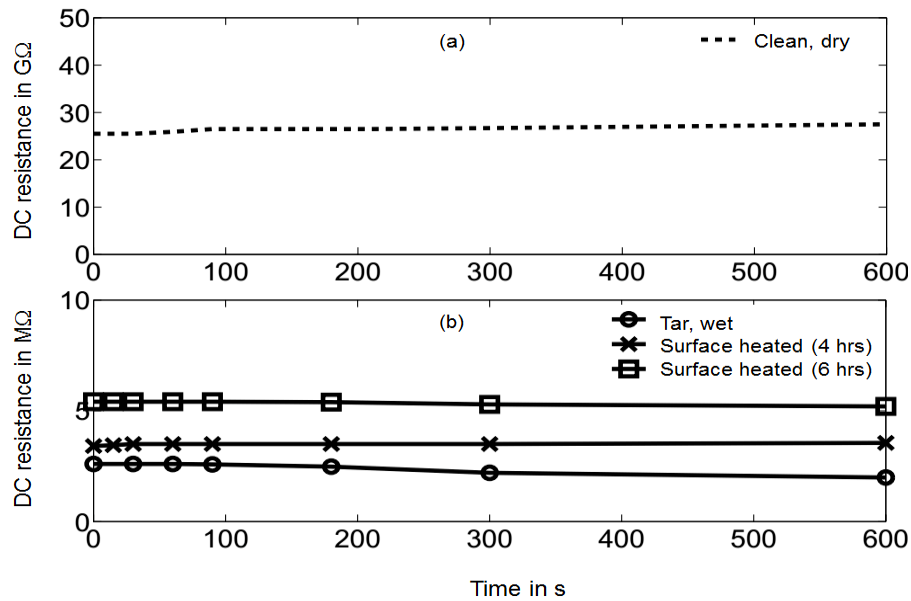


FIGURE 5.8: Time dependent dielectric response (DC insulation resistance) of clean and tar polluted surface of an actual ceramic insulator installed in a wet ESP unit measured over a wide time span. (a) Clean and dry surface. (b) Severe tar polluted surface.

The insulation resistance of the insulator with dry clean surface emerges with a value close to 25 GΩ. This value is closely matches with the data of the new test insulator installed in the test rig. This observation validates the usage of the test rig to ascertain the dielectric condition of the test insulator without the influence of the geometrical condition in a wet ESP unit. At the same time, the insulation resistance (shown in Figure 5.8 (b)) of the contaminated insulator surface, under different states of surface pollution level, has dropped to a very low value in the range of MΩ. Figure 5.8 (b) shows the respective values and trend of the insulation resistance measured with respect to time. The resistance pertaining to the tar-layered surface with wet condition manifests a value of close to 2 MΩ. Surface heating is capable to improve the surface condition of the polluted insulator up to a certain extent. The DC resistance is improved from 2 MΩ to 5 MΩ upon heating. Such an increase in DC resistance can be attributed to reduction of water content on the surface of the tar contaminated insulator surface. Consequently, the ESP operating voltage is improved from 5 kV to 20 kV, while the actual dielectric quality of the surface of the polluted ceramic insulator remains compromised.

5.3.2 Dielectric Response in Frequency Domain

Figures 5.9 (a) and 5.9 (b) show the frequency dependent AC impedance of clean and tar polluted surfaces of the support insulator. Altogether, it appears from these figures that modern frequency dependent dielectric response measurements can be applied for resolving the dielectric condition of the tar polluted ceramic insulator of a wet ESP unit.

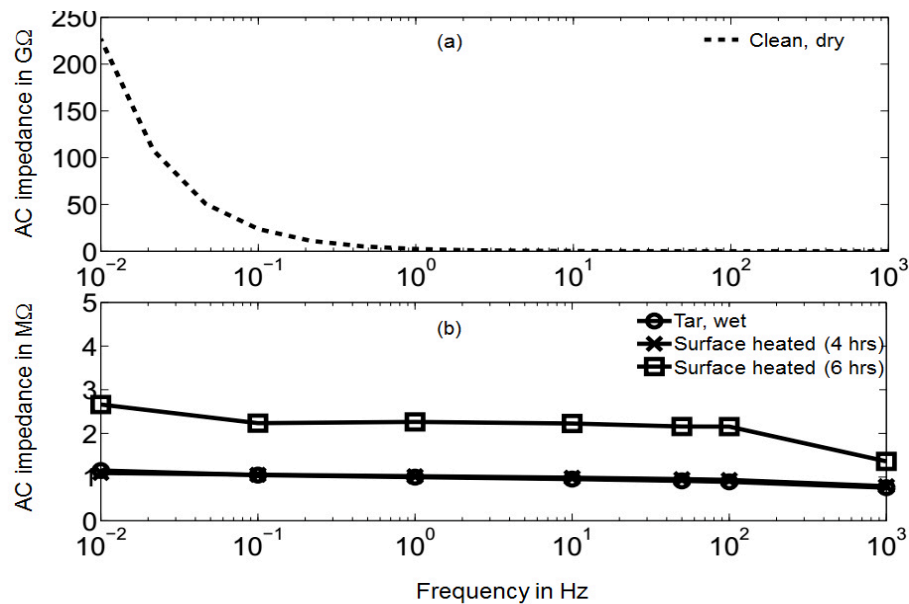


FIGURE 5.9: Frequency dependent AC impedance of a ceramic insulator installed in a wet ESP unit. (a) Clean/dry surface condition. (b) Severely contaminated surface condition.

The insulator with clean and dry surface emerges with better dielectric properties, while the corresponding AC impedance of the insulator with clean surface emerges with a value in $G\Omega$ which further increases with decreasing frequency values. The increase in AC impedance is quite drastic at frequencies in the sub-harmonic range. At the same time, the dielectric condition of the insulator with polluted surface (tar, wet) remains highly compromised. The AC impedance of the polluted insulator (shown in Figure 5.9 (b)) manifests a very low value (in $M\Omega$). Also, the drastic increase in impedance is lost. The surface heating improved the impedance of the contaminated insulator only to a small extent.

Figures 5.10 (a) and 5.10 (b) show the loss factor pertaining to the clean and the polluted states of the ceramic insulator. The clean insulator emerges with less loss of close to 0.002 p.u. at 100 Hz and increases with decreasing frequency the value of 0.1 p.u. at 0.01 Hz, respectively. Furthermore, with decreasing frequency values the slope of the loss factor increases from - 0.4 to - 0.65. The polluted

insulator emerges to be with high loss (Figure 5.10 (b)) which further increase with decreasing frequencies. At a 10 mHz test frequency, the loss factor of the insulator covered with wet tar is around 23 p.u. which is at least 200 times more than the value measured with a clean surface condition of the insulator (refer to Figure 5.10 (a)). The surface heating improved the loss factor only to a minor level. The loss factor is reduced to a value of 20 p.u. after 4 hrs of heating and to a value of 5 p.u. after 6 hrs of heating, while the loss factor trend indicates a finite value of the loss factor with decreasing frequency.

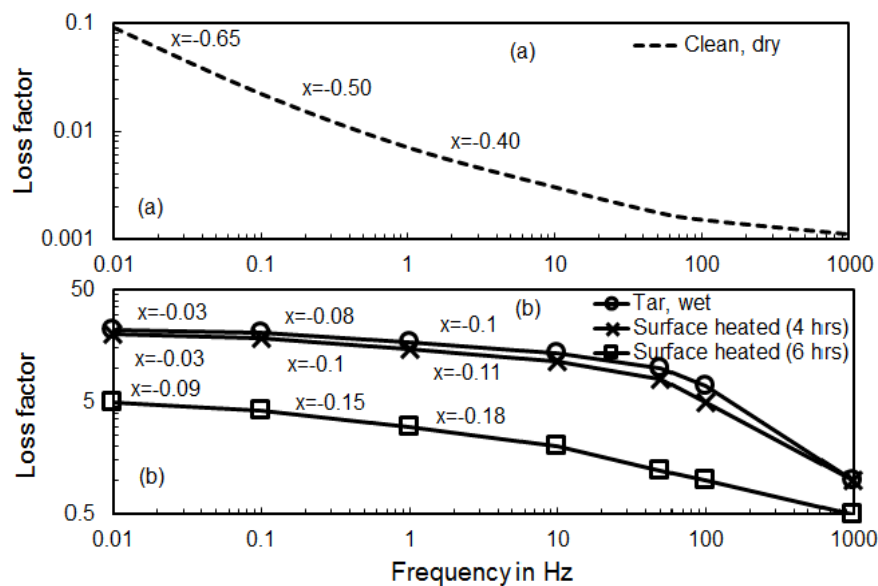


FIGURE 5.10: Frequency dependent loss factor ($\tan(\delta)$) of a ceramic insulator installed in a wet ESP unit. (a) Clean and dry surface condition. (b) Tar polluted surface condition.

Figure 5.11 shows the frequency dependent capacitance of the ESP HV insulator under clean and dry condition (a) and under tar polluted surface condition (b). The capacitance of the insulator with clean and dry surface shows a constant value from 1 kHz to 100 Hz, while the same increases slightly with decreasing frequencies and reaches a value of close to 2 pF at 0.01 Hz. The HV insulator polluted with tar shows the same rising trend over the measured range of frequency exhibiting higher capacitance values. It can be found from Figure 5.11 (a) that the loss factor increase of the clean and dry HV insulator at high frequencies (from 1 kHz to 100 Hz) is a result of residual conductivity, while the increase of the loss factor slope values with decreasing frequencies is a result of polarization loss in consequence of the increasing capacitance. In addition to this, it can be concluded from Figure 5.11 (b) that the minor rise of the loss factor to lower frequencies is a result of the increasing charging current in consequence of polarization. Since

the loss factor trend shows a finite value at very low frequency values it becomes clear that the rising charging current compensates the influence of the loss current. Furthermore, it can be found from Figure 5.10 (b) on the one hand that this effect becomes more dominant with the increase of water in the tar deposition layer. On the other hand, the comparatively low loss factor values of the tar pollution layer heated over 6 hrs clearly indicate the impact of reduced surface conductivity and thereby the worsening influence of water onto the magnitude of the loss factor and the respective dielectric condition of the insulator.

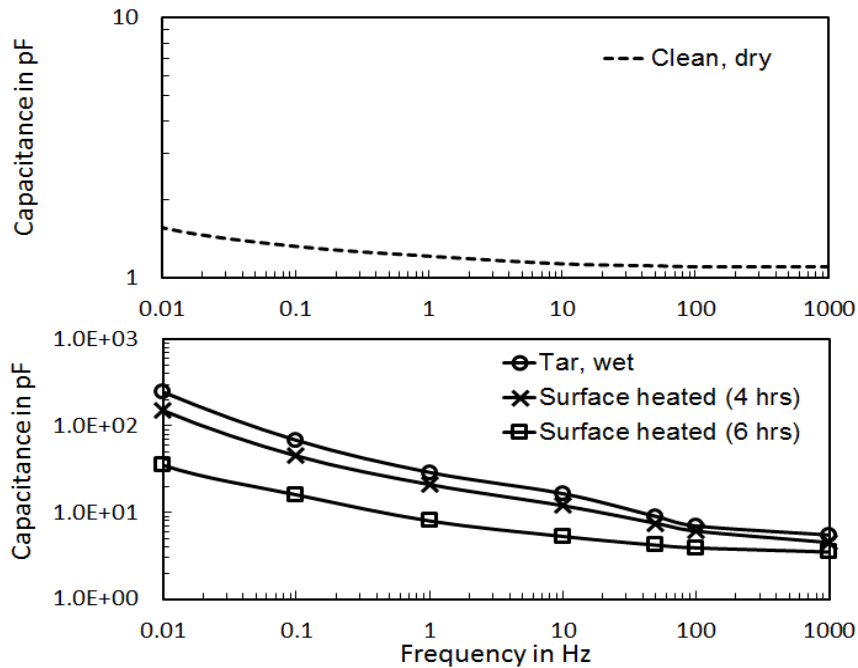


FIGURE 5.11: Frequency dependent capacitance of a ceramic insulator installed in a wet ESP unit. (a) Clean and dry surface condition. (b) Tar polluted surface condition.

Furthermore, it can be observed from Figure 5.10 (a) that the loss factor of the HV insulator installed in the ESP unit shows the same trend and comparable slope values over the frequency range as the clean test insulator investigated in chapter 4 (refer to Figure 4.31). So, the findings from the test insulator (with clean and dry surface) under laboratory conditions are congruent with the results gained from the actual ESP unit. In addition to this, the results of the loss factor gained from the ESP unit with a polluted insulator (wet tar and surface heated) are a few orders in magnitude higher than those of the test insulator installed in the test rig (refer to Figure 4.31). The slope values of the polluted insulator of the ESP unit (refer to Figure 5.10 (a)) only show a slight variation (from - 0.18 to - 0.03) over the frequency range and match to that of the water sprayed condition of the test insulator in the test rig at a frequency below 40 mHz (refer to Figure

4.31). This indicates, on the one hand, the presence of partial capacitance on the ESP insulator as a result of interfacial polarization mechanisms, exhibiting high time-constant values, while the same show a minor impact in case of the tar coated test insulator. This might be due to the fact that the amount of dissolved water in the coated layer of tar is comparatively low. On the other hand, since the test insulator is investigated under laboratory conditions, it becomes clear that the collective response of the HV insulator installed in the ESP unit is superimposed by several polarization mechanisms.

5.4 Partial Discharge Analysis

An online PD test method is involved in the present study. The PD signals are decoupled from the grounded flange connected close to the insulator arrangement. Figure 5.12 shows the online PD test setup adopted for measuring the electrical discharges that arise on the surface of the ceramic insulator of the chosen ESP unit. The setup (Figure 5.12) comprises a HFCT as measuring sensor and a PD detector with a wide range of measuring frequency (DC to 20 MHz). The high voltage source unit comprises a transformer and a full bridge rectifier unit. Being a feed-through type ceramic insulator, the high voltage electrode passes through the ceramic insulator and remains suspended in the cleaning chamber. The HFCT is connected to the ground strip of the ESP tank and the respective PD signals are electromagnetically decoupled through the same. The measured PD signals are synchronized with AC voltage which is fed to the full bridge rectifier unit of the ESP. Since the operating voltage that is applied to industrial ESP units is in general DC it becomes clear that the partial discharges that are measured from the ESP unit are analyzed as QPRPD pattern.

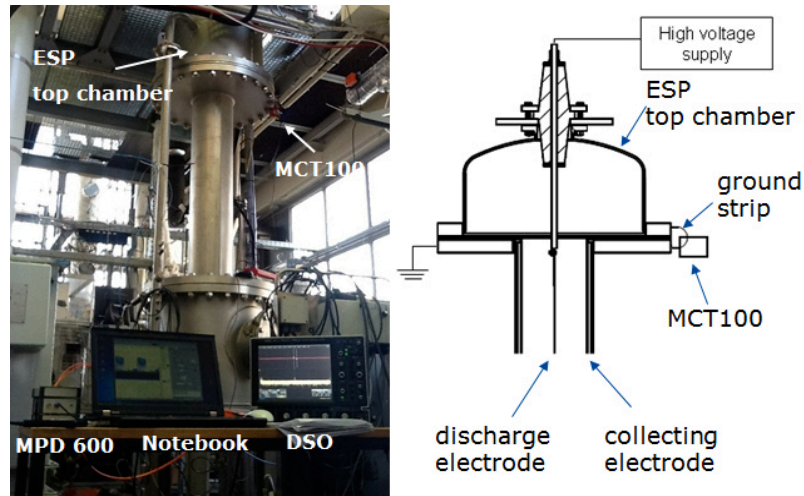


FIGURE 5.12: Online PD test setup. Left: Photo. Right: Schematic.

5.4.1 PD DC Performance Check

Initially, the baseline noise that couples with the PD measuring circuit is measured. During baseline measurements, the hard-wired high-voltage supply of the ESP unit is disconnected while the pertaining high-voltage transformer of the ESP unit is set to the nominal operating voltage of close to 35 kV. Figure 5.13 shows the PRPD pattern pertaining to baseline noise. It can be observed from Figure 5.13 that the apparent charge level of the background noise is within an acceptable level of less than 2 pC.

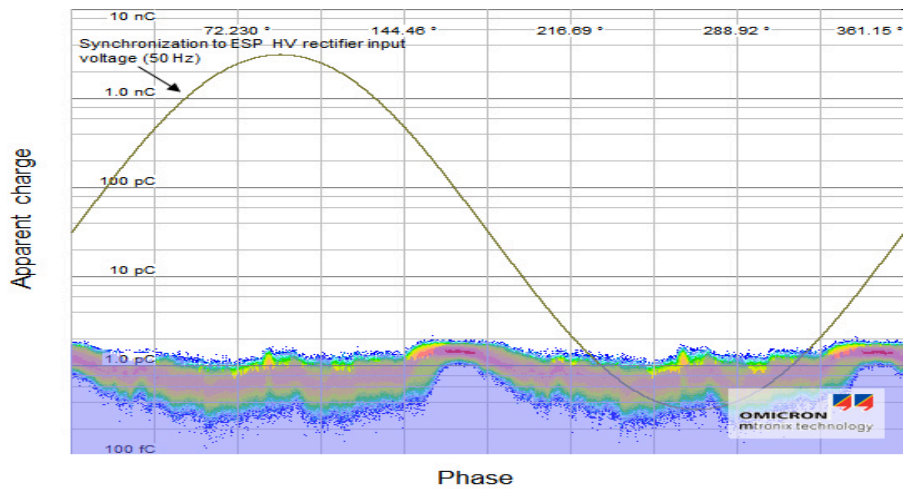


FIGURE 5.13: QRPD pattern of baseline noise during ESP unit open-circuited measured at -35 kV DC (PD level of 1.65 pC).

5.4.2 QPRPD Analysis

5.4.2.1 QPRPD Pattern Analysis

Figure 5.14 shows the PRPD pattern pertaining to severely polluted conditions of the ESP HV insulator surface. The important point to note is that strong discharges appeared even at an ESP operating voltage of - 5 kV DC. Furthermore, since the ESP HV rectifier is under these condition of the HV insulator only capable to build up an operating voltage of - 5 kV DC it becomes clear that the insulator surface is highly conductive in consequence of the polluted surface. The first observation that can be made from Figure 5.14 is that the discharges show a clear repetition in the 1st and 2nd half of the cycle of the synchronization voltage. This is reasonable, since the ESP operating voltage is a rectified voltage. From this it follows that the rectifier unit has a high ripple of the output voltage. Furthermore, it can be observed from Figure 5.14 that the corresponding apparent charge level of the individual PD pulses is up to 40 pC, indicating severe PD activity inside the ESP unit. The phase-resolved PD pulses also remained more intense and stable and can be assumed as two different discharge mechanisms. PD source A shows a small rate of pulses with high apparent charge level (up to 40 pC), while the PRPD pattern marked as PD source B shows comparatively a higher rate of pulses with less amount of apparent charge (up to 2 pC) compared to PD source A.

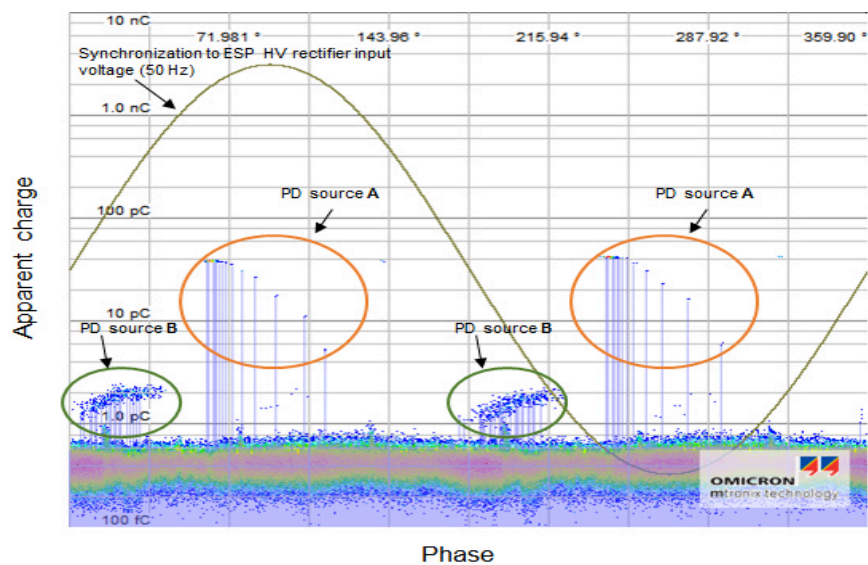


FIGURE 5.14: QPRPD pattern of the ESP unit with a tar polluted HV insulator surface measured at 5 kV DC (PD level of 38.9 pC).

Figures 5.15 and 5.16 show the PRPD pertaining discharge pattern of the surface heated condition of the tar polluted ceramic HV insulator. After surface heating,

the operating voltage is increased from - 5 kV to - 15 kV after 4 hrs. of heating and increased up to - 20 kV after 6 hrs. of heating (refer Figure 5.5 (a)). At the same time, the rate of pulses and the apparent charge level of the PD source A and source B are also increased since the PD activity rises with increasing field strength. It can be found from Figure 5.15 that a 3rd discharge pattern occurs, marked as PD source C, when the applied voltage has reached a magnitude of close to - 15 kV DC. Furthermore, it appears from Figure 5.14 and Figure 5.15 that the discharge pattern show a phase shift of around 50° to lower phase angle. It is assumed that the phase shift of Figure 5.14 is caused by a shift of the synchronization voltage. This seems reasonable since this shift is absent in Figure 5.16. The PD source A is identified as corona activity with a very less activity at - 5 kV DC (refer to Figure 5.14) which shows a stronger occurrence with rising operating voltage manifesting an apparent charge level of around 100 pC in its center at - 20 kV DC (refer to Figure 5.16). In addition to this, PD source B which shows a higher rate of pulses at lower applied voltage is assumed as discharges on the surface of the polluted insulator. This seems reasonable since the number of pulses show a less increase with the rise of the operating voltage magnitude in consequence of the applied surface heating that dried the deposition layer on the insulator surface.

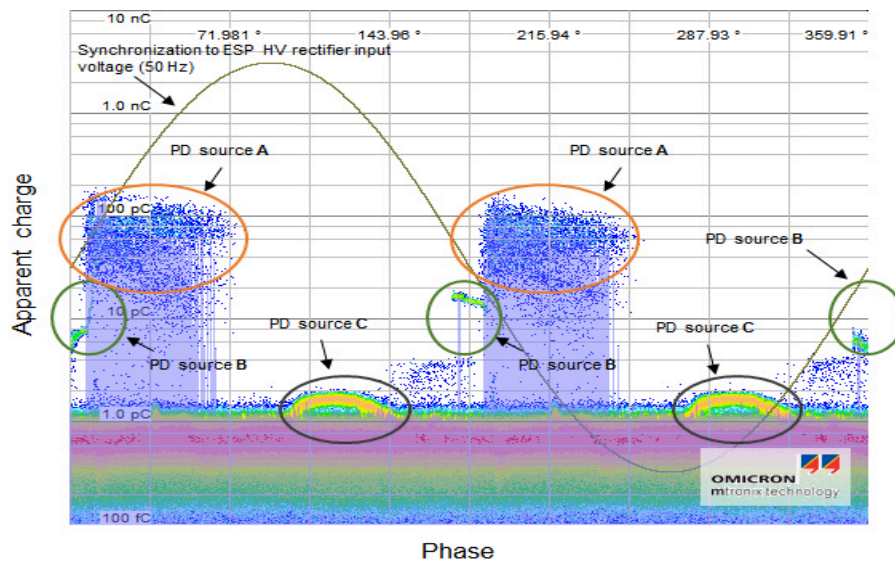


FIGURE 5.15: QPRPD pattern of the ESP unit after 4 hrs of insulator surface heating measured at 15 kV DC (PD level of 60.5 pC).

In addition to this, the PD source C which is visible at higher applied voltage of around - 15 kV DC (refer to Figure 5.15) and is masked by the background noise level with further rise of the applied DC voltage (refer to Figure 5.16) could be a different type of surface discharge due to the fact that the insulator is a feed-through type enabling the possibility of surface discharges between the internal surface and the HV terminal (refer to Appendix B).

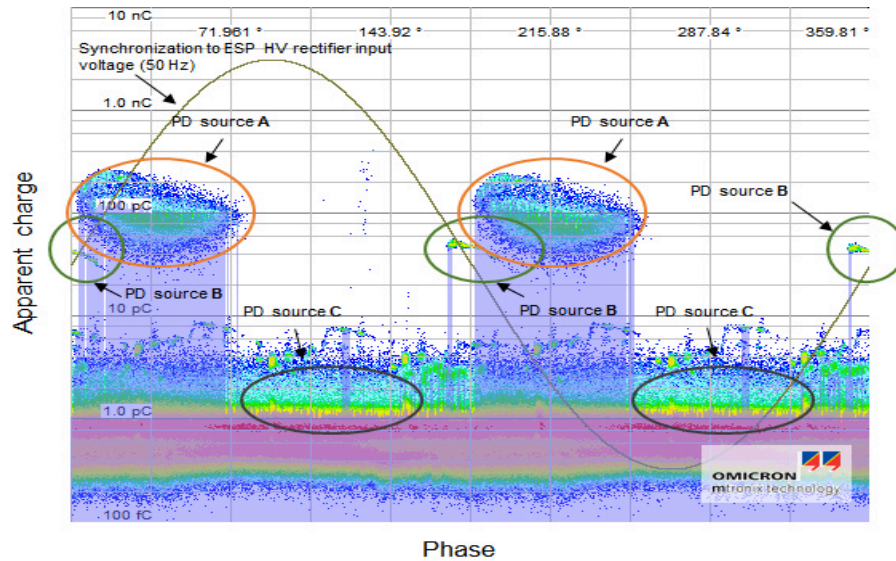


FIGURE 5.16: QPRPD pattern of the ESP unit after 6 hrs of insulator surface heating measured at 20 kV DC (PD level of 129.1 pC).

5.4.2.2 PD Information in Frequency Domain

Figure 5.17 shows the frequency domain representation of the PD signals measured from the ESP unit under different HV insulator surface conditions. Figure 5.17 (a) shows the frequency domain content of the PD signal measured from the tar polluted ESP HV insulator under wet condition, while Figure 5.17 (b) and Figure 5.17 (c) show the respective frequency domain information of the same insulator heated for 4 hrs and 6 hrs, respectively. It can be observed from Figure 5.17 (a) that there are two small peaks in the frequency domain representation at around 1 MHz and 2.5 MHz. However, the peak existing at around 2 MHz is slightly stronger. Its magnitude seems to decrease with an increase of the operating voltage (refer to Figure 5.17 (b)), which further becomes dominant once the voltage reaches around 20 kV (refer to Figure 5.17 (c)). The peak at 2.5 MHz can be assumed as PD activity due to corona, while the peak that arises at close to 1 MHz can be assumed as PD activity in consequence of the presence of surface discharges. These findings are consistent with the results reported in [127]. Furthermore, it can be found from the Figures 5.17 (b) and 5.17 (c) that the increase of the ESP operating voltage in consequence of the applied surface heating procedure provokes more electrical discharges inside the ESP unit.

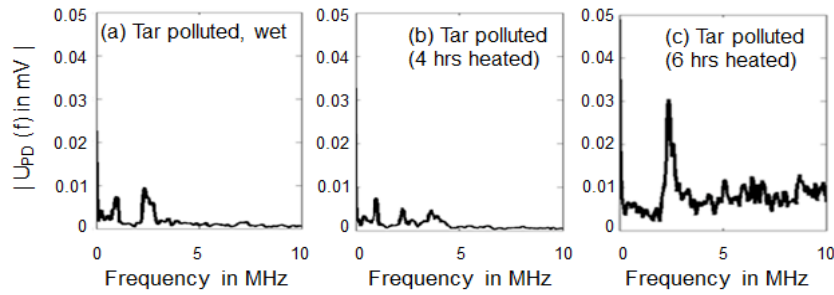


FIGURE 5.17: Frequency domain information of QPRPD signals. (a): Tar polluted HV insulator surface measured at 5 kV DC. (b): HV insulator heated for 4 hrs measured at 15 kV DC. (c): HV insulator heated for 6 hrs measured at 20 kV DC.

5.5 Non-conventional PD Analysis in UHF Range

As an added measure, UHF based PD measurements that record and analyze the electromagnetic signals radiated from the corona discharge of the ESP unit are initiated. Since it is not possible to reproduce the same condition on the HV insulator surface, viz. thickness and composition of the tar contamination layer that are investigated in section 5.4, the UHF based PD analysis of the ESP unit is limited to a clean HV insulator. The UHF method is a state-of-the-art approach for measuring partial discharge activity [128]. Special UHF sensors for partial discharge detection typically work in the frequency range between 300 MHz and 3 GHz [129]. This frequency range has the advantage that a suppression of external noise can be easily achieved. There is, however, no direct link between the conventional measurement according to IEC 60270 and the UHF method existing at the moment. The electromagnetic signals radiated from the PD source are detected using a broadband inductive line end sensor. These signals are amplified by the UHF amplifier (25 dB gain) or attenuated as necessary. The envelope peak of the detected UHF signal is extracted and represented as a phase-resolved event using a PDM system. Sequential cycles of phase-resolved data are displayed as phase-resolved patterns. The photo and the schematic of the complete setup are shown in Figure 5.18 and Figure 5.19 respectively. The attachment of the UHF-PD-coupler to the grounded vessel of the ESP insulator chamber is shown in Figure 5.18.

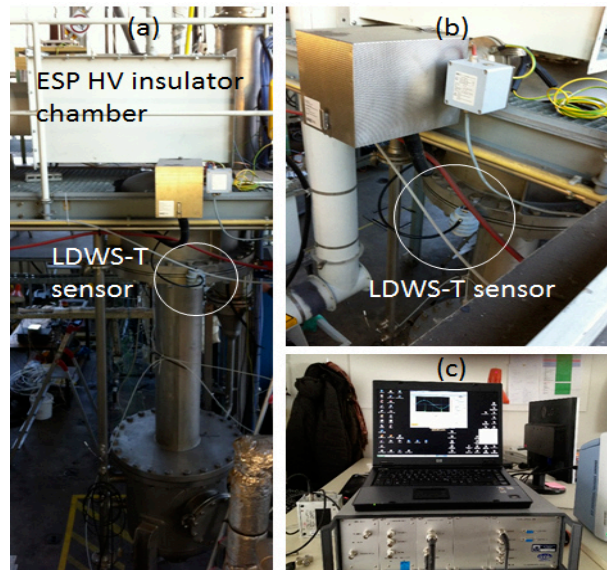


FIGURE 5.18: Photo of the test setup used for measuring the UHF based PD signals from an ESP unit. (a): ESP unit. (b): UHF PD Sensor location at the ESP vessel. (c): LDS-6-UHF PD detector unit.

The fast electromagnetic transients of PD events are captured from the grounded tank of the cleaning chamber and are bridged by a measuring loop which is attached to the UHF-PD-coupler. Therefore, PD defects close to the PD decoupling loop may be well detected, whereas noises and PD events far from the decoupling point are strongly attenuated, which ensures an excellent signal-to-noise ratio.

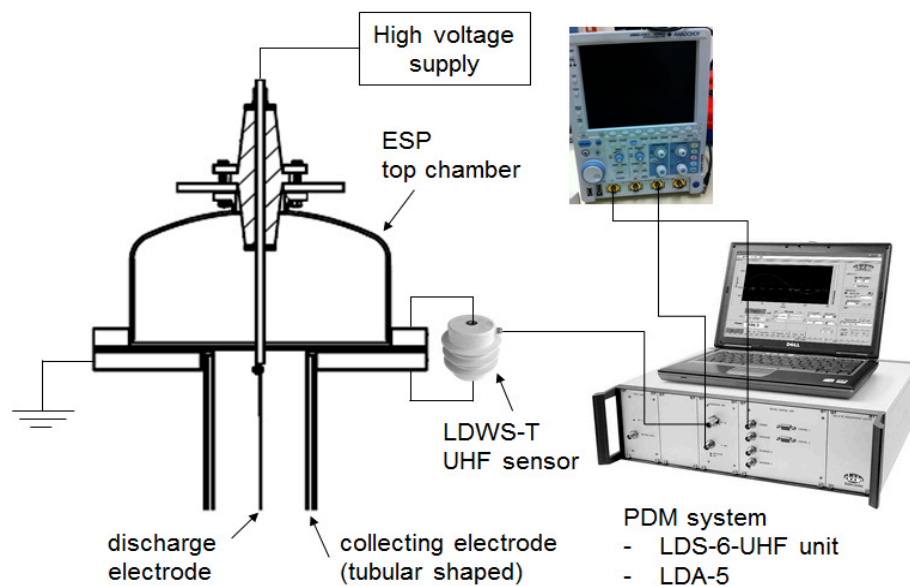


FIGURE 5.19: Schematic of test setup (shown in Figure 5.18) used for online measurements of UHF based PD activity on the surface of an actual ceramic insulator installed in a wet ESP unit.

The output of the UHF-PD-coupler is connected through a co-axial measuring cable (RG-213) to a high-pass filter, which limits the measuring frequency range with a lower limit of approximately 300 MHz. A pre-amplifier installed at the UHF sensor is increasing the signal-to-noise ratio. For PD pulse processing an UHF processing unit with a functionality similar to a spectrum analyzer is plugged in the PDM instrument LDS-6-UHF. The measuring frequency in the zero span mode of the UHF processing unit is adjustable with a frequency bandwidth of 8 MHz in the frequency range of 110 MHz to 1700 MHz. The decoupling of the PD signals from the PD coupler is performed with an external triggering, while the acquisition as well as the storage and the visualization of the PD data are performed by means of a computer-based PD measuring system.

5.5.1 Performance Check

The conventional methods of calibration and apparent charge calculation are not suitable for a UHF based PD measurement procedure. A standardized sensitivity check procedure for UHF sensors installed in a power apparatus is currently not available. However, the same is available (Cigre recommendation TF 15/33.03.05) for Gas Insulated Switchgear (GIS). The Cigre recommendation on PD UHF measurements on GIS recommends the following procedure. The PD signals are decoupled by a UHF sensor and measured through a UHF measuring device or a spectrum analyzer with a low noise amplifier. Later, in the absence of HV, an artificial pulse with known amplitude and of very fast rise time (say in ns) is applied to a UHF sensor which has to be as close as possible to the position in the GIS layout, where the defect was installed. The amplitude of the injected pulse is then raised until a similar spectrum will be measured at the applied sensor like in the previous test, where the HV was turned on. The amplitude of the pulse is noted. Nevertheless, such a procedure recommended for a GIS system cannot be directly extended to the present approach. The geometry, sensor positioning and other relevant factors directly influence the impedance and measuring impedance. Hence, the procedure recommended in the Cigre is slightly modified.

The PD events radiate the electromagnetic signals that propagate and get reflected inside the ESP chamber. So, it is expected these signals could be decoupled through a inductive based UHF sensor connected to the ground strip of the ESP tank. In this regard, it is important to identify the optimum detector frequency, where a sufficient signal-to-noise ratio is achievable. Henceforth, a performance check is initiated by injecting UHF pulse into the HV electrode. Following this, the UHF PD detector is adjusted to an optimum frequency at which better signal noise ratio is achieved. Figure 5.20 shows the injected UHF pulse of 5.0 V, while

Figure 5.21 shows the measured UHF PD pulse plot pattern and Figure 5.22 show the corresponding UHF PD pattern.

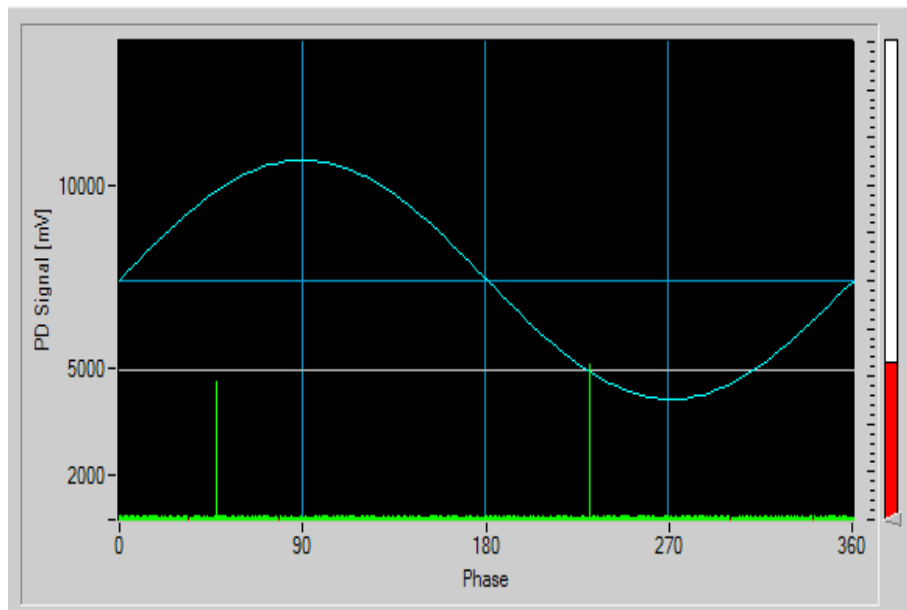


FIGURE 5.20: UHF pulse of 5 V used for the performance check of PD measuring circuit.

It can be observed from the Figures 5.21 and 5.22 that the measured PD pulses that are generated by the UHF calibration unit are close to 5 V. At the same time, it appears from Figure 5.22 that the PD detection sensitivity of the applied setup exhibits a small ripple versus the phase-correlation.

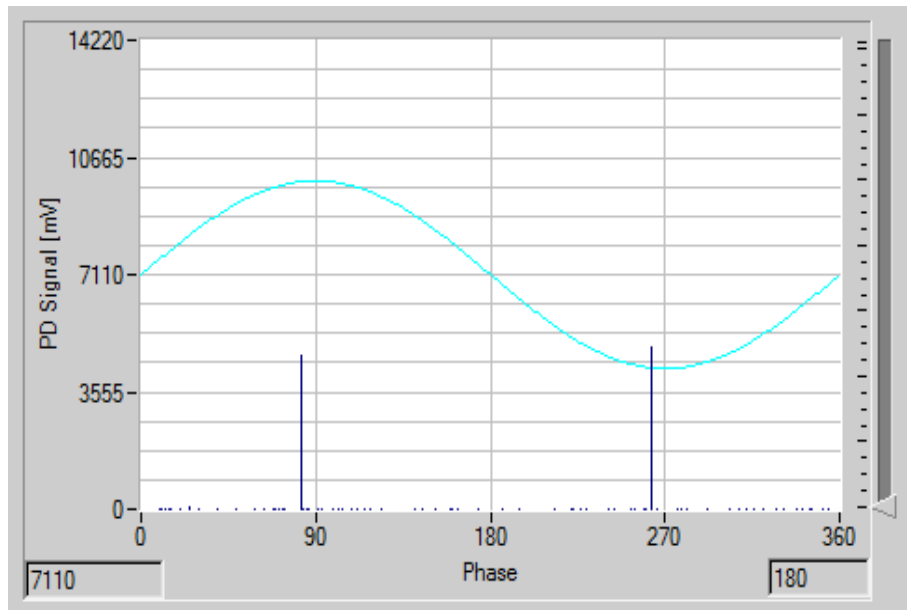


FIGURE 5.21: UHF pulse plot recorded during performance check of PD measuring circuit.

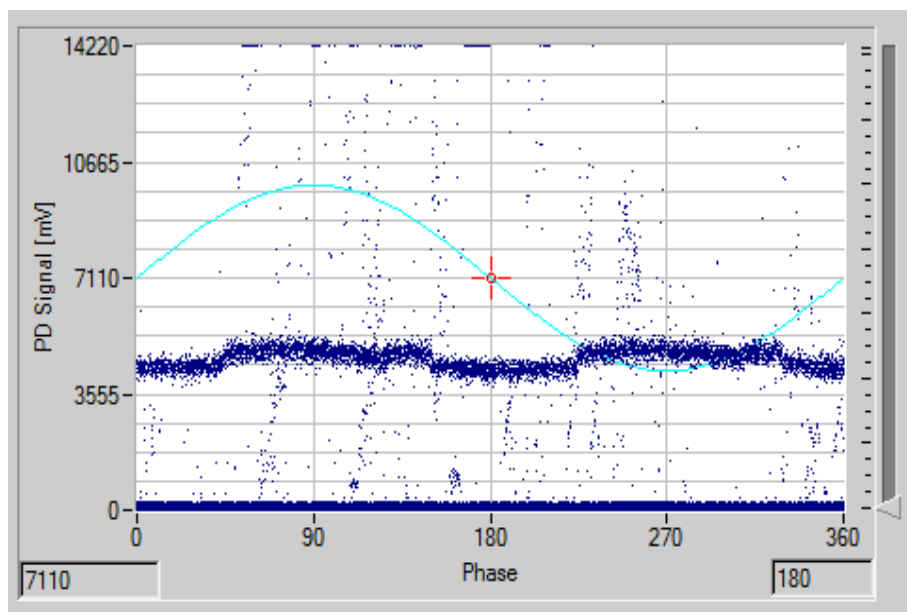


FIGURE 5.22: UHF pattern (related to Figure 5.21) manifested by the UHF pulse during the performance check of PD measuring circuit.

5.5.2 UHF PD Signal Analysis

5.5.2.1 ESP U-I-curve during UHF PD Measurements

The operation condition (applied voltage and secondary current versus time) of the ESP unit during the performed UHF PD measurements is shown in the Figures 5.23 and 5.24 respectively. Figure 5.23 shows the ESP performance during the gasification plant and the ESP unit are flushed with gaseous nitrogen. The ESP performance, that is shown in Figure 5.24, is recorded during operation of the gasification plant and cleaning of producer gas by the applied ESP unit.

The time period from 0 min. to 18 min. and from 25 min. to close to 59 min. of Figure 5.23 corresponds to ESP operation performance during nitrogen flushing. It can be observed from this Figure that the under both condition the applied voltage is close to 33 kV and the secondary current is close to 8 mA respectively. In addition to this, the ESP performance is stable versus time and exhibits around 53 min. a strong increase of the secondary current (close to 13 mA), while at the same time the drop of the applied voltage is of minor degree.

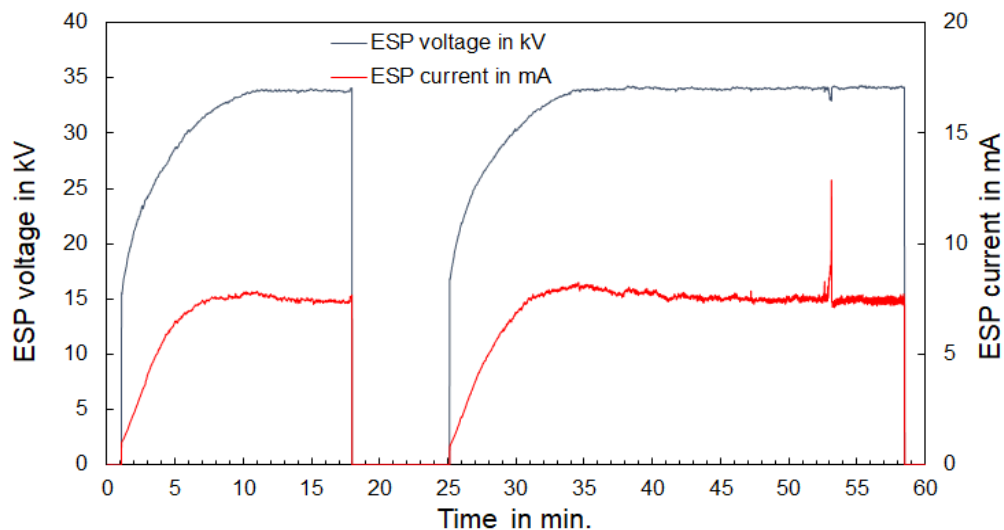


FIGURE 5.23: ESP U-I-curve during N_2 flushing.

Figure 5.24 shows the U-I-curve of the ESP unit during producer gas cleaning. After the gasification plant is flushed with nitrogen and prepared for start-up the ESP unit is switched on (2 min.). The biomass is fed into the fluidized-bed gasifier after 10 min., while the gasifier has reached a steady state after around 30 min. of operation (constant temperature profile of the gasifier unit and a stable composition of permanent gases) and is taken out of operation after 100 min. It can be observed from Figure 5.24 that the secondary current is reduced (about 3 mA)

compared to the operation with nitrogen since during time-consuming preparation of the gasifier operation of around 12 hrs. a certain amount of moisture together with light hydrocarbon compounds condensed on the insulator surface. Furthermore, the secondary current exhibits a slight increase versus time of operation. At the same time, the applied voltage slightly decreases. This can be addressed to the increasing amount of aerosols entering into the electrostatic field of the ESP unit.

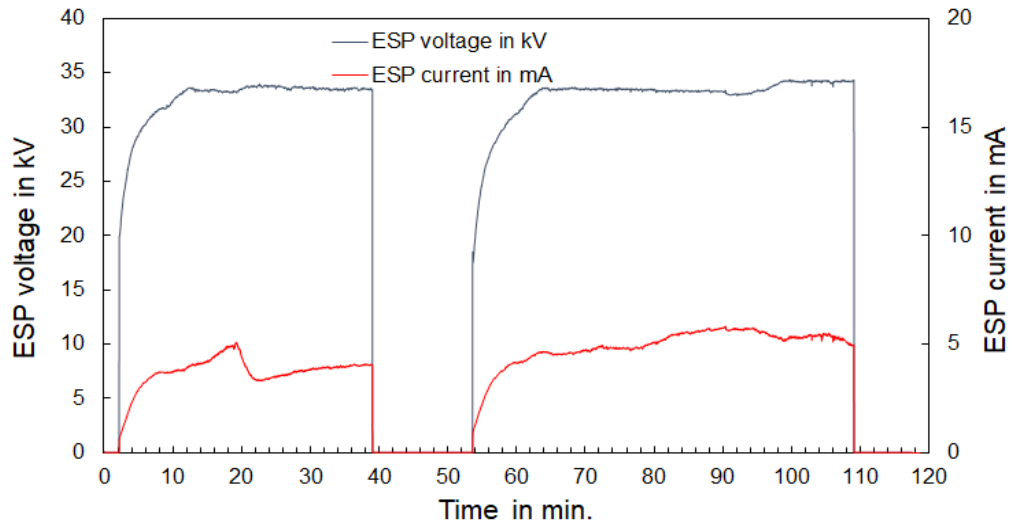


FIGURE 5.24: ESP U-I-curve during producer gas cleaning.

5.5.2.2 UHF PD Pattern Analysis

5.5.2.2.1 Open-Circuit Operation (during N_2 Flushing)

Initially, the baseline data (Figure 5.25 and Figure 5.26) is measured. Such an approach is necessary since due to the high PD detection sensitivity of the PD detector (about 2 mV) PD signals of the test object under investigation are captured along with ambient noises and electromagnetic interference. The recorded UHF PD signals are successfully identified using the PD pattern replay mode feature in the computer-based PD measuring system. This feature can be compared with the replay feature in video-film technology and is capable of visualizing the captured PD pulses phase-by-phase. Thereby, it is possible to distinguish between stochastically occurring noise pulses and periodically occurring "quasi" phase-correlated noise pulses, discharges on the surface of the HV insulator and corona discharges as well as sparks that occur between collecting electrode and discharge electrode.

In order to determine the amount of PD events that occurs in the present test environment (ambient noises and electromagnetic interference due to rotating machines, transformers and so on) the UHF PD baseline data are measured, while the gasification plant and the ESP unit are in open-circuit operation. Figure 5.25 shows the UHF pulse plot line pattern recorded from the ESP unit in open-circuit operation at - 35 kV, while Figure 5.26 shows the corresponding UHF PD pattern, respectively. It can be observed from the Figures 5.25 and 5.26 that there are signal interference due to the operation of the HV rectifier of the ESP unit, the power supply to the electrical consumers of the gasification plant other external sources. Furthermore, the open-circuit operation of the equipment manifests pulse plot lines that seem to emerge stable and phase-correlated close to 90° and 270° (refer to Figure 5.25), while the UHF PD pattern shows a not phase-correlated PD signal interference with a baseline noise level that is close to 600 mV (refer to Figure 5.26).

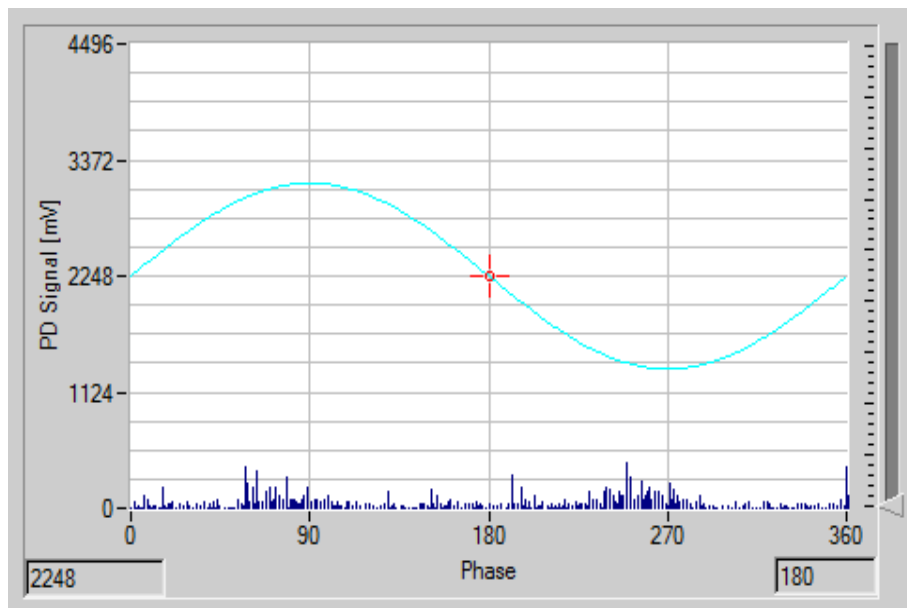


FIGURE 5.25: UHF PD pulse plot line pattern of the ESP unit during open-circuit operation at - 35 kV.

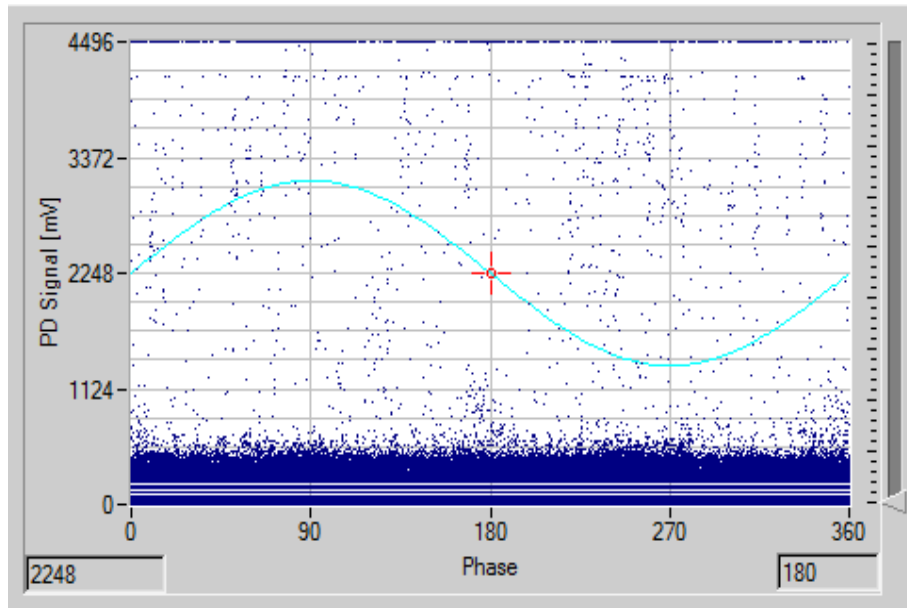


FIGURE 5.26: UHF PD pattern of the ESP unit during open-circuit operation at - 35 kV.

5.5.2.2.2 UHF PD during Nitrogen Flushing and Producer Gas Cleaning

Figure 5.27 and Figure 5.28 show the PRPD pattern that are recorded from the actual ESP unit during N_2 flushing and during producer gas cleaning, respectively. Three observations are possible from these Figures. First, it can be observed from Figure 5.27 and 5.28 that baseline noise level during the operation of the ESP unit is close to 3 times higher compared to open-circuit operation (refer to Figure 5.26). In addition to this, the corona PD pattern (Figure 5.27) recorded from the electrical discharges that occur during N_2 flushing and ESP operation (Figure 5.28) are more or less similar. The main difference are the intensity and the phase correlation of the PD events. The UHF PD signals that are recorded during producer gas cleaning exhibits a higher PD magnitude (around 25 %) compared to the operation in nitrogen. This is reasonable since the presence of aerosols in the producer gas increases the corona activity. The reason for the phase correlation shift of the corona pattern might be due to the fact that the recorded UHF data are mathematically phase-resolved and not synchronized (refer to section 5.4).

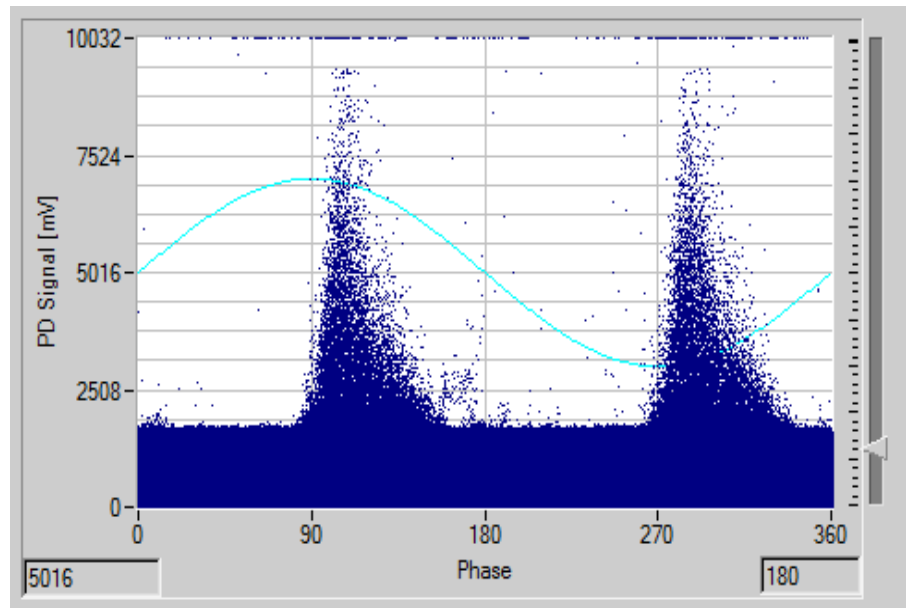


FIGURE 5.27: UHF PD pattern measured from the ESP unit in operation (33 kV and 8 mA) during N_2 flushing.

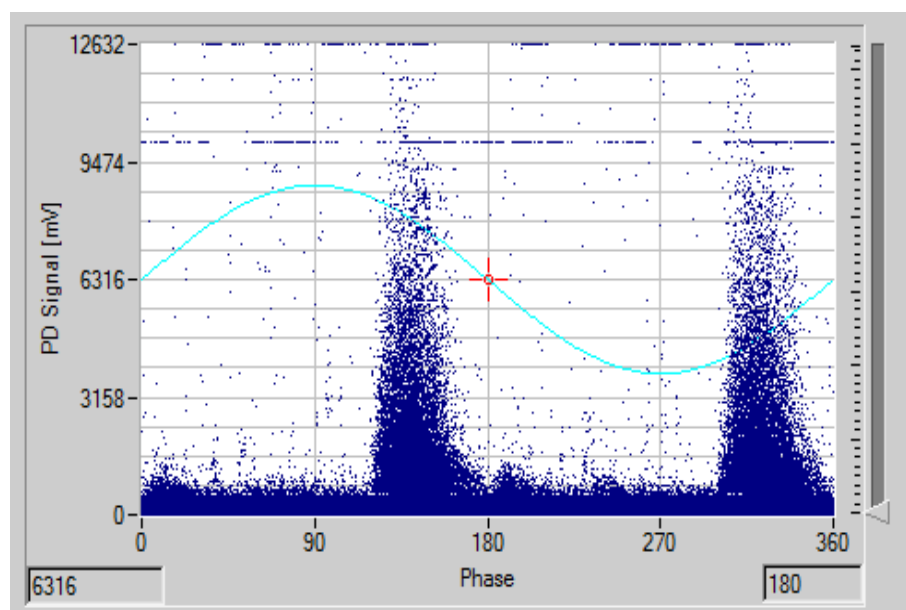


FIGURE 5.28: UHF PD pattern measured from the ESP unit in operation (32 kV, 6 mA) during producer gas cleaning.

Since the UHF PD pattern provides a summation of phase-correlated PD pulses that are recorded over the measuring period it appears that short single PD pulses can not be clearly identified. Therefore, the recorded UHF PD data are analyzed as PD pulse plot line pattern which provides a snapshot of a single measurement that are shown in the following Figures 5.29, 5.30, 5.31 and 5.32, respectively. Figure 5.29 and Figure 5.30 show the PD pulse plot line pattern recorded from

the ESP unit during its operation with nitrogen, while the Figures 5.31 and 5.32 corresponds to the operation of the ESP unit during producer gas cleaning. It can be observed from Figure 5.29 that the pulse plot lines of this pattern arising phase-resolved in the 2nd and 4th quarter are due to the activity of the ESP corona. Contrary, the presence of discharges on the surface of the HV insulator arise in the 1st and 3rd quarter, respectively.

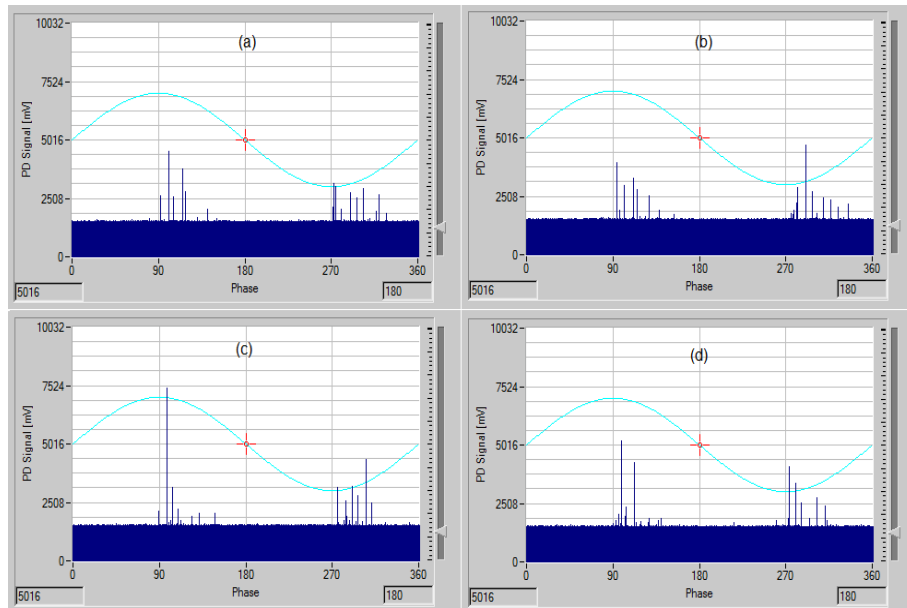


FIGURE 5.29: UHF PD pulse plot line pattern measured from the ESP unit in operation (33 kV and 8 mA) during N_2 flushing.

Furthermore, it can be observed from Figure 5.30 (b) and Figure 5.32 (d) that a strong discharge (arc) between discharge and collecting electrode compromises the activity of the corona. Thereby, the pulse plot lines of the corona pattern are more or less absent. In addition to this, the occurrence of discharges on the surface of the HV insulator (refer to Figure 5.30 (a), (c), (d) and Figure 5.32 (a), (b), (c)) show strong pulse plot lines in the recorded UHF pattern that appear separated in its phase-correlation, while at the same time the activity of the corona pattern is clearly visible. Therefore, the strong increase of the secondary current (refer to Figure 5.23) is identified as a strong discharge of short-period on the surface of the HV insulator (refer to Figure 5.30 (c) and (d)). In addition to this, the surface discharges are of less intensity during producer gas cleaning (refer to Figure 5.24 and Figure 5.32 (c) and (d)).

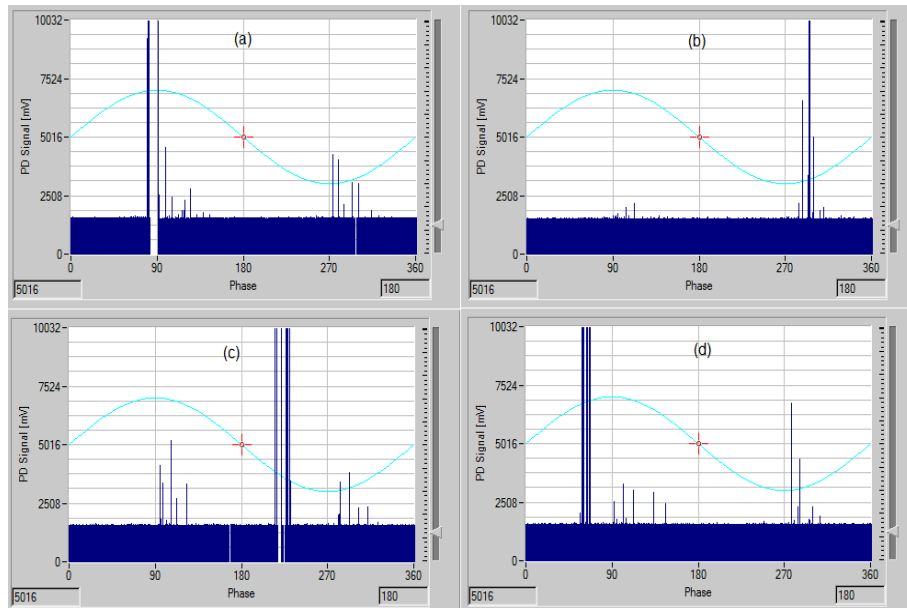


FIGURE 5.30: UHF PD pulse plot line pattern measured from the ESP unit in operation (33 kV and 8 mA) during N_2 flushing.

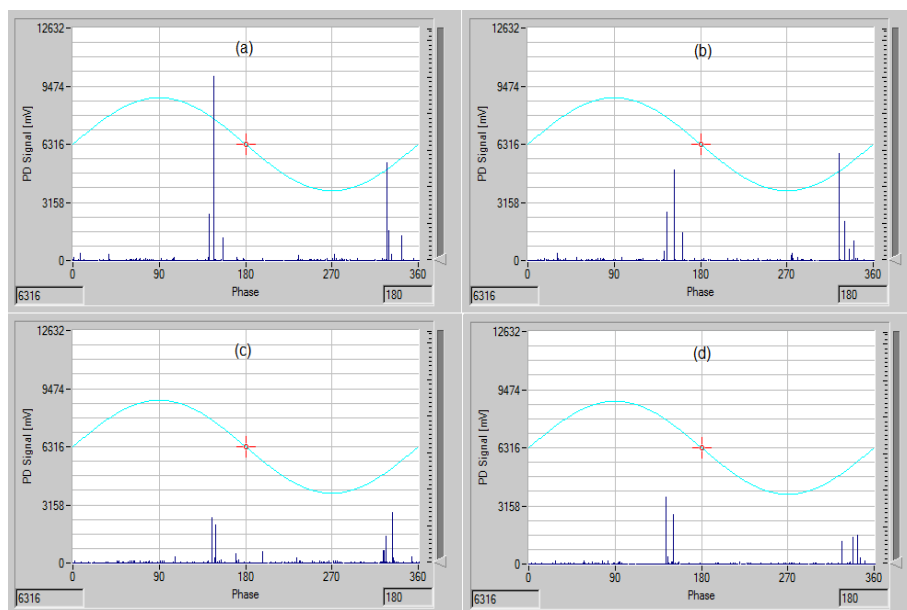


FIGURE 5.31: UHF pulse plot line pattern of ESP corona measured during producer gas cleaning.

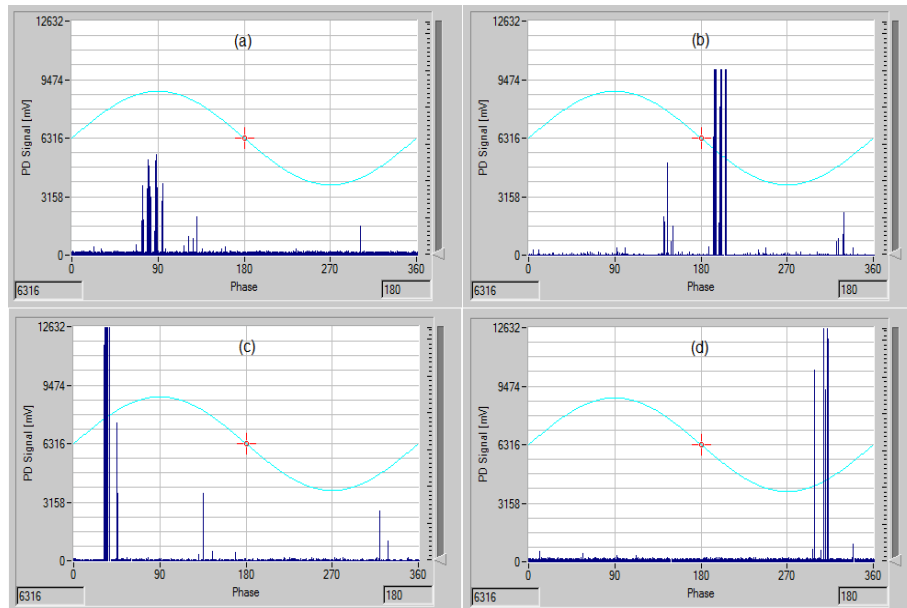


FIGURE 5.32: UHF pulse plot line pattern of surface discharges and sparks measured during producer gas cleaning.

5.6 Inferences

The following inferences are made from the present experimental study:

- The dielectric integrity of a ceramic insulators contaminated with tar on its surface can be resolved through modern diagnostic test procedures. Furthermore, the electrical discharges that arise on the surface of the contaminated ceramic insulator can also be quantified through conventional PD measurements. The intensity of electrical discharges can be correlated to the level of surface contamination.
- The dielectric behavior of condensable hydrocarbons over wide span of time and frequency depends not only in its composition but also on its condition (say dry or wet). It has been experimentally identified that condensable hydrocarbons in dry state improved the dielectric quality of the ceramic insulator. The DC resistance of an insulator with dry condensable hydrocarbons on its surface emerged to be better than that of the clean insulator. Similar observations are made from dielectric response measurements over a wide range of frequency, provided the condensable hydrocarbons are in a dry state. This conforms the fact that certain species of condensable hydrocarbons such as phenol, toluene etc. exhibit dielectric properties. Nevertheless, the same in presence of water behaves different and the dielectric quality

of the ceramic insulator is compromised. Severe contamination might render highly conductive and eventually reduce the operating voltage, thereby hindering the performance and the cleaning efficiency of the ESP unit.

- The surface heating improves the dielectric quality of the insulator to some extent. The reason for such an improvement is attributed to the decrease of water content in the pollution layer of tar. However, electrical discharges inevitably arise on the tar polluted insulator surface. The only possibility to completely regain the dielectric strength of the ceramic insulator is a complete cleaning of the surface which involves manual intervention.

In all, it appears possible to identify the presence of condensable hydrocarbon and hetero-cyclic compounds deposited on the surface of the ceramic insulator through modern dielectric and diagnostic test methods. Consequently, early detection of such surface pollution enables to prevent a premature failure of the HV insulator and the ESP unit. As an alternative measure, the surface of the ceramic insulator can be heated to remove the water content from the polluted insulator surface. Since the dry contamination manifest better properties, surface heating might help in improving the operation condition of the ESP unit. Nevertheless, such an approach can not be considered as an optimal solution since surface heating might cause further damage to the insulator.

Conclusion

6.1 Summary

This thesis reports about the influence of tar on the dielectric integrity of the ceramic support insulator and its pertinent impact on the operating condition and performance of an ESP unit. The objectives of this thesis have been systematically investigated on a test sample that was taken from a tar contaminated broken ceramic insulator. Actual test insulators, installed in a test rig that closely emulates the actual condition in an ESP unit, and an actual wet ESP unit are investigated for validation purpose. The conclusions drawn from this thesis might primarily help in understanding the collective behavior of the multiple species of hydrocarbons under dry and wet conditions. Such knowledge is quite significant, while improving the maintenance procedures of an ESP unit and also in achieving clean energy. Additionally, the pertinent waste disposal procedures could be made much safer for human handling and the environment.

The information gathered in chapter 1 and 2 indicate that there is an increasing interest in understanding the characteristics of condensable aromatic hydrocarbon and hetero-cyclic compounds as well as their derivatives. It is found that few individual aromatic hydrocarbons in their pure form are di-polar in nature. These compounds such as toluene, phenol etc. manifest dipole moments ranging from 0.13 D to 1.396 D. At the same time, certain species like benzene, naphthalene, 1-methylnaphthalene etc. are individually uni-polar and non-conductive. It is proven that aromatic hydrocarbon compounds have to be considered as non-conductive in their pure form and that the presence of any impurity leads into an increase of their conductivity in consequence of the raising amount of free charge

carriers like electrons and/or ions. This indicates that multiple compounds together manifest an entirely different behavior due to dissociation and molecular reaction like radical reaction and polymerization. The present maintenance strategies exercised on electrostatic tar precipitator units and relevant approaches are inadequate in revealing the progress of HV insulator surface deposition and also don't provide an opportunity in understanding the degradation mechanism of dielectric condition of HV insulator under the influence of tar. This situation points out an immediate requirement of research that not only helps in understanding the collective behavior of several compounds of tar but also provides a method to ensure the operating performance of the ESP unit and cleanliness of the producer gas.

The conclusions drawn from this thesis can be broadly categorized into two categories, viz. one that focuses on diagnostic condition assessment of the tar contaminated ceramic insulator, while the other one attempts to understand the relevant mechanism. In a broader sense, the experiments on the test samples (chapter 4), on the HV test insulators installed in a test rig (chapter 4) and on the HV test insulator under operating condition in an ESP unit (chapter 5) altogether validate the possibilities of ascertaining the dielectric integrity of the HV ceramic insulator installed in an ESP unit. The diagnostic experiments on the test samples and on an actual insulator reported in chapter 4 and chapter 5 proved that it is possible to detect surface deposition on an actual insulator at an early stage. The lack of prior attention to the HV insulator resulted in severe deposition of multiple species of tar constituents on its surface causing severe surface discharges and subsequent thermal and electrical stress. Furthermore, the presence of water induced wet condition which further aggravated the scenario, thereby compromising the operating condition and removal efficiency of the ESP unit. Further depositions on the surface of the insulator eventually reduced the operating voltage, thereby aggravating the situation. The subsequent drying up process of the contamination deposited on the surface of the ceramic insulator improved the condition to a certain extent. On the other hand, the applied thermal heat made the surface deposited material glazed, hard and scratch-proof, while its electric response showed a clear increase of the DC resistance compared to its wet condition. Furthermore, localized spots exhibiting high conductivity indicated that the tar compounds deposited on the insulator surface have changed their molecular structure into carbon black similar deposition due to the energy of electrical surface discharges. The second perspective that can be gained from this thesis is related to the apparent surface characteristics of tar contaminated ceramic insulators. Normally, the surface of a ceramic insulator is glazed to achieve a minimal conductivity to warm up and to dry the polluted insulator surface. This implies that a small amount of leakage current on the glazed surface can be tolerated. Nevertheless, the apparent surface

resistance under a clean glazed surface is around $25 \text{ G}\Omega$ and the corresponding loss factor is around 0.1 p.u. at 10 mHz, which is reasonably high. At the same time, the deposition of hydrocarbons under wet condition eventually reduced the surface resistance and increased the dielectric loss factor to a much higher value. The surface resistance dropped from $\text{G}\Omega$ to close to $2 \text{ M}\Omega$, while the loss factor increased (at 10 mHz) to a value of close to 23 p.u. At the same time, drying up the surface of the polluted ceramic insulator seems to improve the apparent characteristics. The surface resistance increased from $2 \text{ M}\Omega$ to $5 \text{ M}\Omega$, while the loss factor decreased from 23 p.u. (under wet condition) to 5.0 p.u. (under dry conditions) at a test frequency value of 10 mHz.

The loss factor values gained from the clean and dry insulator, either installed in a test rig or installed in the ESP unit, match in their shape and values, while their slope values show a small variation (refer section 4.3.2.2 and section 5.3.2). Since the slope values of the loss factor exhibit a behavior that is indirectly proportional to the test frequency in case of DC conductivity, it can be concluded that the slight increase of the loss factor values is a result of the self-capacitance of the insulator that becomes dominant with decreasing frequency values. This slight exponential increase of the loss factor is commonly known characteristic response of homogeneous ceramic insulating materials. Furthermore, the shape of the complex relative permittivity of the clean and dry test insulator surface matches to the literature and its frequency response can be exemplified by an equivalent *RC parallel circuit* with a leaky capacitor. A clear distinction of the insulator surface condition is possible by applying the frequency domain analysis. It has been found that the depositions of tar exhibit a clearly different behavior below 1 Hz, while the same in the presence of water droplets is possible at frequencies below 100 Hz, respectively. The impact of a wet layer of tar on the insulator surface shows in frequency domain analysis an analogy with the LFD response caused by increasing humidity, while the response of water droplets on the insulator surface shows an analogy with a uniform distributed *RC network*. On the one hand, the shape of the loss factor values under compromised surface condition indicates a dominant conductive behavior due to the presence of slowly moving charge carriers. It has been found that the slope of the loss factor under a compromised surface condition of the insulator exhibits comparatively small values close to zero at low test frequency values. This indicates that the increase of the loss factor with decreasing frequency values is a result of the presence of free charges inside and/or in between the surface deposition layer, while their mobility at low frequencies is regionally limited, causing interfacial polarization mechanisms with high time-constant values and orientation polarization in consequence of the polar compounds like phenol, toluene and water. The reason for the presence of the interfacial polarization under polluted surface conditions might be due to the fact

that the pollution layer exhibits an inhomogeneous structure, consisting of different layers that are exhibiting non-uniform dielectric properties in consequence of discontinuous pollution layer buildup due to the operation of the ESP unit and in consequence of the distribution of the individual compounds of tar inside these layers. It becomes clear that the macroscopically uniform pollution layer has to be assumed in microscopic scale as a series- and parallel connection of a resistor and a leaky capacitor, causing the apparent DC resistance, which exhibits constant values over the measured time, while the same of the clean insulator surface shows a slight increase with respect to time. The amount of energy released into the surface deposition layer is comparatively lower under dry condition, while the released energy under wet condition is dominated by water (moisture) which has a stronger dipole moment. These findings are in macroscopic scale and a clearer picture would naturally emerge after adequate verification of pertinent phenomena and a deduced mechanism at molecular level.

In real time, the tar polluted surface of the ceramic insulator suffers severe electrical discharges. In most cases, these discharges are localized on the polluted insulator surface. Hence, exercising a simple conventional and/or non-conventional PD detection method would suffice in assessing the dielectric condition of the ceramic insulator along with the activity of the corona. It is shown that the possible PD sources inside an ESP unit are clearly distinguishable by applying QPRPD analysis (refer to 5.4.2.1). Thus, PD analysis is capable to detect a change of the dielectric insulator surface condition at an early stage. However, the mechanisms corresponding to initial electrical discharges can be explained using a low-temperature plasma approach. During normal operation, certain levels of localized dry patches appear on the contaminated surface due to natural evaporation. Sometimes, the dry patches are formed due to subsequent electrical discharge activity during which the energy of the electrons causes thermal stress, thereby aiding the drying process. Eventually, the carbonization at the localized spot occurs after or in line with the tracking phenomena, causing several conducting regions which eventually bridge into one single path. Such a situation would eventually result in a localized short circuit between carbonized patches, thereby rendering the ceramic insulator completely unusable. In addition to this, it has been found that the strong surface discharges on the polluted insulator surface exhibit dominant peaks in a frequency range below 5 MHz that clearly cover the frequency spectrum of the ESP DC corona discharge. Nevertheless, since the data preparation of the PD signals for frequency domain analysis is a quite time-consuming task, it arises that the overall surface condition of the HV insulator can be directly accessed by the use of QPRPD analysis, which forms the major concern for on-site diagnosis. Furthermore, the online PD analysis method provides advantages in contrast to the applied offline methods. The ESP unit remains in operation, while the PD signals

are measured. In addition to this, it is possible to access the PD signals radiated from the ESP unit by connecting the sensor to a ground strip of the ESP tank ensuring that the measuring devices are not in direct contact with the hazardous compounds of tar.

The applied diagnostic test methods provide altogether the possibility for an early detection of the degradation of the dielectric condition of the insulators induced by surface deposition. It has been found that a clear distinction between wet and dry surface deposition is possible. The time domain analysis provides in short time a view inside the condition of the test object to evaluate its actual quality related to the DC insulation resistance baseline value gained from the respective insulator with clean and dry condition. Furthermore, the possible presence of polar species provoking an increase of the absorption current can be derived from the time dependent trend. More information about the polarization mechanism can be gained by applying frequency domain analysis. The time demand of this diagnostic offline method is comparable high and the further information gained doesn't provide a higher accuracy for the evaluation of the insulation quality. Both, conventional PD and PD in UHF range, provide the advantage of a continuous monitoring of the insulator surface condition. It is demonstrated that the several possible PD sources in an ESP unit can be clearly distinguished, enabling the determination of possible discharges on the insulator surface at an early stage.

In all, the results show that the applied methodology is capable to resolve the dielectric condition of the ceramic insulator. However, the results from the insulator installed in the ESP unit prove that it is possible to evaluate the dielectric condition of the HV insulator regardless the deposition of tar on the internals. Hence, a preparative plant cleaning before a field measurement is not necessary. Nevertheless, it is quite difficult in resolving the composition of the pollution layer and furthermore the individual impact of polar compounds that altogether contributes to the LFD phenomena.

6.2 Limitations and Future Scope

The results and inferences drawn from this thesis are based on a macroscopical investigation. Such an approach is sufficient for gaining a broader insight into the collective behavior of multiple species of condensable hydrocarbons. Also, a betterment of the present maintenance procedures can be achieved through employing offline and online diagnostic monitoring methods. A clearer picture about the actual phenomena would evolve only after fundamental investigations on tar compounds and their properties. This implies studying the influence of individual

aromatic hydrocarbon compounds and their influence under several factors such as humidity, impurity, mixtures of them etc. which form the future scope in this field of research. Further measurements and analysis on test samples with tar contamination would give a deeper understanding in the physics of the aging phenomena using diagnostic testing and monitoring tools. It should be mentioned that utmost care and attention are necessary while handling such test samples.

Reference

- [1] M. Kaltschmitt. Biomass for Energy in Germany Status, Perspectives and Lessons Learned. *Journal of Sustainable Energy and Environmental, Special Issue*, pages 1–10, 2011. URL http://www.jseejournal.com/JSEE_Special_Issue.html.
- [2] M. Kaltschmitt, H. Hartmann, and H. Hofbauer. *Energie aus Biomasse*. Springer-Verlag Berlin Heidelberg, 2016. doi: 10.1007/978-3-662-47438-9.
- [3] S. Arumugam, P. Schröder, Y. Neubauer, and T. Schoenemann. Dielectric and Partial Discharge Investigations on Ceramic Insulator Contaminated with Condensable Hydrocarbons. *IEEE Transactions on Dielectrics and Electrical Insulation Special Issue*, 21(6):2512–2524, December 2014. doi: 10.1109/TDEI.2014.004553.
- [4] P. Schröder, S. Arumugam, Y. Neubauer, and T. Schoenemann. Performance Characteristics and Dielectric Condition of a Wet Electrostatic Precipitator Application for Tar Removal. In *21th EU Biomass Conference and Exhibition, 3-6 June 2013, Copenhagen, Denmark*, pages 789–794, 2013. doi: 10.5071/21stEUBCE2013-2CV.3.14. ISBN: 978-88-89407-53-0.
- [5] L. P. L. M. Rabou, R. W. R. Zwart, B. J. Vreugdenhil, and L. Bos. Tar in Biomass Producer Gas, the Energy research Centre of The Netherlands (ECN) Experience: An Enduring Challenge. *Energy Fuels*, 23:61896198, 2009. doi: 10.1021/ef9007032.
- [6] R. W. R. Zwart, A. Van der Drift, A. Bos, H.J.M. Visser, M.K. Cieplik, and H.W.J. Könemann. Oil-Based Gas Washing - Flexible Tar Removal for High-Efficient Production of Clean Heat and Power as Well as Sustainable Fuels and Chemicals. *Environmental Progress & Sustainable Energy*, 28(3):324–335, October 2009. doi: 10.1002/ep.10383.
- [7] J. H. A. Kiel, S. V. B. van Paasen, J. P. A. Neeft, L. Devi, K. J. Ptasinski, F. J. J. G. Janssen, R. Meijer (KEMA), R. H. Berends, H. M. G. Temmink, G. Brem, N. Padban, and E. A. Bramer. Primary measures to reduce tar formation in fluidized bed biomass gasifier. Technical report, ECN Biomass, Energy research Centre of the Netherlands (ECN), 2004.

- [8] W. Zhang, H. Liu, I. Ul Hai, Y. Neubauer, P. Schröder, H. Oldenburg, A. Seilkopf, and A. Kölling. Gas cleaning strategies for biomass gasification product gas. *International Journal of Low-Carbon Technologies*, February 2012. doi: 10.1093/ijlct/ctr046.
- [9] R. W. R. Zwart. Gas cleaning downstream biomass gasification. Technical report, ECN Biomass, Energy research Centre of the Netherlands (ECN), 2009.
- [10] F. Seidenschnur and E. Groh. Untersuchungen über mechanische und elektrische Teerabscheidung. *Brennstoff-Chemie*, 11(9):188–193, 1928.
- [11] F. Wehrmann, T. Payer, W. Baum, H. Brückner, and F. Schuster. *Handbuch der Gasindustrie. Band 3: Gasreinigung und Nebenproduktgewinnung*. Dr.-Ing. Horst Brückner, 1939.
- [12] R. Schulz. Probleme bei der Filtration unter extremen Gas- und Staubbedingungen. *Chem.-Ing.-Tech.*, 55(11):846–850, 1983. doi: 10.1002/cite.330551106.
- [13] K. R. Parker. *Electrostatic Precipitation. Published in Green Chemistry and Chemical Engineering Series. Particle Technology and Applications*. Taylor & Francis Group, 2012. International Standard Book Number-13: 978-1-4398-8168-2 (eBook - PDF).
- [14] A. Mizuno. Electrostatic precipitation. *IEEE Transaction on Dielectrics and Electrical Insulation*, 7(5):615–624, October 2000. doi: 10.1109/94.879357.
- [15] Y. Neubauer, P. Schröder, I. Litvinov, A. Kölling, W. Zhang H. Liu, N. Sachno, U. Hellwig, H. Oldenburg, and A. Seilkopf. Gas treatment of fuel gases from biomass gasification with structured tube gas cooling, quench, electrostatic precipitator and mop fan filter - experimental results of an era-net bioenergy project. In *19th European Biomass Conference and Exhibition, Berlin, Germany*, pages 1420–1425, 2011. doi: 10.5071/19thEUBCE-VP2.3.18.
- [16] Y. Neubauer, A. Kölling, P. Schröder, F. Behrendt, U. Hellwig, N. Sachno, H. Liu, W. Zhang, I. Ul Hai, S. B. Riffat, and H. Oldenburg. Gas treatment of fuel gases from biomass gasification with structured tube gas cooling, quench, electrostatic precipitator and mop fan filter (emf) - effectiveness and viability of components developed in era-net bioenergy project. In *20th European Biomass Conference*

- and Exhibition, 18-22 June 2012, Milan, Italy, pages 844–849, 2012. doi: 0.5071/20thEUBCE2012-2CO.4.5.
- [17] Y. Neubauer. Strategies for tar reduction in biofuels and synthesis-gases from biomass gasification. *Journal of Sustainable Energy and Environment, Special Issue*, pages 67–71, 2011. URL http://www.jseejournal.com/JSEE_Special_Issue.html.
- [18] H. R. Trenkler. *Die Gaserzeuger. Handbuch der Gaserei mit und ohne Nebenproduktgewinnung*. Julius Springer, 1923. ISBN 978-3-642-90478-3.
- [19] T. A. Milne, R. J. Evans, and N. Abatzoglou. *Biomass Gasifier "Tars": Their Nature, Formation, and Conversion*. National Renewable Energy Laboratories (NREL) Golden, Co., NREL/TP-570-25357, 1998.
- [20] H.-G. Franck and G. Collin. *Steinkohleteer*. Springer-Verlag Berlin Heidelberg New York, 1968. doi: 10.1007/978-3-642-88258-6.
- [21] DIN EN 14639. Crude tar and crude benzole - Characteristics and test methods. European Committee for Standardization (CEN), Brussel, Belgium, November 2005.
- [22] CEN/TS 15439. Biomass Gasifications Tar and Particles in Product Gases Sampling and Analysis. European Committee for Standardization (CEN): Brussels, Belgium, August 2006.
- [23] C. Li and K. Suzuki. Tar property, analysis, reforming mechanism and model for biomass gasification - An overview. *Renewable and Sustainable Energy Reviews*, 13:594–604, 2009. doi: 10.1016/j.rser.2008.01.009.
- [24] E. G. Baker, M. D. Brown, D. C. Elliott, and L. K. Mudge, editors. *Characterization and Treatment of Tars from Biomass Gasifiers*, August 1988. AIChE Summer National Meeting.
- [25] S. V. B. van Paasen and J. H. A. Kiel. Tar formation in a fluidized-bed gasifier. Technical report, ECN, March 2004. ECN-C-04-013.
- [26] H. W. J. Könemann and S. V. B. van Paasen. Olga Tar Removal Technology; 4 MW Commercial Demonstration. In *15th European Biomass Conference & Exhibition, 7-11 May 2007, Berlin, Germany*, pages 873–878, 2007. ISBN 3-936338-21-3.

- [27] L. C. R. de Sousa. *Gasification of Wood, Urban Wastewood (Altholz) and other Wastes in a Fluidised Bed Reactor*. PhD thesis, Swiss Federal Institute of Technology Zürich, 2001. Diss. ETH Nr. 14207.
- [28] H.-G. Franck. The Challenge in Coal Tar Chemicals. *Industrial and Engineering Chemistry*, 55(5):38–44, May 1963. doi: 10.1021/ie50641a006.
- [29] A. N. Lin and K. Moses. Tar Revisited. *International Journal of Dermatology*, 24(4):216–218, May 1985. doi: 10.1111/j.1365-4362.1985.tb05762.x.
- [30] Gruhl. Über elektrische Gasreinigung. *Angewandte Chemie*, 38(26):565–568, Juni 1925. doi: 10.1002/ange.19250382602.
- [31] O. Schärer. Über technische Staubabscheidung und ihre physikalischen Grundlagen. *Schweizer Bauzeitung*, 123/124(5):53–59, Juli 1944. doi: 10.5169/seals-53987.
- [32] J. H. Turner, P. A. Lawless, T. Yamamoto, D. W. Coy, G. P. Greiner, J. D. McKenna, and W. M. Vatauvuk. Sizing and Costing of Electrostatic Precipitators Part I. Sizing Considerations. *JAPCA*, 38(4):458–471, 1988. doi: 10.1080/08940630.1988.10466396.
- [33] Lurgi Gesellschaften. *Lurgi Handbuch*. Lurgi Gesellschaften - Frankfurt am Main, 1960.
- [34] K. Schmidt. *Die Gaserzeuger. Zweite, neubearbeitete und erweiterte Auflage*. Springer-Verlag Wien, 1959. ISBN 978-3-211-80529-9.
- [35] G. W. Penny. A new electrostatic precipitator. *AIEE Transactions on Electrical Engineering*, pages 159–163, 1937. doi: 10.1109/EE.1937.6540096.
- [36] G. W. Penny. Electrostatic precipitation of high resistivity dust. *AIEE Transaction*, 70:1192–1196, 1951. doi: 10.1109/T-AIEE.1951.5060546.
- [37] G. W. Penny. Electrostatic precipitators. *IEE Review, IEE Proceedings*, 135(6):347–361, July 1988. doi: 10.1049/ip-a-1.1988.0056.
- [38] J. Karl. *Dezentrale Energiesysteme. Neue Technologien im liberalisierten Energiemarkt*. De Gruyter Oldenburg, 2004. ISBN 3-486-27505-4.

- [39] P. Hasler and T. Nussbaumer. Gas cleaning for IC engine applications from fixed bed biomass gasification. *Biomass and Bioenergy*, 16:385–395, 1999. doi: 10.1016/S0961-9534(99)00018-5.
- [40] S. Anis and Z. A. Zainal. Tar reduction in biomass producer gas via mechanical, catalytic and thermal methods: A review. *Renewable and Sustainable Energy Reviews*, 15:2355–2377, 2011. doi: 10.1016/j.rser.2011.02.018.
- [41] L. Devi, K. J. Ptasiński, and F. J.J.G. Janssen. A review of the primary measures for tar elimination in biomass gasification processes. *Biomass and Bioenergy*, 24:125140, 2003. doi: 10.1016/S0961-9534(02)00102-2.
- [42] K. Göransson, U. Söderlind, J. He, and W. Zhang. Review of syngas production via biomass DFBGs. *Renewable and Sustainable Energy Reviews*, 15:482492, 2011. doi: 10.1016/j.rser.2010.09.032.
- [43] A. Villot, Y. Gonthier, E. Gonze, A. Bernis, S. Ravel, M. Gâteau, and J. Guillaudeau. Separation of particles from syngas at high-temperatures with an electrostatic precipitator. *Separation and Purification Technology*, 92:181–190, 2012. doi: 10.1016/j.seppur.2011.04.028.
- [44] A. Küchler. *Hochspannungstechnik*. Springer-Verlag Berlin Heidelberg, 2009. doi: 10.1007/978-3-540-78413-5.
- [45] H. Bässler. Über die Gleichstromleitfähigkeit flüssiger Kohlenwasserstoffe. *Phys. kondens. Materie* 2, pages 187–203, 1964. doi: 10.1007/BF02422844.
- [46] E. O. Forster. Electric Conductance in Liquid Hydrocarbons. II. MethylSubstituted Benzenes. *Journal of Chemical Physics*, 40(1):86–90, January 1964. doi: 10.1063/1.1724900.
- [47] A. L. Horvath. Electrical Conductivities of Pure Organic Liquids. *Chem. Eng. Technol.*, 16:238–242, 1993. doi: 10.1002/ceat.270160405.
- [48] I. M. Smallwood. *Handbook of organic solvent properties*. First published in Great Britain 1996 by Arnold, a member of the Hodder Headline Group. Copublished in the Americas by Halsted Press an imprint of John Wiley & Sons Inc., 1996. ISBN 0-340-64578-4.

- [49] J. A. Dean, editor. *Langes Handbook of Chemistry*. McGRAW-HILL, INC., 1999. ISBN 0-07-016384-7.
- [50] Z. Rappoport, editor. *The chemistry of phenols Part 1*. John Wiley & Sons Ltd, The Atrium, Southern Gate, Chichester, West Sussex PO19 8SQ, England, 2003. ISBN 0-471-49737-1.
- [51] E. O. Forster. Electric Conduction in Liquid Hydrocarbons. I. Benzene. *Journal of Chemical Physics*, 37(5):1021–1028, September 1962. doi: 10.1063/1.1733206.
- [52] W. B. Green. Conduction and Breakdown in Hexane. *Journal of Applied Physics*, 26(10):1257–1264, October 1955. doi: 10.1063/1.1721886.
- [53] D. C. Northrop and O. Simpson. Electronic properties of aromatic hydrocarbons I. Electrical conductivity. *Proceedings of the Royal Society of London*, pages 124–135, 1956. doi: 10.1098/rspa.1956.0020.
- [54] A. I. Belousov, I. V. Rozhkov, and E. M. Bushueva. Measurement of bulk electrical conductivity of hydrocarbon liquids. *Plenum Publishing Corporation*, pages 474–476, 1983. doi: 10.1007/BF00725997.
- [55] E. A. Nartey. Oil/ Paper Insulation for HVDC: Conductivity of Oil. Master’s thesis, Norwegian University of Science and Technology, 2011.
- [56] F. Schober, A. Küchler, and C. Krause. Oil conductivity - An Important Quantity for the Design and the Condition Assessment of HVDC Insulation Systems. *FHWS Sciene Journal*, 1(2):59–78, 2013.
- [57] S.O. Morgan and W. A. Yager. Dielectric Properties of Organic Components Relation to Chemical Composition and Physical Structure. *Industrial and Engineering Chemistry*, 32(11):1519–1528, November 1940. doi: 10.1021/ie50371a024.
- [58] United States Environmental Protection Agency. Locating and estimating air emissions from sources of polycyclic organic matter. Technical report, United States Environmental Protection Agency, 1998. URL <https://www3.epa.gov/ttnchie1/le/pompta.pdf>.
- [59] United States Environmental Protection Agency. A resource for mgp site characterization and remediation: Expedited site characterization and source remediation at

- former manufactured gas plant sites. Technical report, United States Environmental Protection Agency, 1999. URL https://www.epa.gov/sites/production/files/2015-08/documents/mgp_chap1-4a.pdf.
- [60] The World Bank Group in collaboration with the United Nations Environment Programme and the United Nations Industrial Development Organization. Pollution prevention and abatement handbook. Technical report, The International Bank for Reconstruction and Development/The World Bank Group, 1998. URL http://www.ifc.org/wps/wcm/connect/9ecab70048855c048ab4da6a6515bb18/coke_PPAH.pdf?MOD=AJPERES. ISBN 0-8213-3638-X.
- [61] M.-H. Cho, T.-Y. Mun, and J.-S. Kim. Production of low-tar producer gas from air gasification of mixed plastic waste in a two-stage gasifier using olivine combined with activated carbon. *Energy*, 58:688–694, 2013. doi: 10.1016/j.energy.2013.06.021.
- [62] J. Katz. Maintenance program and procedures to optimize electrostatic precipitators. *IEEE Transaction on Industry Applications*, IA-11(6):674–680, 1975. doi: 10.1109/TIA.1975.349354.
- [63] P. Schröder, S. Arumugam, Y. Neubauer, and T. Schoenemann. Diagnosis of operating conditions of high voltage insulators in electrostatic precipitators. In *ETG-Fachbericht 134 - Diagnostik elektrischer Betriebsmittel 2012, 15-16 November 2012, Fulda, Deutschland*, 2012. ISBN 978-3-8007-3465-8.
- [64] H. J. White. *Entstaubung industrieller Gase mit Elektrofiltern*. VEB Deutscher Verlag für Grundstoffindustrie, September 1969. VLN 152-915/72/69.
- [65] L. F. Hawley and H. M. Pier. Application of Electrical Precipitation to the Wood-Distillation Process. *Chemical and Metallurgical Engineering*, 26(22):1031–1033, May 1922.
- [66] P. Schröder, S. Arumugam, Y. Neubauer, M. Schuchardt, F. Behrendt, and T. Schoenemann. Investigations on Ageing Phenomena of a Tar contaminated Porcelain Insulator. In *19th International Conference on Gas Discharge and Their Applications, 2-7 September 2012, Beijing, China*, pages 778–781, 2012. ISSN: 1003-6520.

- [67] C. Brage, Q. Yu, G. Chen, and K. Sjöström. Tar evolution profiles obtained from gasification of biomass and coal. *Biomass and Bioenergy*, 18:87–91, 2000. doi: 10.1016/S0961-9534(99)00069-0.
- [68] M. Israelsson, M. Seemann, and H. Thunman. Assessment of the Solid-Phase Adsorption Method for Sampling Biomass-Derived Tar in Industrial Environments. *Energy and Fuels*, 27:7569–7578, 2013. doi: 10.1021/ef401893j.
- [69] S. A. Nair, K. Yan, A. J. M. Pemen, E. J. M. van Heesch, K. J. Ptasinski, and A. A. H. Drinkenburg. Tar Removal from Biomass Derived Fuel Gas by Pulsed Corona Discharges: Chemical Kinetic Study II. *Ind. Eng. Chem. Res.*, 44:1734–1741, 2005. doi: 10.1021/ie049292t.
- [70] S. A. Nair, K. Yan, A. J. M. Pemen, E. J. M. van Heesch, K. J. Ptasinski, and A. A. H. Drinkenburg. Tar Removal from Biomass-Derived Fuel Gas by Pulsed Corona Discharges. A Chemical Kinetic Study. *Ind. Eng. Chem. Res.*, 43:1649–1658, 2004. doi: 10.1021/ie034066p.
- [71] S.A. Nair, K. Yan, A.J.M. Pemena, G.J.J. Winandsa, F.M. van Gompela, H.E.M. van Leukena, E.J.M. van Heescha, K.J. Ptasinskib, and A.A.H. Drinkenburg. A high-temperature pulsed corona plasma system for fuel gas cleaning. *Journal of Electrostatics*, 61:117–127, February 2004. doi: 10.1016/j.elstat.2004.02.002.
- [72] M. A. Malik and M. Ahmed. Preliminary studies on formation of carbonaceous products by pulsed spark discharges in liquid hydrocarbons. *Journal of Electrostatics*, 66:574577, 2008. doi: 10.1016/j.elstat.2008.06.004.
- [73] van Heesch. Pulsed corona tar cracker. *IEEE Transactions on Plasma Science*, 28:1571–1575, 2000. doi: 10.1109/27.901235.
- [74] L. Yu, X. Li, X. Tu, Y. Wang, S. Lu, and J. Yan. Decomposition of Naphthalene by dc Gliding Arc Gas Discharge. *J. Phys. Chem. A*, 114:360–368, 2010. doi: 10.1021/jp905082s.
- [75] M. Kang, B.J. Kim, S. M. Cho, C.-H. Chung, B.-W. Kim, G. Y. Han, and K. J. Yoon. Decomposition of toluene using an atmospheric pressure plasma/TiO₂ catalytic system. *Journal of Molecular Catalysis A: Chemical*, 180:125–132, 2002. doi: 10.1016/S1381-1169(01)00417-4.

- [76] M. P. Cal and M. Schluep. Destruction of benzene with non-thermal plasma in dielectric barrier discharge reactors. *Environmental Progress*, 20(3):151–156, October 2001. doi: 10.1002/ep.670200310.
- [77] A. Jaworek, M. Jedrusik, A. Swierczok, and M. Lackowski. Biomass Co-firing - New challenge for electrostatic precipitators. *International Journal of Plasma Environmental Science and Technology*, 5(2):161–167, January 2011. URL http://www.iesj.org/html/service/ijpest/vol15_no2_2011/IJPEST_Vol15_No2_11_pp161-167.pdf.
- [78] K. R. Parker, editor. *Applied Electrostatic Precipitation*. Springer Netherlands, 1997. doi: 10.1007/978-94-009-1553-4. Hardcover ISBN: 978-0-7514-0266-7.
- [79] Siemens-Schuckertwerke. Anordnung für Isolatoren elektrische Niederschlagsanlagen. Patentschrift 332 805, 1922.
- [80] Siemens-Schuckertwerke. Vorrichtung zur Verhinderung von Staubablagerungen auf den Isolatoren elektrische Gasreiniger. Patentschrift 505 686, 1930.
- [81] O. Güpner, W. Böbel, and G. Böning. Vorrichtung zur Verhinderung einer zur Verschmutzung führenden Wirbelbildung bei der Belüftung von Isolatoren in elektrischen Gasreinigung- oder Emulsionstrennanlagen. Patentschrift 1 093 447, 1961.
- [82] BETH Maschinenfabrik. *Handbuch Staub*. 1959.
- [83] Electronic German Commission for Electrical, Information Technologies of DIN, and VDE. Ceramic and glass-insulating materials - Part 3: Specifications for individual materials (IEC 60672-3:1997); German version EN 60672-3:1997, 1997.
- [84] D. C. Jolly. Contamination Flashover Theory and Insulator Design. *Journal of The Franklin Institute*, 294(6):483–500, December 1972. doi: 10.1016/0016-0032(72)90099-3.
- [85] IEC 60112:2003+AMD1:2009. Method for the determination of the proof and the comparative tracking indices of solid insulating materials, January 2009. Fourth edition.
- [86] W. Oburger. *Die Isolierstoffe der Elektrotechnik*. Springer-Verlag Wien, 1957. ISBN 978-3-662-24084-7.

- [87] E. Ivers-Tiffée and W. von Münch. *Werkstoffe der Elektrotechnik*. B. G. Teubner Verlag, 2007. ISBN 978-3-8351-0052-7.
- [88] M. Beyer, W. Boeck, K. Möller, and W. Zaengl. *Hochspannungstechnik. Theoretische und praktische Grundlagen für die Anwendung*. Springer-Verlag Berlin Heidelberg New York, 1986.
- [89] B. Pevzner. Transport and Dielectric Properties of Thin Fullerene (C60) Films. Master's thesis, Massachusetts Institute of Technology, December 1995.
- [90] A. K. Jonscher. Review A new understanding of the dielectric relaxation of solids. *Journal of Material Science*, 16:2037–2060, 1981.
- [91] M. Koch and M. Krüger. The negative dissipation factor and the interpretation of the dielectric response of power transformers. In *16th International Symposium on High Voltage Engineering, ISH 2009, 24-28 August 2009, Cape Town, South Africa*, 2009.
- [92] W. S. Zaengl. Dielectric spectroscopy in time and frequency domain for HV power equipment. I. Theoretical considerations. *IEEE Electrical Insulation Magazine*, 19(5):5–19, Sept.-Oct. 2003. doi: 10.1109/MEI.2003.1238713.
- [93] A. K. Jonscher. Dielectric relaxation in solids. *J. Phys. D: Appl. Phys.*, 32:R57R70, 1999. URL <http://iopscience.iop.org/0022-3727/32/14/201>.
- [94] N. Panda. Complex impedance spectroscopy for monitoring frequency response to the electrical properties of polycrystalline materials. *Int. J. of Intelligent Computing and Applied Sciences*, 4, 2016. ISSN 2322-0031.
- [95] F.-C. Chiu. A review on conduction mechanisms in dielectric films. *Hindawi Publishing Corporation*, 2014, 2014. doi: <http://dx.doi.org/10.1155/2014/578168>. Article ID 578168.
- [96] G. W. Bak and A. K. Jonscher. Low-frequency dispersion in hopping electronic systems. *Journal of Materials Science*, 34:5505–5508, 1999.
- [97] A. K. Jonscher. *Dielectric Relaxation in Solids*. Chelsea Dielectrics Press Limited, new corrected impression (1996) edition, 1983. ISBN 0 950871109.

- [98] A. K. Jonscher. *Universal relaxation law*. Chelsea Dielectrics Press Limited, 1996. ISBN 0950871125.
- [99] J. S. Kim, B. C. Choi, H. K. Yang, J. H. Jeong, S. T. Chung, and S-B. Cho. Low-frequency dielectric dispersion and electrical conductivity of pure and la-doped srbi2nb2o9. *Journal of Korean Physical Society*, 52(2):415–420, 2008. doi: 10.3938/jkps.52.415.
- [100] W. D. Kingery, H. K. Bowen, and D.R Uhlmann. *Introduction into Ceramics*. John Wiley & Sons, Inc., second edition edition, 1976. ISBN 0-471-47860-1.
- [101] Y. Feldman, A. Puzenko, and Y. Ryabov. Non-debye dielectric relaxation in complex materials. *Chemical Physics*, pages 139–168, 2002.
- [102] C. P. Smyth. *Dielectric Behavior and Structure*. McGRAW-HILL, INC., 1955.
- [103] A. Cavallini, G. C. Montanari, S. Chandrasekar, and F. Puletti. Inferring ceramic insulator pollution by innovative approach resorting to PD detection. *IEEE Transactions on Dielectrics and Electrical Insulation*, 14(1):23–29, 2007. doi: 10.1109/TDEI.2007.302866.
- [104] A. Cavallini, G. C. Montanari, S. Chandrasekar, and F. Puletti. A Novel Approach for the Inference of Insulator Pollution Severity. In *Conference Record of the 2006 IEEE International Symposium on Electrical Insulation, 11-14 June 2006, Toronto, Ont.*, pages 114–117, 2006. doi: 10.1109/ELINSL.2006.1665270.
- [105] I. Y. Shurrab, A. El-Hag, K. Assaleh, and R. Ghunem. Partial Discharge On-Line Monitoring of Outdoor Insulators. In *IEEE Conference*, pages 391–394, 2012. doi: 10.1109/ELINSL.2012.6251496.
- [106] B. G. Stewart, D. M. Hepburn, I. J. Kemp, A. Nesbitt, and J. Watson. Detection and Characterisation of Partial Discharge Activity on Outdoor High Voltage Insulating Structures by RF Antenna Measurement Techniques. In *High Voltage Engineering, 1999. Eleventh International Symposium on (Conf. Publ. No. 467)*, volume 5, pages 188–191, August 1999. doi: 10.1049/cp:19990917.
- [107] S. Arumugam, P. Schröder, Y. Neubauer, and T. Schoenemann. An experimental study on electrostatic precipitator with tar contaminated HV insulator through

- UHF based PD test methods. In *18th International Symposium on High Voltage Engineering, 25-30 August 2013, Seoul, Korea*, pages 1234–1239, 2013.
- [108] S. Arumugam, P. Schröder, Y. Neubauer, S. Gorchakov, K.-D. Weltmann, and T. Schoenemann. Electrical Discharge on the Condensable Hydrocarbons under the influence of DC Voltage: An Experimental approach. In *20th International Conference on Gas Discharges and their Applications, 6-11 Juli 2014, Orleans, France*, pages 630–633, 2014. URL <http://gd2014.sciencesconf.org/28558>.
- [109] S. Boggs, A. Pathak, and P. Walker. Partial discharge. XXII. High frequency attenuation in shielded solid dielectric power cable and implications thereof for PD location. *IEEE Electrical Insulation Magazine*, 12(1):9–16, Jan.-Feb. 1996. doi: 10.1109/57.484104.
- [110] J. P. Steiner, P. H. Reynolds, and W. L. Weeks. Estimating the location of partial discharges in cables. *IEEE Transactions on Electrical Insulation*, 27(1):44–59, Feb. 1992. doi: 10.1109/14.123440.
- [111] S. Arumugam, S. Gorchakov, and T. Schoenemann. Evaluation of Partial Discharge Failures on HV Apparatus Over a Wide Frequency. In *International Conference on Condition Monitoring and Diagnostics, 21.-25. Sept. 2014 (CMD 2014), Jeju Island, South Korea*, 2014.
- [112] E. Lemke, S. Berlijn, E. Gulski, M. Muhr, E. Pultrum, T. Strehl, W. Hauschild, J. Rickmann, and G. Rizzi. Guide for Partial Discharge Measurement in Compliance to IEC 60270. Technical brochure, CIGRE, December 2008. In behalf of WG D1.33.
- [113] IEC 60270. High-voltage test techniques - Partial discharge measurement, Dezember 2000. Third edition.
- [114] Laborunterlagen Hochspannungstechnik. Technical report, Technische Universität Graz. Institut für Hochspannungstechnik und Systemmanagement, WS2006/2007.
- [115] U. Gafvert, L. Adeen, M. Tapper, and P. Ghasemi. Dielectric spectroscopy in time and frequency domain applied to diagnostics of power transformers. *Proceedings of the 6th International Conference on Properties and Applications of Dielectric Materials, 21-26 June*, 2:825–830, June 2000. doi: 10.1109/ICPADM.2000.876357.

- [116] U. Gafvert. Influence of geometric structure and material properties on dielectric frequency response of composite oil cellulose insulation. *Proceedings of 2005 International Symposium on Electrical Insulating Materials, 5-9 June 2005*, 1:73–76, 2005. doi: 10.1109/ISEIM.2005.193329.
- [117] M. Hassig, R. Braunlich, R. Gysi, and J.-J. Alff. On-site applications of advanced diagnosis methods for quality assessment of insulation of power transformers. *2001 Annual Report Conference on Electrical Insulation and Dielectric Phenomena, 14-17. October 2001*, pages 441–447, October 2001. doi: 10.1109/CEIDP.2001.963577.
- [118] T. K. Saha and P. Purkait. Investigation of an expert system for the condition assessment of transformer insulation based on dielectric response measurements. *IEEE Transactions on Power Delivery*, 19(3):1127–1134, July 2004. doi: 10.1109/TPWRD.2004.829100.
- [119] T. K. Saha. Review of modern diagnostic techniques for assessing insulation condition in aged transformers. *IEEE Transactions on Dielectrics and Electrical Insulation*, 10(5):903–917, October 2003. doi: 10.1109/TDEI.2003.1237337.
- [120] K. Schon. *Hochspannungsmesstechnik. Grundlagen Messgeräte Messverfahren*. Springer Fachmedien Wiesbaden GmbH 2016, 2016. doi: 10.1007/978-3-658-15178-2. ISBN 978-3-658-15178-2 (eBook).
- [121] G. Hoogenraad and J. Beyer. Digital HVDC partial discharge testing. In *Electronic Insulation, 2000. Conference Record of the 2000 IEEE International Symposium on. 5 April 2000.*, 2000. doi: 10.1109/ELINSL.2000.845545.
- [122] E. Lemke, S. Strehl, S. Markalous, and W. Weissenberg. Ultra-wide-band PD Diagnostics of Power Cable Terminations in Service. *IEEE Transaction on Dielectrics and Electrical Insulation*, 15(6):1570–1575, December 2008. doi: 10.1109/TDEI.2008.4712659.
- [123] *User Manual Pulse Generator LDC-7/UHF*. DOBLE LEMKE GmbH. Manual Version: 09.
- [124] D. J. Scheiber. An ultra low frequency bridge for dielectric measurements. *Journal of Research of the National Bureau of Standards - C. Engineering and Instrumentation*, 65C(1):23–42, 1961.

-
- [125] W. Zhou, J. Zuo, and W. Ren. Thermal conductivity and dielectric properties of al/pvdf composites. *Composites: Part A* 43, pages 658–664, 2012. doi: 10.1016/j.compositesa.2011.11.024.
- [126] VDI 3678 Blatt 1. Elektrofilter Prozessgas- und Abgasreinigung, September 1998.
- [127] A. Akbari, H. R. Mirzaei, M. Kharezi, and A. Mazhabjafari. New Informative Features of Partial Discharges and Limitations of Conventional Measuring Devices. *XVth International Symposium on High Voltage Engineering (ISH 2007), Ljubljana, Slovenia, 27-31 August, 2007*.
- [128] A. Müller, M. Beltle, M. Siegel, and S. Tenbohlen. Assesment of UHF PD Monitoring Data by means of Pattern Recognition. In *18th International Symposium on High Voltage Engineering. 25-30 August Seoul, Korea*, pages 1850–1855, 2013.
- [129] F. Alvarez, F. Garnacho, J. Ortego, and M. A. Sanchez-Uran. Application of HFCT and UHF Sensors in On-Line Partial Discharge Measurements for Insulation Diagnosis of High Voltage Equipment. *Sensors*, 15:7360–7387, 2015. doi: 10.3390/s150407360.

Appendix A

Physical and electrical properties of aromatic hydrocarbons that are predominantly present in producer gas.

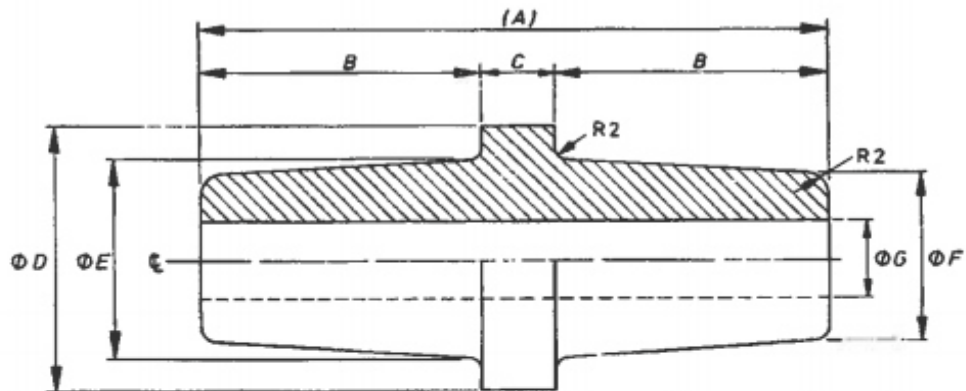
Appendix A: Properties of condensable hydrocarbon species present in producer gas from biomass gasification

IUPAC name	unit	benzene	toluene	styrene	phenol	indene	naphthalene	1-methyl-naphthalene	acenaphthalene	fluorene	anthracene
Empirical formula		C_6H_6	C_7H_8	C_8H_8	C_6H_5OH	C_9H_8	$C_{10}H_8$	$C_{11}H_{10}$	$C_{12}H_8$	$C_{13}H_{10}$	$C_{14}H_{10}$
Chemical structure											
Relative molar mass [g/mol]		78.11 [1]	92.14 [1]	104.15	94.11	116.16	128.17	142.20	154.21	166.22	178.23
Specific density [kg/dm ³]		0.88	0.87	0.91	1.07	0.99	1.14	1.02	1.15	1.20	1.24
Condition of aggregation [2]		20 °C, 1013 hPa	liquid	liquid	solid	liquid	solid	liquid	solid	solid	solid
Vapor pressure [hPa]		100	29.1	7.14	n.a.	1.61	2 (26°C)	n.a.	n.a.	n.a.	n.a.
Melting point [°C]		1013 hPa	5.5	-95	41	-2	80.3	-31	95	113-115	217
Boiling point [°C]		1013 hPa	80	111	182	182	218	245	278	295	340
Flashpoint [°C]			-11	6	32	51	80	94	135	152	121
Polarity		nonpolar [7, 12]	nonpolar	nonpolar	polar	nonpolar	nonpolar	nonpolar	nonpolar	nonpolar	nonpolar
Polarity (water = 100) [10]			11.1	9.9	94.2	n.a.	n.a.	n.a.	n.a.	n.a.	n.a.
Solubility in water [g/dm ³]		20 °C	1.8	0.52	84	insoluble	0.032	0.028 (25 °C)	0.003-0.004 (25 °C)	0.0018	insoluble
Conductivity (specific conductance)			$4.4 \cdot 10^{-14}$ [9]	$8.0 \cdot 10^{-16}$ [9]	$2.7 \cdot 10^{-8}$ [9]	n.a.	n.a.	n.a.	n.a.	n.a.	$1 \cdot 10^{-18}$ [1]
			$1.1 \cdot 10^{-14}$ [20 °C [2]]	$80.0 \cdot 10^{-16}$ [25 °C [2]]	1.73 [4]						$2 \cdot 10^{-2}$ [0 °C [1]]
			$4.4 \cdot 10^{-17}$ [9]		1.45 [8]						0 [1]
					$(1.43) \cdot 10^{-6}$ [50 °C [8]]						
Resistance			n.a.	n.a.	n.a.	n.a.	n.a.	n.a.	n.a.	n.a.	$5 \cdot 10^{14}$ [1]
Dipole moment			0 [20 °C [9]]	0.4 [20 °C [9]]	2.2 [40 °C [9]]	n.a.	0 [10]	(0.85) [8]	n.a.	n.a.	n.a.
			0 [8]	0.36 (8)	1.73 [4]						
			0 [20-30 °C [9]]	1.0 [20-30 °C [9]]	1.45 [8]						
					1.396 [17]						
Static dielectric constant (relative permittivity)			2.28 [20 °C [9]]	2.38 [20 °C [9]]	10.0 [60 °C [9]]	n.a.	2.54 [50 °C [3]]	2.92 [20 °C [17, 18]]	n.a.	n.a.	2.65 [228 °C [9]]
			2.27 [25 °C [9]]	2.38 [25 °C [9]]	10.3 [45 °C (4)]			2.85 [40 °C [19]]			2.64 [223 °C [9]]
			2.284 [20 °C [9]]	2.408 [25 °C [9]]	12.31 [30 °C [9]]			2.79 [50 °C [9]]			2.63 [243 °C [9]]
			2.282 [20 °C [9]]	2.381 [20 °C [9]]	13.4 [20 °C [14]]						

- ¹Perry's chemical engineers handbook, 8th edition, 2008.
- ²Geotis Geklerstoff Datenbank, URL: <http://www.dgvc.de/ita/CeGeklerstoffdatenbankum/GESTIS-Stoffdatenbank/index.jsp> (2011.08.14).
- ³V. G. Bobyl, B. G. Romanets, and V. A. Alysh'ev, *Izvestiya VUZ. Fizika*, No. 6, pp. 46-53, 1965.
- ⁴Morgan, S.O. and Yager, W. A. *Ind. Eng. Chem.*, 37 (11), pp. 1519-1528, 1940.
- ⁵Maryott, Arthur A. and Smith, Edgar B. *United States Department of Commerce. National Bureau of Standards Circular* 514, 1951.
- ⁶John A. Hildick and William B. Bunger, *Techniques of Chemistry Volume II, Organic Synthesis, Physical Properties and Methods of Purification*, John Wiley & Sons, 4. Auflage 1966.
- ⁷Puanganti, Sri R. and Vargas, Francisco M. and Chapman, Walter G. *Ind. Eng. Chem. Res.*, 52, pp. 8069-8070, 2013.
- ⁸Ralph D. Nelson, Jr., David R. Lide, Jr. and Arthur A. Maryott, *United States Department of Commerce. National Standard Reference Data Series - National Bureau of Standards 10, Category 3- Atomic and Molecular Properties*, Sept. 1967.
- ⁹Christian Reichardt and Thomas Welton, *Solvents and Solvent Effects in Organic Chemistry*, Fourth Edition, 2011 WILEY-VCH Verlag GmbH & Co. KGaA, Weinheim.
- ¹⁰Smallwood, Ian M. *Handbook of organic solvent properties*, Copublished in the Americas by Halsted Press an imprint of John Wiley & Sons Inc., 1994.
- ¹¹Wardlaw, D. C. and Simpson, O. *Electronic properties of aromatic hydrocarbons I. Electrical conductivity*, Proceedings of the Royal Society of London, pp. 124-135, 1955.
- ¹²E. O. Förster, *J. Chem. Physik*, vol. 37, No. 5, pp. 1021-1028, 1962.
- ¹³E. O. Förster, *J. Chem. Physik*, vol. 40, No. 1, pp. 85-90, 1964.
- ¹⁴George, J., Sastri, N.V.; *J. Chem. Thermodynamics* 35 (2003), 1037.
- ¹⁵Landolt-Börnstein, *Eigenschaften der Materie in ihren Aggregatzuständen*, Elektrische Eigenschaften, Springer 2008.
- ¹⁶John A. Dean, editor, *Langas Handbook of Chemistry*, MCGRAW-HILL, INC., 1999, ISBN 0-07-016384-7.
- ¹⁷Zvi Rappaport, editor, *The chemistry of phenols Part 1*, John Wiley & Sons Ltd, The Atrium, Southern Gate, Chichester, West Sussex PO19 8SQ, England, 2003, ISBN 0-471-40737-1.

Appendix B

Dimension sheet of the HV test insulator.



porcelain no.	A	B	C	D max.	E max.	F	G min.	H
CB1M	223	102	19	82	57	47	18	61
CB2M	225	102	21	107	80	70	39	86
CB3M	381	178	25	159	114	102	64	121
CB6M	291	135	21	107	80	70	39	86
CB7M	225	102	21	117	89	80	48	95

NOTE 1 The end faces are to be free from glaze and perpendicular to porcelain axis.

NOTE 2 For porcelains CB3M and CB6M the end faces are to be ground perpendicular to porcelain axis.

NOTE 3 The seating flange faces are to be free from glaze and ground perpendicular to porcelain axis outside a diameter of "H".

Material: glazed porcelain

Tests and tolerances to BS 4963 except where otherwise stated

All dimensions are in millimetres.